

Low variability, snowmelt runoff inhibits coupling of climate, tectonics, and topography in the Greater Caucasus

Expanded Methods and Figures

Adam M. Forte¹, Joel S. Leonard², Matthew W. Rossi³, Kelin X. Whipple², Arjun M. Heimsath², Lasha Sukhsvili⁴, Tea Godoladze⁴, and Fakhraddin Kadirov⁵

¹Department of Geology & Geophysics, Louisiana State University, Baton Rouge, LA, USA

²School of Earth and Space Exploration, Arizona State University, Tempe, AZ, USA

³Earth Lab, Cooperative Institute for Research in Environmental Sciences (CIRES), University of Colorado, Boulder, CO, USA

⁴Institute of Earth Sciences and National Seismic Monitoring Center, Ilia State University, Tbilisi, Georgia

⁵Institute of Geology and Geophysics of Azerbaijan National Academy of Sciences, Baku, Azerbaijan

Contents

1 Data Availability	3
2 Expanded Methods	3
2.1 ^{10}Be Sample Site Selection	3
2.2 ^{10}Be Sample Processing	3
2.3 Erosion Rate Calculation	4
2.4 Topographic, Tectonic, and Climatic Analysis	4
2.4.1 Basin Averaged Analyses	4
2.4.2 Convergence and Uplift Along- and Across-Strike	4
2.5 Evaluating Influence of Lithology on Topography, Quartz Sourcing, and Erosion Rates	6
2.6 Potential Divisions within k_{sn} and Erosion Rate Relationship	6
2.7 Fitting a Stream Power Incision Model Based Relationship Between k_{sn} and Erosion Rate	7
2.7.1 Bootstrap Approach	7
2.7.2 Monte-Carlo Approach	7
2.7.3 Performing the Fits	7
2.8 Discharge, Runoff, and Variability in the Caucasus in Gauged Basins	8
2.9 Estimating Hydroclimatic Parameters in Ungauged Basins	8
2.9.1 Estimation of Mean Runoff	8
2.9.2 Estimation of Runoff Variability	9
2.10 Application of the Stochastic Threshold Incision Model	9
2.10.1 Review of Parameters within STIM	9
2.10.2 Parameterization of the STIM Relationship in the Caucasus	11
2.10.3 Comparison of SPIM and STIM Relationships	13
2.10.4 Cluster Analysis of STIM Relationship	13
3 Supplemental Table Captions	13
3.1 Table S1	13
3.2 Table S2	13
3.3 Table S3	13
3.4 Table S4	14

List of Figures

S1	GPS velocities	15
S2	Across strike GPS Swaths	16
S3	χ -Z plots of sampled basins	17
S4	Quartz sourcing and erosion rates	18
S5	GPS velocity and erosion rates	18
S6	Spatial variation in erosion rates	19
S7	Topography and lithology comparisons for all basins	20
S8	Topography correlations	21
S9	Topography, gradient, erosion rate, and concavity	22
S10	Runoff and runoff variability in gauged basins	23
S11	Power law fit of data	24
S12	Measuring channel widths from imagery	25
S13	Channel width data from erosion rate basins	26
S14	Variation of optimized k_e , R and lithology	27
S15	k_{sn} , erosion rate, and optimized k_e and τ_c	27
S16	SPIM and STIM Residuals	28
S17	Cluster number selection	28
S18	Spatial distribution of clusters	29
S19	Clustered k_{sn} -E relationships and STIM relationships	30
S20	Convergence rate and clusters	31
S21	Predicted erosion rates from clustered and population wide STIM relationships	31
S22	Seasonal control on variability	32
S23	Rainfall and Runoff Time Series	33
S24	Lithology distribution for Sample 10115-4	34
S25	Lithology distribution for Sample 10215-2	35
S26	Lithology distribution for Sample 10215-3	36
S27	Lithology distribution for Sample 10215-4	37
S28	Lithology distribution for Sample 10215-5	38
S29	Lithology distribution for Sample 10315-1	39
S30	Lithology distribution for Sample 92215-1	40
S31	Lithology distribution for Sample 92315-1	41
S32	Lithology distribution for Sample 92315-3	42
S33	Lithology distribution for Sample 92415-2	43
S34	Lithology distribution for Sample 92415-3	44
S35	Lithology distribution for Sample 92515-1	45
S36	Lithology distribution for Sample 92515-2	46
S37	Lithology distribution for Sample 92715-4	47
S38	Lithology distribution for Sample 93015-1	48
S39	Lithology distribution for Sample 93015-2	49
S40	Lithology distribution for Sample CT15081	50
S41	Lithology distribution for Sample CT15123	51
S42	Lithology distribution for Sample CT15125	52
S43	Lithology distribution for Sample CT15131	53
S44	Lithology distribution for Sample 82916-1	54
S45	Lithology distribution for Sample 82916-3	55
S46	Lithology distribution for Sample 82916-4	56
S47	Lithology distribution for Sample 83016-2	57
S48	Lithology distribution for Sample 83116-1	58
S49	Lithology distribution for Sample 90216-1	59
S50	Lithology distribution for Sample 90216-2	60
S51	Lithology distribution for Sample 90216-3	61
S52	Lithology distribution for Sample 90416-1	62

S53	Lithology distribution for Sample 90516-1	63
S54	Lithology distribution for Sample 90516-3	64
S55	Lithology distribution for Sample 90616-1	65
S56	Lithology distribution for Sample 91416-1	66
S57	Lithology distribution for Sample 16AF01	67

1 Data Availability

The majority of the relevant data for the sample locations and associated data (e.g. gauged watersheds) are provided as tables at the end of this document. To aid in reproducibility and ease of usage, we also provide these data as text files in a GitHub repository. In this repository we also provide selected analysis scripts (these are highlighted in the supplemental methods document that follows), shapefiles, and rasters necessary to reproduce the analyses we present. A complete list of the contents of the repository can be found in the ReadMe file in the repository.

2 Expanded Methods

2.1 ^{10}Be Sample Site Selection

Sample locations were pre-selected based on several criteria. Specifically, we primarily targeted basins with drainage areas between 5 - 100 km² and that did not include major knickpoints within their profiles or major variations in mean local relief (2500 m window) or normalized channel steepness (k_{sn}). The lower bound on drainage area was to avoid sampling extremely small catchments whose erosion rates can be significantly biased by landsliding events [Yanites et al., 2009, Niemi et al., 2005] and the upper bound was designed to avoid averaging over large spatial areas where erosion rates may vary due to tectonic heterogeneity (e.g. basins spanning across major structures, etc). We additionally avoided sampling catchments which included areas that were currently glaciated or had been glaciated during the last glacial maximum [Gobejishvili et al., 2011]. We attempted to select sample basins with minimal lithologic heterogeneity, but this was not often possible considering the other restrictions along with more practical access restrictions (i.e. we were operating in Azerbaijan and Georgia and as such only were only able to sample from locations within those countries, additionally, Georgia has two Russian occupied territories which are not accessible and restricts the area within the Georgian Greater Caucasus that could be sampled). We also made an effort to sample across a wide range of mean annual precipitation rates and basin mean normalized channel steepness.

In the field, sample sites were evaluated for potential local landslide activity and human modification. Both Georgia and Azerbaijan have a long history of human occupation and many settlements are preferentially built along rivers. When possible, we sampled river sediments upstream of settlements. Additionally, we attempted to sample tributaries at least 500 meters in elevation above their confluences with major trunk streams to avoid sampling reworked sediment that could have been deposited as a result of landslide dams on major streams. Sediment samples were preferentially taken from the active channels or bar deposits without vegetation. In total, we collected 76 samples (Table S2).

2.2 ^{10}Be Sample Processing

Of the 76 total samples, based on their spatial distribution, coverage of parameter space as defined by normalized channel steepness and mean annual precipitation rates, and additional field or topographic observations, we selected 47 samples to process for ^{10}Be . All samples were processed in the Surface Processes WOMBAT Laboratory in the School of Earth and Space Exploration at Arizona State University. Samples were wet sieved to 250-1000 μm and then air dried. All samples were cleaned in a 1:1 solution of HCl and HNO₃ at room temperature for 24 hours. Because of the abundance of quartz rich lithic clasts within the samples, initial attempts at standard HF and HNO₃ leaches to clean and concentrate quartz [e.g. Kohl and Nishizumi, 1992] were unsuccessful, and thus we needed to implement the much more labor and time intensive Hot Phosphoric Acid (HPA) technique [Mifsud et al., 2013]. Through trial and error, we modified the original HPA technique to a three step process where in small (80g) aliquots of the sample were first boiled in a 50% solution of NaOH for 10-20 minutes, allowed to cool, and then washed thoroughly to decant off the fine grained residue. Then the remainder of the sample was slowly heated to 220°C in 80% orthophosphoric acid (H₃PO₄) to form pyrophosphoric acid (H₄P₂O₇) and then leached in this solution for 30-60 minutes. Finally, after cooling, the samples were washed thoroughly and boiled in another 50% solution of NaOH for 15-30 minutes and then, after cooling, washed and dried. The modified HPA technique was successful in removing the majority of feldspars and/or disaggregating lithic components present within the samples.

After the HPA, minerals denser than $2.85 \frac{g}{cm^3}$ were removed via lithium polytungstate (LST) density separation. To purify the remaining quartz, the remaining samples were leached in 1-5% HF and HNO_3 solutions on heated rollers for at least 12 hours. Quartz yields for the majority of samples were very low (<5%), despite large masses (>1500g) of processed sample (Table S2). Of the original 47 samples, only 35 samples had sufficient quartz to proceed. Remaining quartz was spiked with either commercial or a low-background ^{9}Be blank and digestions for purified quartz in HF and HNO_3 lasted for 7-10 days. We removed cations and anions using standard liquid chromatography techniques [Ditchburn and Whitehead, 1994]. Oxidized beryllium was mixed with a niobium matrix and loaded into cathodes for analysis at PRIME Lab, Purdue University. Beryllium isotope ratios for samples and blanks were referenced to isotope ratios defined in the 07KNSTD (Table S3). One sample (92715-2), which had been particularly problematic during the liquid chromatography steps, came back with 0 measured ^{10}Be , but spatially was surrounded by samples with very low erosion rates, thus we do not interpret this as a high erosion rate sample, but rather some sort of chemical processing error, and as such we exclude this from Table S3 and other subsequent results.

2.3 Erosion Rate Calculation

To calculate the catchment averaged erosion rates, we use the approach of Portenga and Bierman [2011], wherein for each basin we identify a single effective elevation, latitude, and longitude to approximate a suitable production rate of ^{10}Be for the entire basin. To accomplish this, we use topography for each basin from the Shuttle Radar Topography Mission (SRTM) 30-m digital elevation model and calculate a scaled ^{10}Be production rate based on the elevation and latitude of each pixel, using the production rate from spallation reactions using the scheme by Stone [2000]. From this, we calculate the mean production rate and then find the elevation and latitude (i.e. the effective latitude and elevation) within the basin that corresponds to this production rate. We use this effective latitude and elevation, along with the longitude of the centroid of the sampled basin and the calculated ^{10}Be concentrations in the online exposure age calculator formerly known as the CRONUS-Earth online exposure age calculator [Balco et al., 2008], v3.0 (accessed August 2019). Parameters used for erosion rate calculations are provided in Table S2. We assume no topographic shielding as this effect is usually small and has generally been shown to be unnecessary in steep landscapes [DiBiase, 2018]. We report erosion rates from all three schemes as reported by the calculator in Table S3, but elsewhere only use the time independent 'St' estimate using the scheme of Stone [2000].

2.4 Topographic, Tectonic, and Climatic Analysis

2.4.1 Basin Averaged Analyses

We use the Shuttle Radar Topography Mission (SRTM) 30 meter digital elevation model and a combination of TopoToolbox [Schwanghart and Scherler, 2014] and the Topographic-Analysis-Kit [TAK; Forte and Whipple, 2019] to calculate basin averaged statistics. For calculation of normalized channel steepness (k_{sn}), we use a reference concavity of 0.50, a smoothing length of 1000 m, the 'ksn_quick' method within TAK and for hillslope gradients we use the 'arcslope' method within the base TopoToolbox gradient8 function. We report a variety of basic topographic statistics and metrics, including elevation, k_{sn} (across a range of concavity values), gradient, and the best fit concavity and χR^2 for each basin (Table S3). The χR^2 statistic describes the extent to which the relationship between χ and elevation is linear. A steady state basin with no knickpoints should have a linear χ and elevation relationship and thus a χR^2 value close to 1. χR^2 values for basins generally are a better indicator of potential disequilibrium than either the standard deviation or standard error of the mean of k_{sn} as these metrics more reflect noise in the underlying DEM. All but two of the reported basins (16AF01 and 90216-1) have χR^2 values > 0.9 , and χR^2 of trunk stream values $>$ than 0.97, indicating the majority of these basins lack major knickpoints (Figure S3). The knickpoints in 16AF01 and 90216-1 are not extreme and neither of these basins represent outliers in k_{sn} or erosion rate space, thus we do not think that their inclusion in the analysis is inappropriate, however we evaluate their exclusion from the dataset in a later section.

2.4.2 Convergence and Uplift Along- and Across-Strike

The presence of an along-strike, eastward increasing gradient in modern convergence velocity has long been noted in the Greater Caucasus, attributed to the counter-clockwise rotation of the Lesser Caucasus block about an Euler pole in the eastern Black Sea [e.g. Reilinger et al., 2006]. Forte et al. [2014] analyzed this convergence gradient by grouping GPS velocities as either south of the Greater Caucasus (i.e. stations within the Lesser Caucasus or southern foreland basins of the Greater Caucasus) or within the Greater Caucasus. As the velocities of stations north of the Greater Caucasus are effectively zero (referenced to stable Eurasia), this implies that the motion of the Lesser Caucasus are a proxy for the total convergence accommodated within the Greater Caucasus. We perform a similar analysis as Forte et al. [2014] to compare the ^{10}Be erosion rates to convergence along the length of the range. We first compiled available GPS data using the original datasets used by Forte et al. [2014], [Reilinger et al., 2006, Kadirov et al., 2012], but also with additional stations and updated observations for previously included stations from Sokhadze et al. [2018]. We then classify stations as either being representative of the movement of regions south of the Greater Caucasus (the black stations in Figure S1, as being within the Greater Caucasus, or outside the domain of interest.

The selection of Lesser Caucasus stations largely corresponds to the Lesser Caucasus block defined by Reilinger et al. [2006], but we include stations further west, extending all the way to the Black Sea coast (i.e. across the East Anatolian fault used as the western boundary of this block in Reilinger et al. [2006]). The selection of stations here is similar to those used in previous publications wishing to approximate the along-strike convergence within the Greater Caucasus [e.g. Avdeev and Niemi, 2011, Forte et al., 2014].

We then use TAK [Forte and Whipple, 2019] to project the locations of these selected stations onto the swath along the crest of the Greater Caucasus so that they have a common reference frame with the erosion rate basins. Because of the bends in the swath profile used throughout this paper (e.g. Figure S1) and the relatively long distances between the swath and some of the stations within the Lesser Caucasus, simply projecting station locations directly onto the swath tends to result in stations 'bunching' at swath bends. To correct for this, we first projected the locations of stations along a swath with the same median location of the main swath, but without bends and oriented at 115° , parallel to the approximate strike of the Greater Caucasus and orthogonal to the plane onto which we resolve velocities. We then projected the locations of stations along this swath onto the swath line with bends. We calculate the velocity and slice through the error ellipse in a $N25^\circ E$ direction for individual stations as this is perpendicular to the average 115° strike of the Greater Caucasus.

The division between which stations are defined as 'Lesser Caucasus' or 'Greater Caucasus' is reasonably straight forward in the eastern Greater Caucasus where there are few intervening stations (e.g. Swaths D-D' and E-E' in Figure S2), but is less clear in the western Greater Caucasus (e.g. Swaths B-B' and C-C' in Figure S2). Also as highlighted especially in Swath B-B', the transition from Lesser to Greater Caucasus stations is represented as a semi-continuous velocity gradient, consistent with locked faults at depth [e.g. Reilinger et al., 2006, Sokhadze et al., 2018]. In these areas, we classified stations clearly in the foreland basins as 'Lesser Caucasus' (e.g. Swath C-C' in Figure S2). The most problematic region was in the area centered around swath B-B' (Figure S2), here we identified a somewhat clear break in velocity (~ 175 km in B-B') and classified stations south of this as 'Lesser Caucasus' and north of this as 'Greater Caucasus'. This is consistent with prior similar groupings, e.g. Reilinger et al. [2006] placed a block boundary in a nearly identical location, Avdeev and Niemi [2011] identified an intermediate group of stations as 'Kura and Rioni Basins' between the Lesser and Greater Caucasus, but the northern boundary between these foreland basin and Greater Caucasus stations is the same as here, and Forte et al. [2014] use the same division as we use here.

For stations defined as 'Lesser Caucasus' or 'Greater Caucasus', we calculate a smoothed $N25^\circ E$ velocity by taking the average within a moving 50 km window which is interpolated over the along-strike length of main the swath (dashed lines in the bottom of Figure S1). We calculate similar moving averages for the extremes of both datasets using the uncertainty on the GPS velocities (shaded regions in the bottom of Figure S1). We then use similar assumptions as Forte et al. [2014] and difference the Lesser Caucasus and Greater Caucasus velocities (Supplementary Table ??). This difference is interpreted as an approximation of the amount of convergence along the southern margin of the Greater Caucasus, with the remaining velocity of the Greater Caucasus accommodated as convergence within the range or along its northern flank. As described in [Forte et al., 2014], this is equivalent to treating the region as three non-deforming blocks (from south to north, the Lesser Caucasus (LC), Greater Caucasus (GC), and Eurasia (EU)) with parallel boundaries and subject to the relative velocity relationship,

$$_{EU}\mathbf{V}_{LC} = _{EU}\mathbf{V}_{GC} + _{GC}\mathbf{V}_{LC} \quad (S1)$$

where the red curve (Lesser Caucasus Velocity) in Figure S1 is $_{EU}\mathbf{V}_{LC}$, the blue curve (Greater Caucasus Velocity) is $_{EU}\mathbf{V}_{GC}$, and black curve (GC-LC Convergence) is $_{GC}\mathbf{V}_{LC}$. Comparisons between the ^{10}Be erosion rates and the velocity of the Lesser Caucasus or Greater Caucasus domains and convergence between them reveals some degree of correspondence (Figure S5).

Specifically, there is a loose positive correlation between Lesser Caucasus $N25^\circ E$ velocity and erosion rate (left panel, Figure S5) but less correspondence between Greater Caucasus $N25^\circ E$ velocity and erosion rate (center panel, Figure S5). The correspondence is similar to the Lesser Caucasus velocity if erosion rate is compared to the convergence between the Greater and Lesser Caucasus, i.e. the difference between the LC $N25^\circ E$ velocity and the GC $N25^\circ E$ velocity (right panel, Figure S5), suggesting that the erosion rates in these basins at least in part reflect the rate of shortening between the Greater and Lesser Caucasus. This hypothesis is further bolstered by recognizing that the one ^{10}Be basin which is a significant outlier (i.e. it has a high GC-LC convergence, but a relatively low erosion rate) is sample 16AF01, which was taken from the northern flank of the range and for which the rate of GC-LC convergence is not as directly relevant. Correlation coefficients for both the Lesser Caucasus and GC-LC convergence improve if the northern Greater Caucasus basin and the three Lesser Caucasus basins are removed.

2.5 Evaluating Influence of Lithology on Topography, Quartz Sourcing, and Erosion Rates

To assess the potential role that lithology plays in influencing our results, either in terms of variable sourcing of quartz or topographic statistics, for each sampled catchment we digitized available geologic maps and compiled lithologic information. Most sampled catchments were covered by at least one 1:200,000 scale geologic map in the Soviet geologic map series, specifically K-38-VII [Gamkrelidze and Kakhadze, 1959], K38-VIII [Melnikov and Popova, 1975], K-38-XIII [Dzhanelidze and Kandelaki, 1957], , K-38-XIV [Kandelaki and Kakhadze, 1957], K-38-XV [Kandelaki and Kakhadze, 1957], K-38-XVI [Krestnikov, 1957], K-38-XX [Gamkrelidze, 1958], and K-39-XXV [Khain and Shardanov, 1960], however some catchments in Azerbaijan were not (i.e. there are no 1:200,000 scale geologic maps published for these regions), and for those we relied on the 1:500,000 scale geologic map of Azerbaijan [Ali-Zade, 2005] along with more detailed unit descriptions from Alizadeh et al. [2016]. For the 1:200,000 scale Russian geologic map sheets, we transliterated individual map unit descriptions. As is the standard in the region, map units are defined chronostratigraphically as opposed to lithostratigraphically and map unit descriptions are often similar between map sheets, i.e. they may not be specific to the map sheet in question, but rather general descriptions of the lithologies of that age in the region. Consequently, the description of many map units reflect significant lithologic heterogeneity which required interpretation and classification of dominant rock types for each mapped unit. We defined 11 different lithologic categories: limestone and minor clastics, limestone and marl, limestone, marl, limestone and sandstone, sandstone and shale, sandstone and minor carbonate, shale, conglomerates, volcanics undifferentiated, phyllites and schists, and granite, and then classified each map unit as one of these categories based on the order in which lithologies were listed in the descriptions and field observations (Table S4). With these digitized lithologic classifications, we then used the functionality within TAK [Forte and Whipple, 2019] to calculate the percent of each catchment occupied by specific lithologies (Table S3).

For each catchment, we produced explorative plots to assess whether the distribution of lithologies had meaningful contributions to the topographic metrics (i.e. k_{sn} and slope gradient) of interest (Figures S24, S25, S26, S27, S28, S29, S30, S31, S32, S33, S34, S35,S36, S37, S38, S39, S40, S41, S42, S43, S44, S45, S46, S47, S48, S49, S50, S51, S52, S53, S54, S55, S56, S57, which appear at the end of this supplement). While many catchments exhibit at least some degree of correlation between values of k_{sn} or gradient and lithology, none of these patterns appear consistent, i.e. no particular lithology appears to always be steeper or shallower across catchments (Figure S7). The only lithologies that appear to have consistent k_{sn} or gradients, or values of either that differ substantially from the statistics of the population as a whole, are those which represent very small portions of the area and as such, we do not think this is diagnostic of the representation of a lithologic influence on topography, but rather a reflection of the topography of the specific catchments which include these lithologies.

More critically, given the documented extremely low quartz yields from all samples (e.g. Table S3), we also tested the sensitivity of the calculated erosion rates to variable quartz sourcing based on lithologic heterogeneity. We first recalculated appropriate latitudes and elevations for the production rate calculations again using the method of Portenga and Bierman [2011], but after filtering out portions of any catchments with dominantly carbonate lithologies, specifically those classified as 'limestone', 'limestone and marl', and 'marl'. We did not filter out 'limestone and minor clastics' and 'limestone and sandstone' as we assumed these units may still contribute sufficient quartz from their clastic constituents. We then used these updated elevation and latitude values in the online erosion rate calculator (Table S3) and paired this with mean basin k_{sn} values calculated excluding the same portions of each watershed. The calculated erosion rates, mean basin k_{sn} values, mean basin gradient, and pattern between erosion rates and either topographic metric was not appreciably different after filtering out these dominant carbonate lithologies (Figure S4)

Given the uncertainty in individual unit descriptions (and unknown quartz concentrations within the units), we additionally tested two end member schemes for calculation of production and erosion rates along with topography. For these schemes, we assumed that either all of the quartz was sourced from the bottom or top 50% of the catchment and calculated appropriate elevations and latitudes for use in the online calculator and topographic metrics for the respective portions of the catchments. Results from the erosion rate calculations are reported in Table S3. As with the lithological filtering, this experiment did not appreciably change the nature of the relationship between topography and erosion rate (e.g. Figure S4), thus generally we do not consider variable quartz sourcing as a source of uncertainty in the erosion rates and our subsequent conclusions.

2.6 Potential Divisions within k_{sn} and Erosion Rate Relationship

As discussed in the main text, the relationship between k_{sn} and ^{10}Be erosion rates are well described by a single relationship. However, to assess whether there may be meaningful ways to split the data that could complicate or undermine our analysis, we compared the variations in k_{sn} , gradient, and erosion rate against a variety of parameters including additional topographic metrics, lithology , and several climatic metrics (Table S3). Visuals of these relationships are provided here (Figure S8), though

as noted in the main text, while some co-vary with erosion rate and k_{sn} (e.g. maximum elevation), there do not appear to be robust ways of parsing the data based on any of these variables into populations with substantially different erosion rate - k_{sn} patterns. We also provide comparisons between erosion rate and mean basin gradient for each of these variables to show that it is also not possible to parse sensible relationships within this data if a different topographic metric is considered. It is interesting to note that the range of erosion rates above which k_{sn} becomes largely invariant (e.g. Figure S9) is similar to the range of erosion rates above which mean basin gradient also begins to reach threshold a threshold value, commonly associated with a critical limiting gradient [e.g., Roering et al., 2007]. This similarity explains why populations of basins within the Greater Caucasus exhibited a quasi-linear relationship between mean basin k_{sn} and gradient [Forte et al., 2016].

2.7 Fitting a Stream Power Incision Model Based Relationship Between k_{sn} and Erosion Rate

To fit a stream power incision model (SPIM) based power law relationship between k_{sn} and erosion rate, we fit the available data using two different methodologies, a bootstrap and a monte-carlo fit. We use these two methodologies as they represent two different approaches to assess the importance of outliers and consider the uncertainty ranges on the data in the fit parameters. We briefly these approaches below.

2.7.1 Bootstrap Approach

For this approach, we use bootstrap sampling, i.e. random sampling of a N member dataset with replacement to produce a bootstrap sample also with N members, but that may have multiple repeated entries. For example, bootstrap sampling of the array [1 2 3 4] could reproduce the array exactly or result in an array [1 1 1 1], etc. Each bootstrap sample draws from a set of k_{sn} - erosion rate pairs with their respective uncertainties, i.e. the relationships between k_{sn} and erosion rate for particular samples are preserved in the bootstrap sampling process. A fit (considering uncertainty) is performed on each bootstrap sample and this procedure is repeated an arbitrarily large number of times. Ultimately we are interested in the population of fit parameters, i.e. coefficients and exponents of the power law, and we can choose the most appropriate coefficient and exponent pair by finding the medians of these fit parameter populations. This bootstrap technique is explicitly designed to test the importance of outliers.

2.7.2 Monte-Carlo Approach

As an alternative approach, we test a monte-carlo scheme adapted from Adams et al. [2020]. Specifically, for each k_{sn} - erosion rate pair, we draw a single random sample from a normal distribution with the respective mean and a standard deviation set by the uncertainty on the measurement for that sample. For a given replicate, we produce a N member sampled dataset where each individual sample is represented by one k_{sn} - erosion rate pair. For each replicate sample, we perform a fit (with equal weighting, as the error in the values will be reflected in the range of k_{sn} - erosion rate values extracted for a given sample between replicates) and perform this an arbitrarily large number of times. As with the bootstrap technique, we consider the population of coefficients and exponents and select the median of these populations as the most representative values for the fit parameters. This approach is designed to try to simultaneously negate the tendency that high uncertainties lead to high erosion rate samples being ignored in error weighted fits while still reflecting that there is a wide range of acceptable values for k_{sn} - erosion rate pairs given the underlying uncertainty.

2.7.3 Performing the Fits

Within each different approach, we use the orthogonal distance regression (ODR) algorithm as implemented in SciPy and the k_{sn} -E relationship,

$$E = K(k_{sn})^n \quad (S2)$$

as a log-transformed version such that it is a linear fit using,

$$\log_{10}(E) = n * \log_{10}(k_{sn}) + \log_{10}(K) \quad (S3)$$

For both the bootstrap and monte-carlo fit, we perform 1e6 individual fits and then aggregate the population of fit parameters, i.e. values of K and n . We exclude data from sample 91416-1 for all fits because the uncertainty value for erosion rate is greater than the measured rate. We also perform a second set of fits where we exclude the two highest erosion rate basins (samples 90416-1 and 90216-2) and the two basins with lower χR^2 values (16AF01 and 90216-1, Figure S3) to estimate a more conservative set of parameters (Figure S11). We emphasize however that there is no specific reason to exclude the two high erosion rate samples, i.e. other than the erosion rate, there is nothing anomalous about these basins that cause us to question the validity of these rates.

For each population of fits, we use the median value (see bottom panel of Figure S11) of n and K to define the main curve. The shaded area is defined by the 25th and 75th percentile of the n and K values, specifically pairing the 25th percentile n with the 75th percentile K and vice versa. We use the median and quartile range because the bootstrap fit parameter distributions are skewed and thus the median and quartile range are less biased measures of the central tendency than the mean and standard deviation. For the main text and Figure 2, we only display the bootstrap fit result as its uncertainty range encapsulates the uncertainty range of the monte-carlo fit. Removing the two highest erosion rates and the two basins with some degree of disequilibrium does decrease the best bootstrap fit n value from 3.46 to 3.07 (primarily driven by the removal of the two high erosion rate basins), but (1) this lower n still implies a very nonlinear k_{sn} - erosion rate and thus does not appreciably change the result and (2) this lower median n is within the uncertainty bounds on the estimation of n from the fits that include these high erosion rate basins.

2.8 Discharge, Runoff, and Variability in the Caucasus in Gauged Basins

With our ultimate goal being the approximation of both mean runoff and runoff variability for the ungauged sampled ^{10}Be basins, we start with an analysis of gauged basins in the Caucasus region. Forte et al. [2016] presented such an analysis of available daily discharge data from gauged basins within the Caucasus region provided by the Global Runoff Data Centre (GRDC). Here, we use the same underlying dataset as Forte et al. [2016], but reprocess it to (1) describe variability with a power law right tail (i.e. inverse gamma, k) for use in equations related to the stochastic threshold incision model as in Forte et al. [2016], the tail of the discharge distributions were fit with a stretched exponential [e.g. Rossi et al., 2016] and (2) to remove potentially problematic basins from the dataset which may have anomalous discharges or variability. Specifically, using publicly available satellite imagery, we manually inspected the course of rivers within the GRDC basins and removed from the dataset any basins which had visible dams. As in Forte et al. [2016], we use a threshold of 99% to fit the tail of the discharge distribution. We provide a shapefile of the GRDC basins with relevant summary values in the attribute table in the GitHub repository.

To convert from discharge to runoff, we assume a simple relationship between drainage area and discharge,

$$Q = RA^c \quad (\text{S4})$$

where R is runoff, Q is discharge, and A is drainage area. We follow DiBiase and Whipple [2011] and assume $c = 1$, i.e. a linear relationship. This linear approximation appears valid, i.e. after accounting for spatial variation in rainfall rates, there is a quasi-linear relationship between discharge and drainage area (Figure 2). Results from this analysis are reported in Table S1. As discussed in the main text (and visible in Figure S10), the variability values are quite low (i.e. the k parameters are high). This is consistent with other analyses of runoff variability in the Caucasus region. Specifically Sutcliffe et al. [2008] analyzed a different, larger set of gauging stations and generally found low variability in runoff. More direct comparison of our results and those presented in Sutcliffe et al. [2008] are challenging as they characterize the runoff with generalized extreme value theory using a block maxima approach (which is appropriate given that they had access to monthly or annual maxima as opposed to daily data) where as we use a peaks over threshold approach.

2.9 Estimating Hydroclimatic Parameters in Ungauged Basins

2.9.1 Estimation of Mean Runoff

To estimate mean daily runoff in the ungauged ^{10}Be sample basins, we use a spatially continuous rainfall dataset (TRMM 3B42) to estimate runoff in ungauged basins (Figure 3). We first account for differences between precipitation as estimated from ground based precipitation stations, which are more appropriate for comparison with runoff data but are spatially discontinuous, and rainfall estimates from satellite observations. We use precipitation station data from the European Climate and Assessment Dataset (ECAD) [Klein Tank et al., 2002] for this purpose as this covers the majority of the area of interest and individual station data has been vetted. A shapefile of the mean precipitation for the relevant ECAD stations are provided in the GitHub repository. The underlying TRMM data is the same as that presented in Forte et al. [2016], see this publication for details. For each ECAD station, we extract the mean values of the corresponding TRMM pixel and then fit a linear relationship to the resulting population (Figure 3), which can be used to tune the TRMM rainfall estimates. This highlights that generally, before correction, there is relatively close agreement between the ground based ECAD stations and the TRMM data, though the relative disagreement increases at higher rates. Further, it suggests that on average TRMM tends to over predict total precipitation in the Caucasus region (i.e. the best fit line lies below the 1:1 line).

After correcting the TRMM data, we then calculate the mean basin rainfall within individual GRDC basins and then apply the correction to the TRMM data, which effectively shifts all of the rainfall to slightly lower magnitudes. From this, we then calculate the runoff ratio, i.e. $\frac{MDR}{MDP}$, and fit a linear relationship between the runoff ratio and corrected mean basin rainfall (Figure 3). From this relationship, mean basin rainfall (as estimated from the corrected TRMM) for any watershed can be converted to an estimated runoff ratio and the estimated runoff can be found by multiplying the mean basin rainfall by this estimated runoff ratio. The application of this procedure to the ungauged ^{10}Be sample basins is presented in Table S3. It is worth noting that generally, gauged basins with mean runoffs below 3 mm/day have mean basin rainfall rates that are greater than their runoffs, i.e. the runoff ratio is below 1. However, consistently for basins above 3 mm/day of gauged runoff, the mean runoff exceeds the mean basin rainfall, i.e. the runoff ratio is greater than 1. Consequently, the result of the linear fit between runoff ratios and mean basin rainfall implies that any basin with a mean rainfall rate of 4 mm/day or greater would have a runoff ratio >1 . We tested schemes where we assumed that runoff ratios could not exceed 1, i.e. we used the linear fit up to a mean rainfall of 4 mm/day and then assumed a runoff ratio of 1 above that threshold, so mean runoff would directly equal mean rainfall. These more conservative estimates of runoff did not appreciably change the results of later analyses that depend on the mean runoff, so we used the original fit values and runoff estimates, i.e. we allowed the runoff ratio to exceed 1.

As discussed in Forte et al. [2016], which also noted runoff ratios exceeding 1 in some of the high runoff GRDC basins using a similar methodology, we expect that this results from an underestimation of the precipitation at high elevations within the TRMM 3B42 data. TRMM 3B42 data is specifically known to underestimate precipitation that falls as snow at high elevations [e.g. Wulf et al., 2016]. Correction of the TRMM using the ECAD station data was meant to partially offset general disagreements between station and satellite precipitation measures, but the ability of our correction is limited by assuming a linear relationship (with the caveat being that we do not think a higher order polynomial or alternate form is warranted given the scatter in the data) and the relative lack of ECAD stations at high elevations (e.g. Figure 3).

2.9.2 Estimation of Runoff Variability

To estimate runoff variability, we take a similar approach as for estimating mean daily runoff, i.e. relating observed runoff variability in gauged basins to a spatially continuous parameter that can be used to estimate runoff variability in ungauged basins. We tested the efficacy of a variety of topographic and climatic metrics for this purpose and found that the two best predictors of runoff variability were the maximum elevation of the gauged watershed and the basin mean of the standard deviation of monthly mean snow cover (Figure 4). This latter metric was used by Forte et al. [2016] as a proxy for the relative importance of snow melt in generating runoff. We provide a georeferenced raster of the standard deviation of monthly mean snow cover in the GitHub repository.

Applying the linear relationships between maximum elevation and the standard deviation of monthly mean snow cover from the gauged basins allows us to estimate the variability for ungauged basins, specifically the ^{10}Be sample basins. The results of both of these approximations are reported in Table S3. For subsequent analyses that require the variability, we use the average of these two estimates for each basin.

2.10 Application of the Stochastic Threshold Incision Model

2.10.1 Review of Parameters within STIM

As described in the main text of the paper, we apply a stochastic threshold incision model (STIM) to our data, which is a modified form of a fluvial incision model that incorporates a threshold term, i.e. there is a minimum discharge below which no erosion occurs, and a stochastic distribution of flood discharges [e.g., Tucker and Bras, 2000, Lague et al., 2005, DiBiase and Whipple, 2011]. The details of this model are discussed in multiple other publications and we refer interested readers to Lague et al. [2005] or DiBiase and Whipple [2011] for more complete derivations, and discussion of the specific implementation we consider, but below we summarize some of the key components of the STIM with a specific focus on the parameters and their values that we use set to be able to use STIM.

We start with a simple relationship for instantaneous channel incision I ,

$$I = K\bar{Q}^m Q^{*\gamma} S^n - \Psi_c \quad (\text{S5})$$

where \bar{Q} is mean discharge, Q^* is normalized discharge such that $Q^* = Q/\bar{Q}$, and K is given by,

$$K = k_e k_t^a k_w^{-a\alpha} \quad (\text{S6})$$

the downstream discharge exponent m is,

$$m = a\alpha(1 - \omega_a) \quad (\text{S7})$$

the local discharge exponent γ is,

$$\gamma = a\alpha(1 - \omega_s) \quad (\text{S8})$$

the slope exponent n is,

$$n = \alpha\beta \quad (\text{S9})$$

the threshold parameter Ψ_c is,

$$\Psi_c = k_e \tau_c^a \quad (\text{S10})$$

where k_e is an erosional efficiency coefficient related to substrate erodibility, a is related to erosional process, k_t is a hydraulic factor including water density, gravitational acceleration, and a friction factor, k_w , ω_a , and ω_s are constants related to channel width, and α and β are constants depending on the frictional relationship assumed. If we assume that discharge Q is linearly related to drainage area A via mean runoff \bar{R} such that $\bar{Q} = \bar{R}A$, we can substitute this and the relationship for channel steepness to recast this incision law in terms of k_s ,

$$I = K \bar{R}^m Q^{*\gamma} k_s^n - \Psi_c \quad (\text{S11})$$

Either form of this instantaneous incision rate is equivalent to the erosional component of the stream power incision law (main text equation 1) if Q in Q^* is treated as temporally constant and equal to the mean, i.e. $Q^* = 1$, and the critical shear stress τ_c is assumed to be negligible at this mean discharge, i.e. $\Psi_c \approx 0$.

To consider the impact of both a threshold for incision, i.e. a non-zero Ψ_c term, and the temporal variability of discharge, i.e. how often incision occurs will be a function of the critical shear stress and how often and for how long this critical shear stress is exceeded, it is necessary to integrate the instantaneous incision law across a range of discharges. This long term average incision rate, \bar{I} , can be expressed as,

$$\bar{I} = \int_{Q_c^*}^{Q_m^*} I(\bar{Q}, Q^*, S) pdf_{\bar{Q}k}(Q^*) dQ^* \quad (\text{S12})$$

or in the context of equation S11,

$$\bar{I} = \int_{Q_c^*(k_s)}^{Q_m^*} I(Q^*, k_s) pdf_{\bar{Q}k}(Q^*) dQ^* \quad (\text{S13})$$

where Q_c^* is the minimum discharge that will overcome τ_c and Q_m^* is the maximum discharge observed within the considered time frame. We follow Lague et al. [2005] and consider the probability distribution of discharge $pdf_{\bar{Q}k}$, as

$$pdf_{\bar{Q}k} = \frac{k^{k+1}}{\Gamma(k+1)} \exp\left(-\frac{k}{Q^*}\right) Q^{*(2+k)} \quad (\text{S14})$$

where Γ is the gamma function and k is a variability parameter which describes the shape of the tail of the distribution of discharges, where lower values of k represent greater degrees of discharge variability.

Ultimately, we are primarily interested in the relationship between channel steepness, k_s and average incision rate \bar{I} . As shown in Lague et al. [2005], equation S12 can be solved using different assumptions and rearranged to relate channel steepness to incision rate. Specifically, if it assumed that if Q_c^* is negligible with respect to the incision rate, i.e. a constant discharge case, then k_s can be expressed as,

$$k_s = K^{-\frac{1}{n}} \bar{R}^{-\frac{m}{n}} \left(\frac{\Gamma(k+1) k^{-\gamma}}{\Gamma(k+1-\gamma)} \right)^{\frac{1}{n}} (\Psi_c + \bar{I})^{\frac{1}{n}} \quad (\text{S15})$$

If alternatively Q_c^* is large compared to the incision rate, then k_s can be approximated with,

$$k_s \approx K^{-\frac{1}{n}} \bar{R}^{-\frac{m}{n}} \left(\frac{(k+1)(k+1-\gamma)\Gamma(k+1)}{k^{k+1}\gamma} \right)^{\frac{\gamma}{n(k+1)}} \Psi_c^{\frac{k+1-\gamma}{n(k+1)}} \bar{I}^{\frac{\gamma}{n(k+1)}} \quad (\text{S16})$$

These two equations represent end member relationships with equation S15 only being appropriate when incision rate is very high and/or thresholds are negligible (i.e. Regime III) and equation S16 is only appropriate at very low incision rates and/or when thresholds are high (i.e. Regime I). For most cases (i.e. Regime II), in order to relate k_s to incision rate it is instead necessary to numerically solve equation S13. For the STIM curves that appear in the main text we use this numerical integration approach (i.e. Regime II), but we show solutions for equations S15 and S16 in Figure S19 for reference. What can be noted there is that the Regime II curve collapses to the Regime I curve at very low erosion rates and k_{sn} and collapses to the Regime III curve at very high erosion rates and k_{sn} . Our implementation of the STIM relationships are provided in the GitHub repository as *stochastic_threshold.py*.

In the context of using the STIM to explain the observed k_{sn} - erosion rate relationship, we focus on understanding the variation in mean discharge/runoff and discharge/runoff variability. As discussed later, while other parameters are important in controlling the form of the k_{sn} - erosion rate relationship, these are either extremely difficult to constrain (e.g. k_e) or we lack the primary field observations / measurements to adequately parameterize them (e.g. τ_c or ω_s) and so must make assumptions.

2.10.2 Parameterization of the STIM Relationship in the Caucasus

From the prior results, for each erosion rate basin, we have estimates of the mean runoff and runoff variability (Table S3), but to explore the extent to which STIM relationship, considering these runoffs and variabilities, explains the observed patterns between ^{10}Be erosion rates and k_{sn} , we must assign, or estimate, values for the other parameters in equations S11 and S13. We list the values used and their associated units below:

- k_e : Variable : $m^{2.5} s^2 kg^{-1.5}$
- R : Variable : $m^1 s^{-1}$
- k : Variable : Dimensionless
- τ_c : 45 : Pa
- k_w : 15 : $m^{-0.5} s^{0.5}$
- k_t : 1000 : $m^{-7/3} s^{-4/3} kg$
- ω_a : 0.5 : Dimensionless
- ω_s : 0.25 : Dimensionless
- a : 3/2 : Dimensionless
- α : 2/3 : Dimensionless
- β : 2/3 : Dimensionless

We assume a Darcy-Weisbach friction relation and set $\alpha = \beta = 2/3$, follow Tucker [2004] and set $k_t = 1000$, such that $k_t = \rho_w g^{2/3} C_f^{1/3}$ where $C_f = 0.08313$, and we set $a = 3/2$, which assumes unit stream power. We do not have direct field observations with regards to channel width or cross sectional form, so for ω_s we use a value of 0.25 consistent with a concave channel cross section and between the expected range of 0 to 0.5 [Lague et al., 2005]. With $\omega_s = 0.25$, we set $\omega_a = 0.50$ so that the ratio of m/n , i.e. the concavity, equals 0.5 to be consistent with the reference concavity we use to calculate k_{sn} .

For k_w , which is the coefficient on the power law relationship between channel width, w , at a given discharge Q ,

$$w = k_w Q^{\omega_a} \quad (\text{S17})$$

we use a value of 15, which is the same value used by DiBiase and Whipple [2011]. To explore whether this choice of k_w is appropriate, it is necessary to compare the predictions for channel width implied by this value, along with the value of ω_a , to field measurements of width. In the absence of such field measurements, we use the 'ChanGeom' tool [Fisher et al., 2013], which can be used to measure channel widths on high resolution satellite imagery. Careful measurements using this tool have been shown to be similar to field measured widths in both the Himalaya and Taiwan [e.g. Fisher et al., 2013, Yanites et al., 2018]. Specifically, we use freely available imagery in Google Earth to map channel widths and the methodology of Yanites et al. [2018] in which we map the extent of largely vegetation free, gravel areas surrounding channels, with the assumption being that this represents areas which experience flows often enough to suppress the establishment of vegetation. Where clear edges of terraces into which this channel belt are cut, we use this as the edge of the channel. At larger drainage areas, this often represents a channel width that is significantly wider than the visible channel occupied by water in a single given satellite image (Figure S12).

The choice to map channels in this manner is in part based on field observations where these gravel areas are routinely inundated during higher flow events or after individual rain storms along with the variability in channel width and position (i.e. the width of the area occupied by water) observed in different satellite images taken over different years which are available within Google Earth. This means that some portion of the channel width measurements are biased towards widths largely relevant for discharges higher than the mean. In other areas, only the channel occupied by water is visible within the imagery, usually due to tree cover, so in these cases, we mapped this as the channel width. Together, our channel width measures are likely a mixture of widths relevant for mean discharges and those for higher, moderate flood discharges depending on local conditions and available imagery.

Using this methodology, we were able to measure channel widths for 26 of the 34 erosion rate basins. For the other 8 basins, the imagery available was insufficient to measure channel widths largely because the channels were completely obscured by tree cover. The results of these channel width measurements as a function of drainage area are presented in Figure S13. The underlying data for this plot and plotting algorithm are also provided in the GitHub repository.

We use the width estimates to evaluate the choice of $k_w = 15$ and $\omega_a = 0.5$, specifically by combining equation S4 and S17 to derive a relationship between width, runoff, and drainage area,

$$w = k_w R^{\omega_a} A^{\omega_a c} \quad (\text{S18})$$

We again assume $c = 1$ and use the discharge data for the gauged basins to calculate runoffs, R , at the mean discharge and a moderate flood, i.e. the discharge associated with the 2-year flood. We then evaluate this relationship at a series of reference drainage areas that span the areas within our measured width data. Comparisons between the predicted width-drainage area relationship and those measured suggest reasonable agreement, and thus that the choice of k_w and ω_a appear appropriate (Figure S13). At a given drainage area, the predicted widths also span much of the range of measured widths and further highlight that our measurements likely reflect a mixture of widths reflective of mean discharges and higher, moderate flood discharges. It is also worth highlighting that the lack of a clear relationship between channel width and mean basin erosion rate suggests that adjustment of channel width as opposed to slope is not a robust explanation for the $k_{\text{sn}}\text{-}E$ pattern in the Greater Caucasus. This analysis does assume there is no specific difference in the relations between width, drainage area, runoff, and discharge within the gauged basins compared (which we use to calculate the width for the mean and 2 year flood event) and the erosion rate basins (which we used to measure the widths). Given that we are already assuming some amount of correspondence between behavior in the gauged basins and erosion rate basins to estimate mean runoff and variability, we consider this appropriate.

This finally leaves k_e and τ_c as the two remaining unconstrained or assigned variables in the STIM equations. τ_c can be estimated from the grain size distribution within channels [e.g., DiBiase and Whipple, 2011], but we presently do not have (and are not aware of any published) estimates of grain size distributions for streams in the Greater Caucasus. In the absence of such grain size data, we first use a fixed τ_c of 45 Pa. Relating this back to grain size and using a Shields criterion with a critical Shields stress of 0.3 and densities for sediment (ρ_s) and water (ρ_w) densities of 2700 and 1000 kg*m⁻³ respectively [after DiBiase and Whipple, 2011],

$$\tau_c = 0.3(\rho_s - \rho_w)D_{50} \quad (\text{S19})$$

a τ_c of 45 Pa corresponds to a D_{50} of 90 mm. We consider this a reasonable approximation as this lies between the median (79 mm) and mean (107 mm) of the large compilation of D_{50} values from a variety of different types of steep mountain streams [e.g. Palucis and Lamb, 2017].

Fixing τ_c to 45 Pa, we then estimate acceptable ranges of k_e values. For each sampled basin, we use the assigned parameter values as described above, the estimated mean runoff and runoff variability, and the measured basin averaged k_{sn} , to find the k_e value for that basin that will best reproduce the measured basin averaged ¹⁰Be erosion rate. In this estimation, we also wish to account for the uncertainty on both basin averaged k_{sn} and erosion rate, so for each basin, we generate a synthetic set of k_{sn} and erosion rates drawn for a normal distribution centered on the observed value and with a standard deviation equal to the uncertainty. We then minimize the root mean squared error between these populations of synthetic erosion rates and erosion rates calculated from the STIM relationship using the corresponding population of synthetic k_{sn} . This results in a wide range of k_e values that have a quasi-linear relationship with estimated mean runoff, but not runoff variability (Figure 6). These estimated k_e values have no meaningful relationship with lithology (Figure S14). The algorithm to perform this optimization is provided in the GitHub repository as *optimize_k_e.py*.

2.10.3 Comparison of SPIM and STIM Relationships

Comparison of the best fit SPIM relationship from the bootstrap fitting, the SPIM relationship using the median values, or the best fit SPIM relationship all reveal similar residuals and root mean squared errors (Figure S16). Depending on whether residuals for k_{sn} or erosion rates are considered, either the SPIM or STIM have slightly better performance, at least using the RMSE as a determinant. In detail, for residuals on k_{sn} , both versions of the STIM are more uniform with respect to the residual values through a range of erosion rates, where as the SPIM has lower residuals for low k_{sn} -E pairs and higher residuals for high k_{sn} -E pairs (Figure S16 - top row). For residuals on erosion rates, the SPIM better matches the erosion rates at low k_{sn} ($<\sim 250$), whereas STIM using the median values better matches the erosion rates at moderate to high k_{sn} (between ~ 375 -425) and both fail to meaningfully explain several samples. The algorithms to calculate a best fit using the STIM relationship (*stim.fit.py*) and calculate the RMSE and residuals (*residuals.py*) are provided in the GitHub repository.

2.10.4 Cluster Analysis of STIM Relationship

While this median STIM relationship qualitatively does reproduce the general shape of the observed k_{sn} - erosion rate relationship and some of the along-strike patterns in k_{sn} , this can be refined considering that there is a wide range in both mean runoff and runoff variability from our estimates. To investigate this, we identify populations within the basins as defined by the estimated mean runoff and variability using a k-means clustering analysis. The data was scaled prior to cluster analysis using the 'StandardScaler' in scikit-learn such that the mean of each variable is 0 and the standard deviation is 1. We tested cluster values of 1-14 and found that 3 clusters was the ideal based on a 'elbow plot' (Figure S17). The algorithm to do the cluster analysis is provided in the GitHub repository in *cluster_analysis.py*.

For each cluster, to generate the STIM relationship, we again used the median values of the runoff and variability parameters for the respective cluster, but keep k_e fixed to the median of the entire population. Cluster 1 (Very-low variability and moderate runoff) and Cluster 2 (Low variability and moderate runoff) are moderately well explained by the resulting STIM relationships, however Cluster 3 (High runoff) is not (Figure S19).

We can compare the relative performance of the clustered STIM relationships vs the whole population median STIM relationship by comparing the predicted vs observed erosion rates implied by each (Figure S21). To generate the ranges in predicted erosion rates, we used the standard deviations of the clustered populations of mean runoff and variability as uncertainty bounds for calculating implied erosion rates. For this, we assumed that higher mean runoffs would tend to be characterized by lower variability (higher values of k) and vice versa, i.e. the bounds on predicted erosion rates are constructed by pairing the upper bounds of R and k and pairing the lower bounds of R and k . We did not account for uncertainty on k_e in this analysis. We performed this either using the STIM relationship implied by the respective cluster (Left panel of Figure S21) or by the population median STIM relationship (Right panel of Figure S21). For the population median STIM relationships, the significantly larger error bars in predicted erosion rate reflect the larger magnitude of standard deviations on R and k for the whole population. While neither is perfect, for the majority of the data (excluding those in Cluster 3), the clustered STIM relationship is a better (Cluster 2) or similar (Cluster 1) predictor of erosion rates.

3 Supplemental Table Captions

Tables are provided as excel files as supplementary documents. The data in these tables are reproduced as text files (though spread across a wider number of files) in the GitHub repository. Below we provide captions for the supplementary tables referenced in the main text and this document.

3.1 Table S1

Summary of topographic, rainfall, and discharge statistics for gauged basins from the Global Runoff Data Centre (GRDC).

3.2 Table S2

Location of all samples collected in the Caucasus region and the result of these samples (either Data, indicating that we report a ^{10}Be erosion rate for this basin, Failed with reason for failure specified, or Not Analyzed).

3.3 Table S3

Master table reporting data for the basins for which we report ^{10}Be erosion rates. This excel table has multiple sheets:

Topography: Basic topographic statistics and sample location for analyzed basins.

Climate: Mean climatological variables, including interpreted mean runoff and variability for analyzed basins.

Lithology: Lithologic breakdown of each basin along with the mean k_{sn} and mean hillslope gradient calculated for areas occupied by each lithology within a given basin. NaN entries mean k_{sn} and mean hillslope gradient columns indicate that this lithology was not present in that basin.

Quartz Masses: Total mass of sample processed, the mass after Aqua Regia leaches, the mass of quartz dissolved for ^{10}Be analysis, and the yield of quartz in the context of total mass processed.

Be Measurements: Raw measurements of Be concentrations and associated measurements necessary to recalculate erosion rates.

Be Blanks: Raw measurements of Be concentrations of blanks associated with various samples as reported in the "Be Measurements" tab.

CRONUS v3 Inputs: Input for CRONUS v3 calculator for main erosion rates (no filtering). This in the format for direct input to CRONUS v3.

Main Erosion Rates: The output erosion rates from CRONUS v3 for main erosion rates (no filtering) reporting the results from the three different scaling schemes. Note that we use the time independent St (Stone) scheme in the main text.

CRONUS v3 Litho Inputs : Input for CRONUS v3 calculate for lithologically filtered erosion rates.

Litho Erosion Rates: The output erosion rates from CRONUS v3 for lithologically filtered erosion rates.

CRONUS v3 Low Z Inputs : Input for CRONUS v3 calculate for erosion rates assuming contribution only from lower half of basin.

Low Z Erosion Rates: The output erosion rates from CRONUS v3 for erosion rates assuming contribution only from lower half of basin.

CRONUS v3 High Z Inputs : Input for CRONUS v3 calculate for erosion rates assuming contribution only from upper half of basin.

High Z Erosion Rates: The output erosion rates from CRONUS v3 for erosion rates assuming contribution only from upper half of basin.

3.4 Table S4

Summary of the synthesis of geologic maps for the Caucasus region. Included are the relevant map sheet designation from the Soviet Geologic Map Series, the original unit identifier, the interpreted age from this unit identifier, the full transliterate description, and then the interpreted rock type from this description.

4 Supplemental Figures and Captions

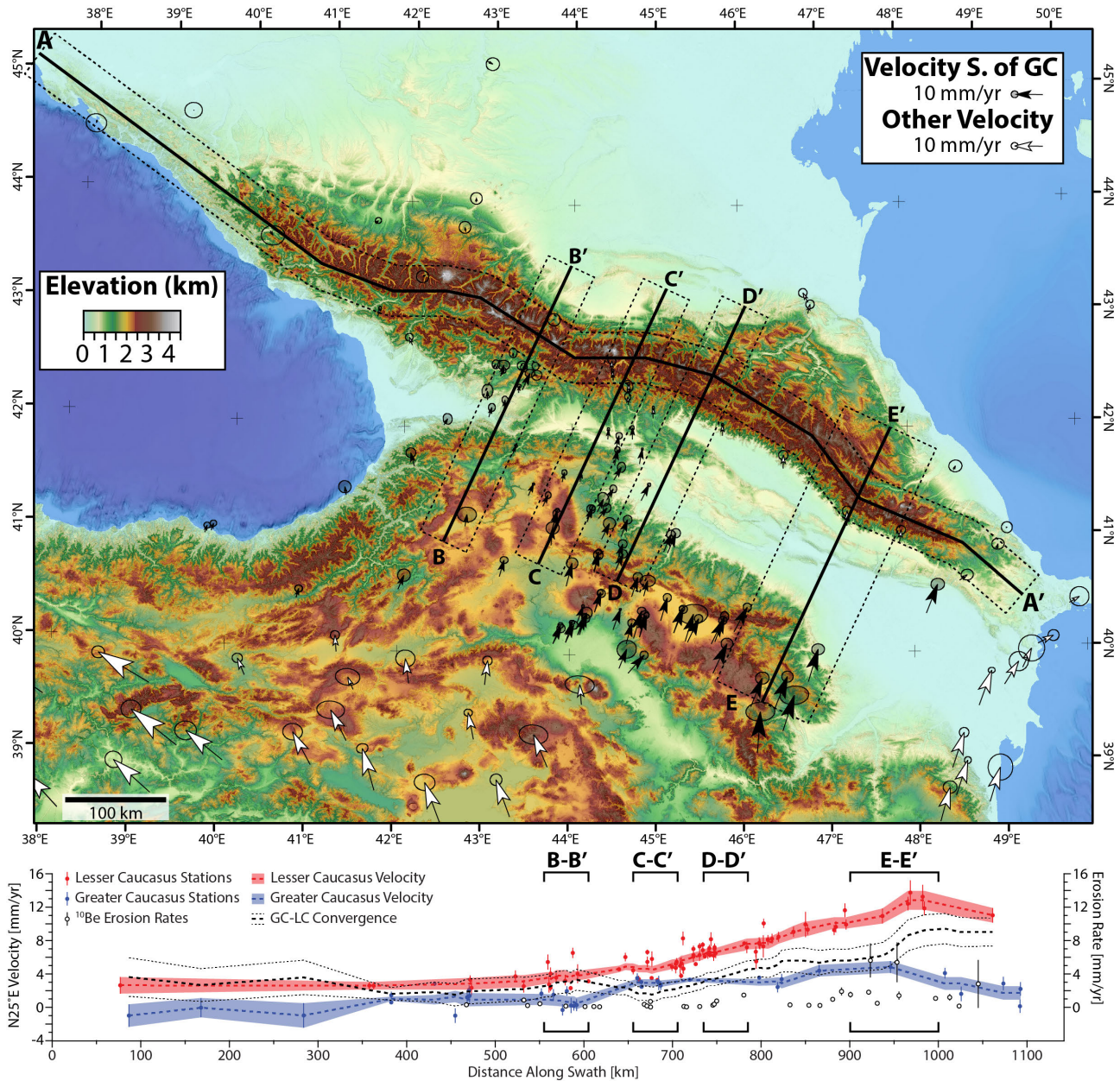


Figure S1: GPS stations within the Greater Caucasus regions from Reilinger et al. [2006], Kadirov et al. [2012], Sokhadze et al. [2018]. Black stations are used for the estimation of along-strike convergence rate shown in the bottom plot. GPS swath is the same as in Figure 1.

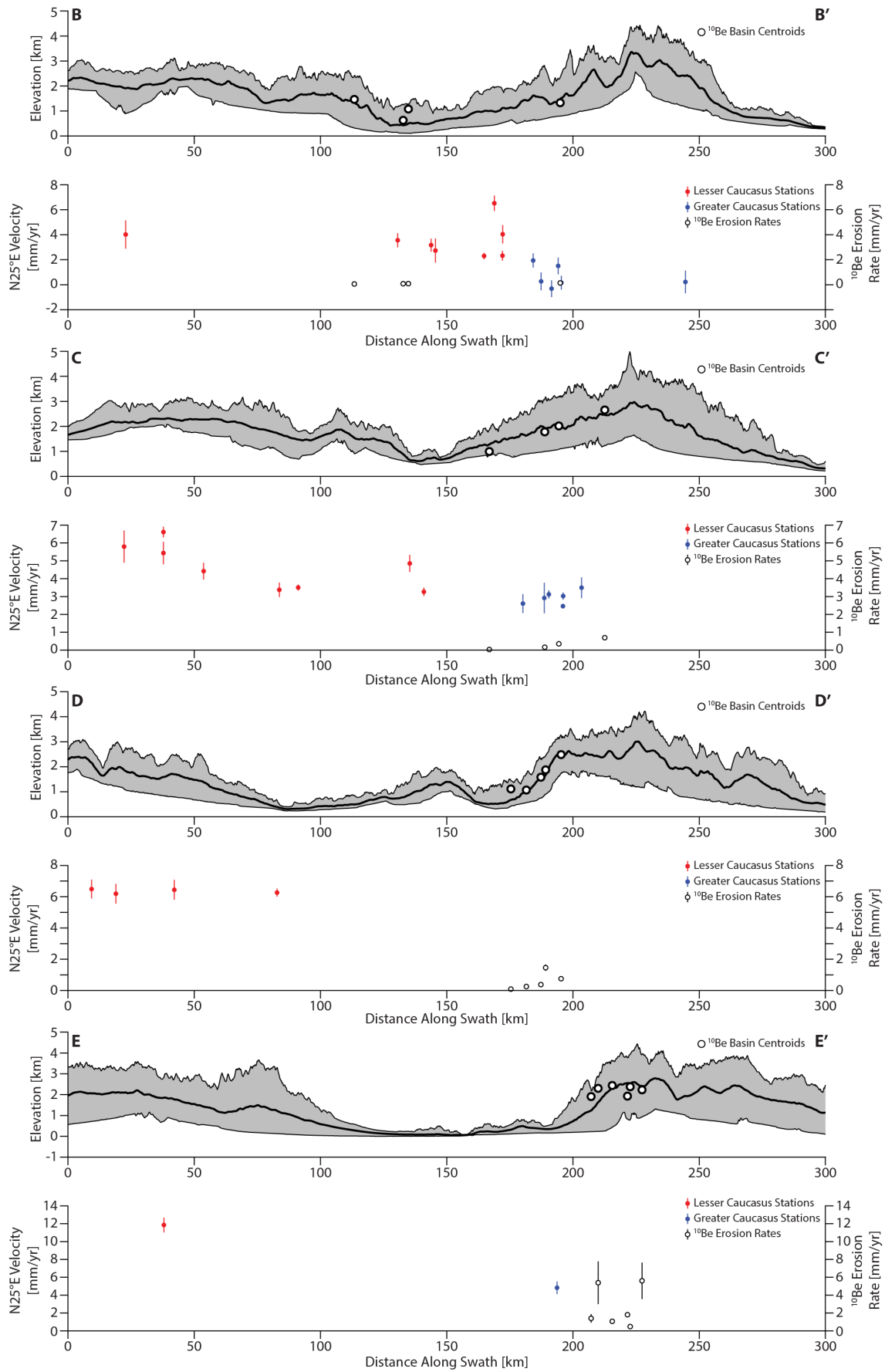


Figure S2: Across strike swath showing correspondence between GPS velocities and erosion rates, see Figure S1 for location).

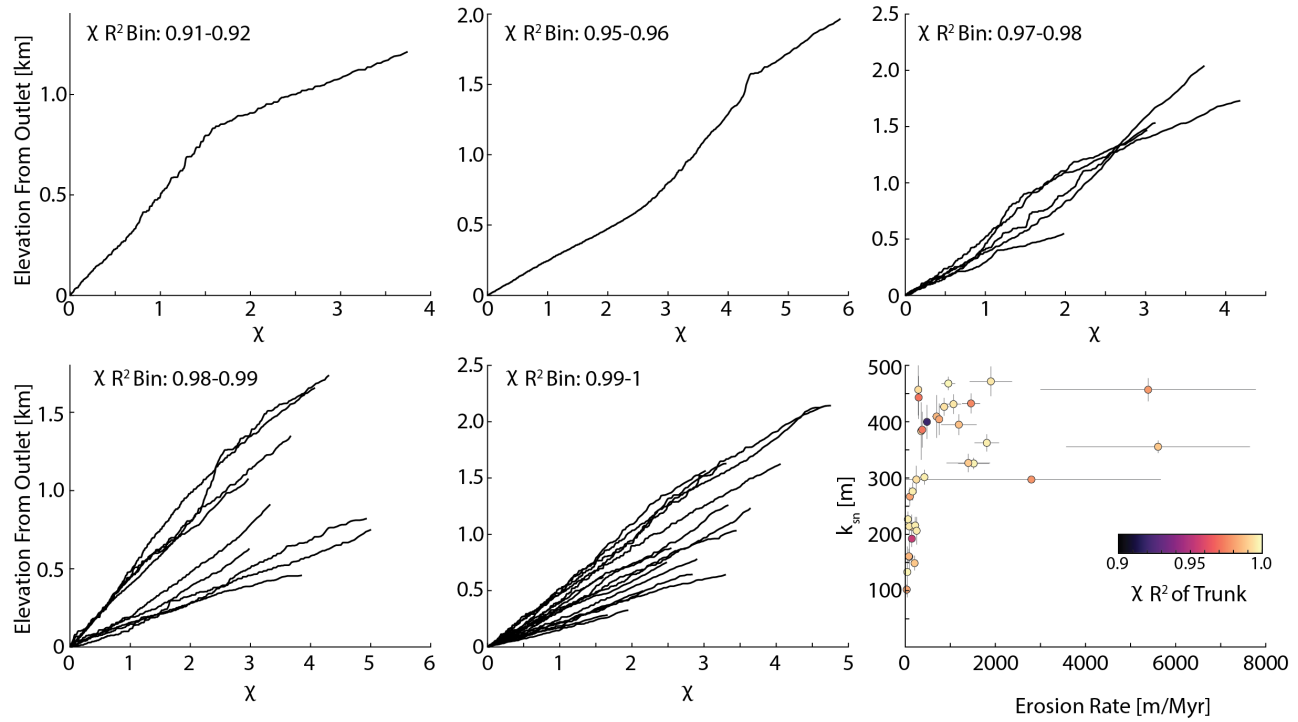


Figure S3: χ - elevation plots of the trunk streams of individual basins, binned by the χR^2 of the trunk stream, and k_{sn} vs erosion rate colored by the χR^2 of the trunk stream.

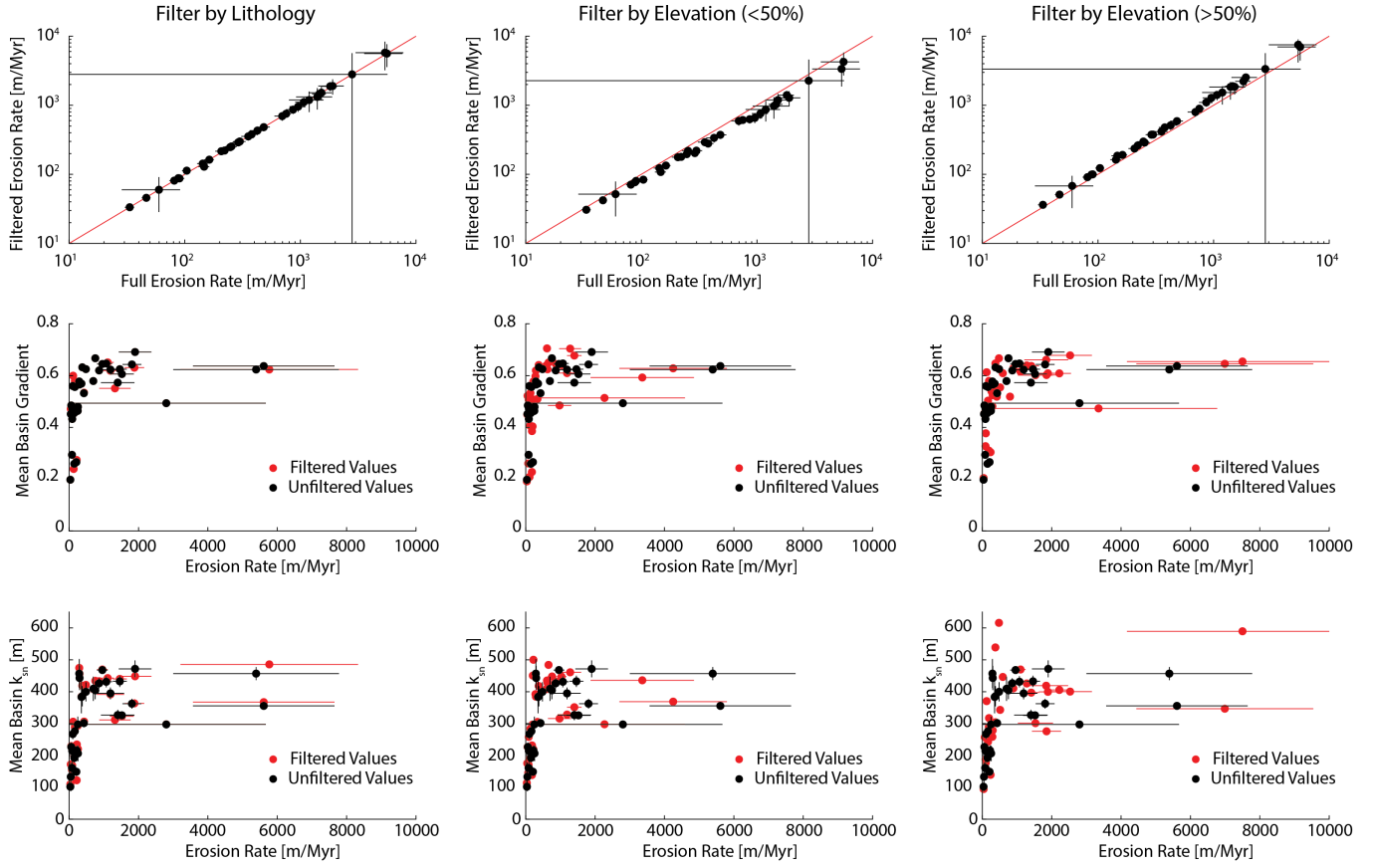


Figure S4: Comparison between erosion rates and mean basin k_{sn} as used in the main text and three different strategies for assessing the sensitivity to quartz sourcing.

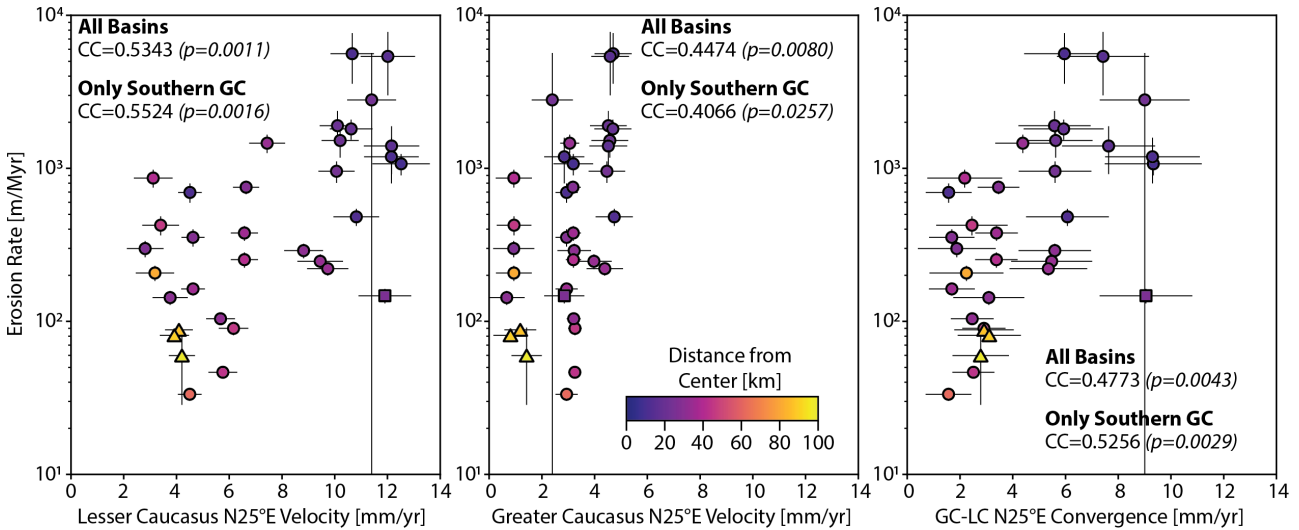


Figure S5: Comparison between Lesser Caucasus N25°E velocity (left), Greater Caucasus N25°E velocity (center), convergence between the Greater and Lesser Caucasus (right), and ^{10}Be erosion rates. Square basin is in the northern Greater Caucasus and triangle basins are in the Lesser Caucasus. Correlation coefficients (CC) and corresponding p values are shown for the respective relationships.

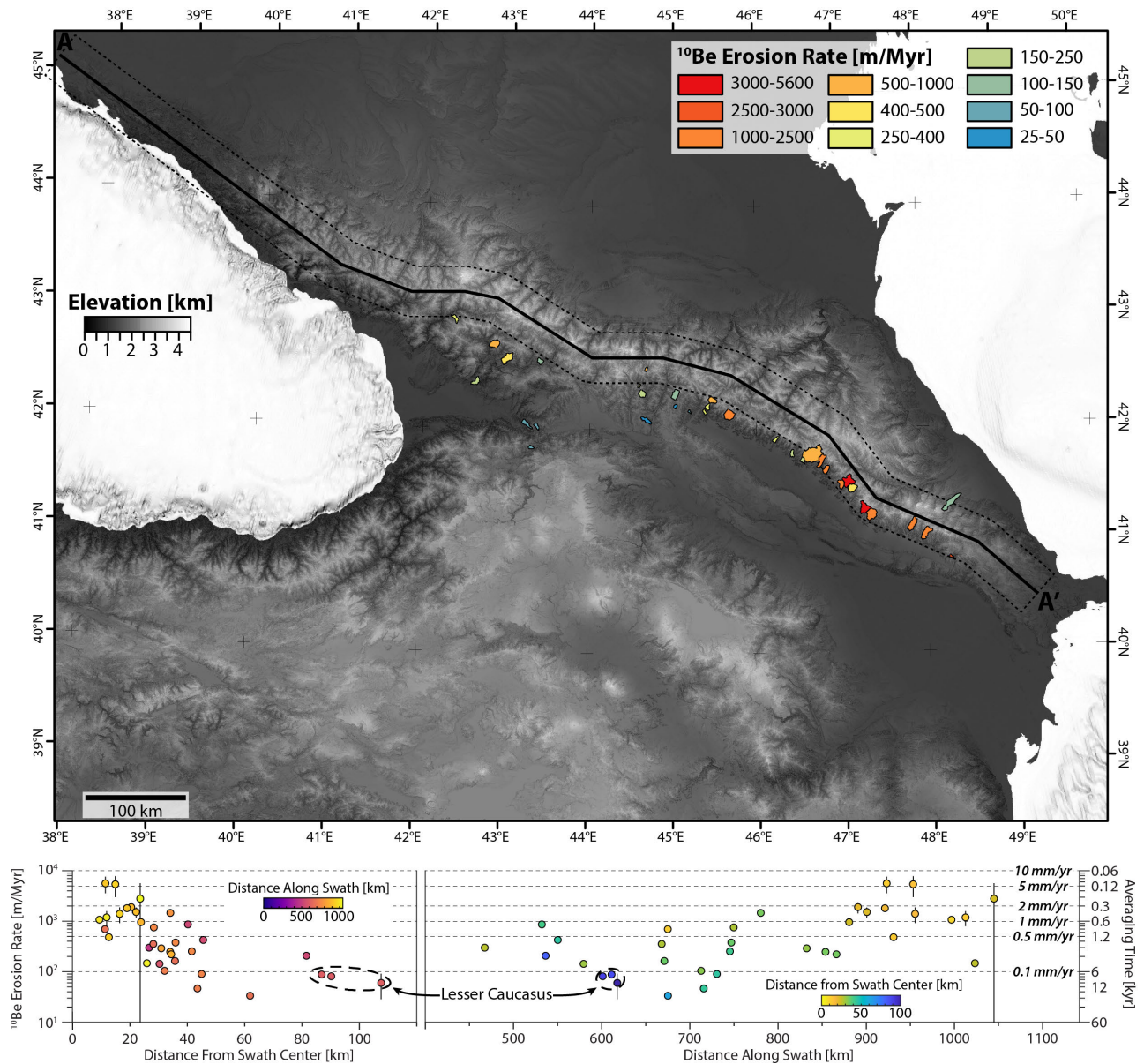


Figure S6: Erosion rate basins and their position along the swath (right) and from the center line of the range (left), which approximates the topographic crest of the range.

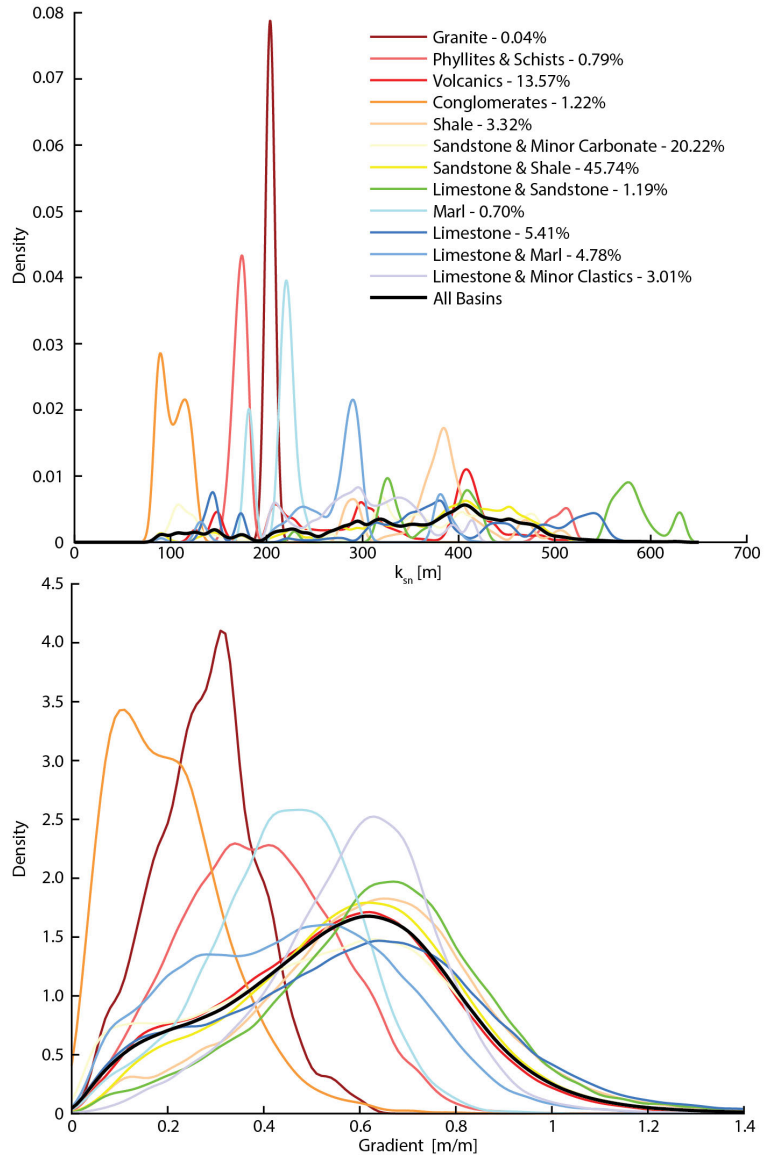


Figure S7: Kernel density estimates of k_{sn} (top) and gradient within specific lithologies. Percentages within explanation represent the fraction of the area within the entire population of sampled watersheds occupied by that lithology.

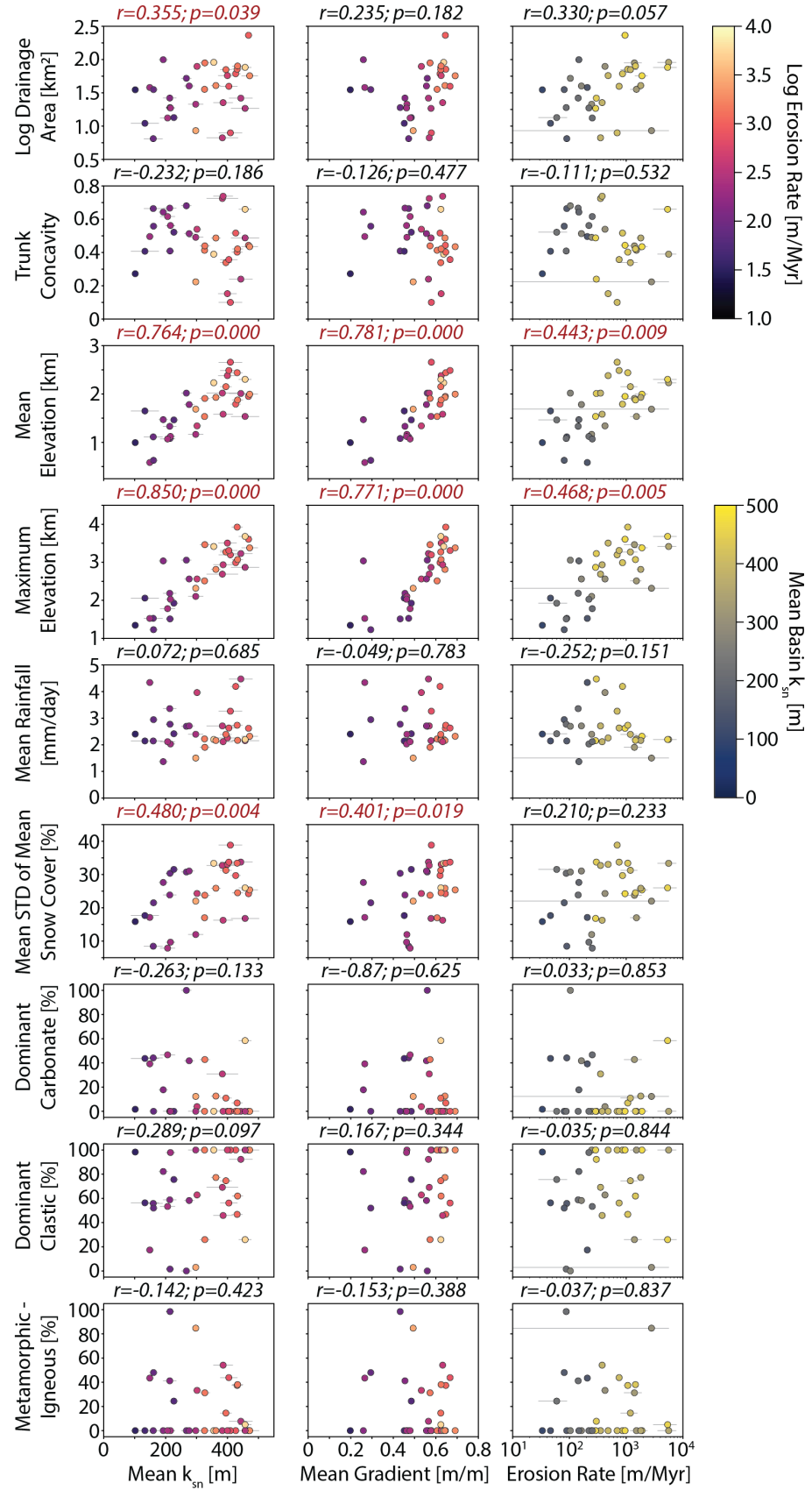


Figure S8: Comparisons of mean basin k_{sn} (left column), gradient (center column), and ^{10}Be (right column) against various other values. Pearson's correlation coefficient and significance (p-value) are shown for each relationship, those colored in red indicate a p value suggesting the relationship between the two variable is significant at the 95% confidence level.

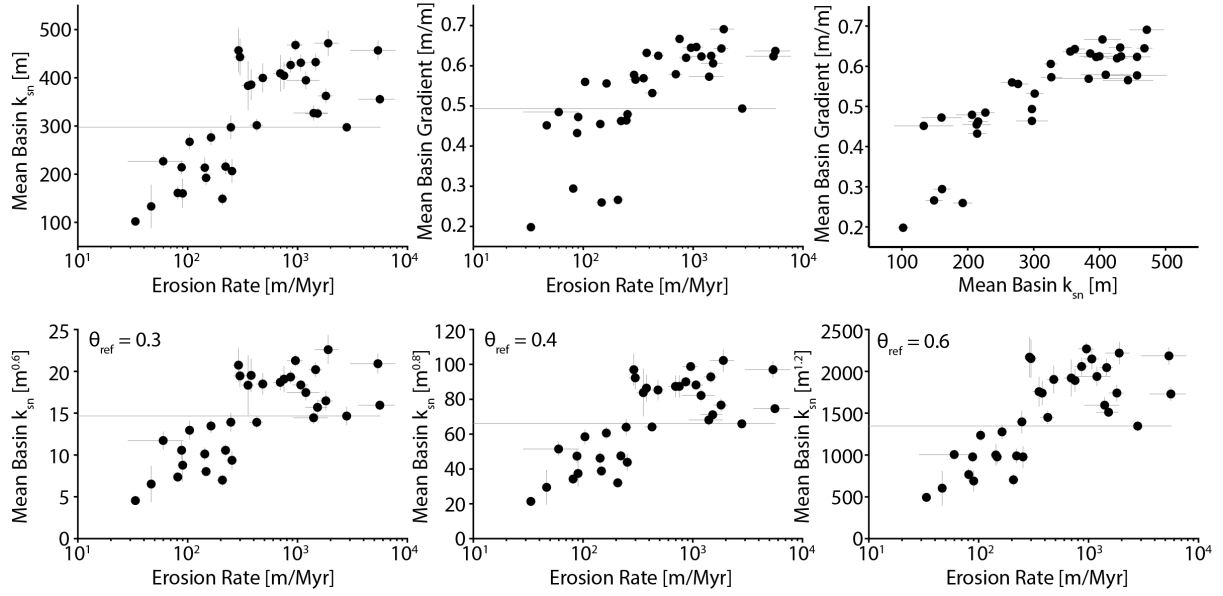


Figure S9: Top row shows basic relationships between k_{sn} , gradient and ^{10}Be erosionr rates. Bottom row shows k_{sn} - ^{10}Be relationships with k_{sn} calculated at different θ_{ref} values.

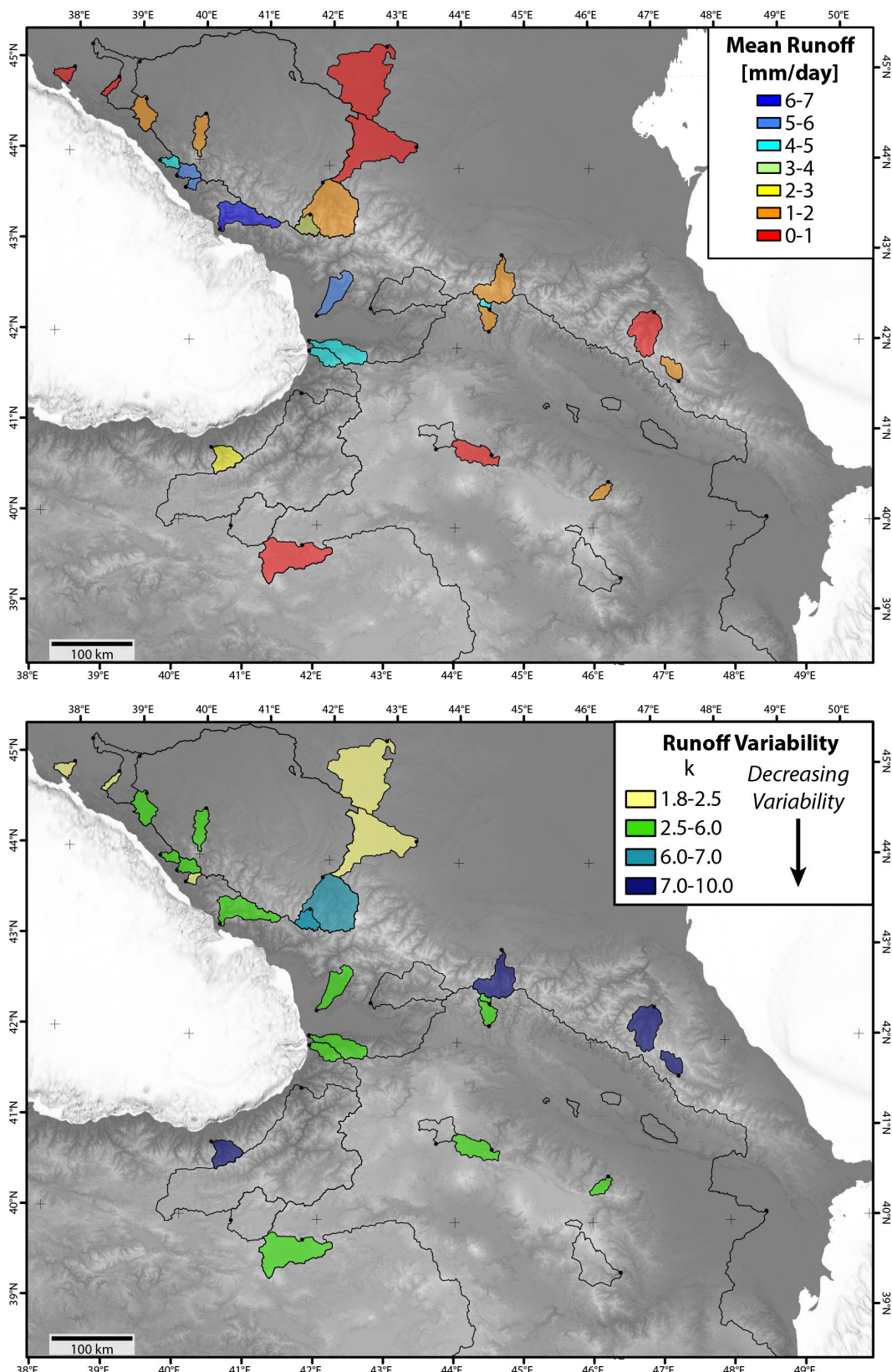


Figure S10: Upper: Mean daily runoff for GRDC basins used in this analysis. Basins without coloring are GRDC watersheds removed due to the presence of dams. Lower: Power law right tail (i.e. inverse gamma, k) of runoff distributions to characterize variability.

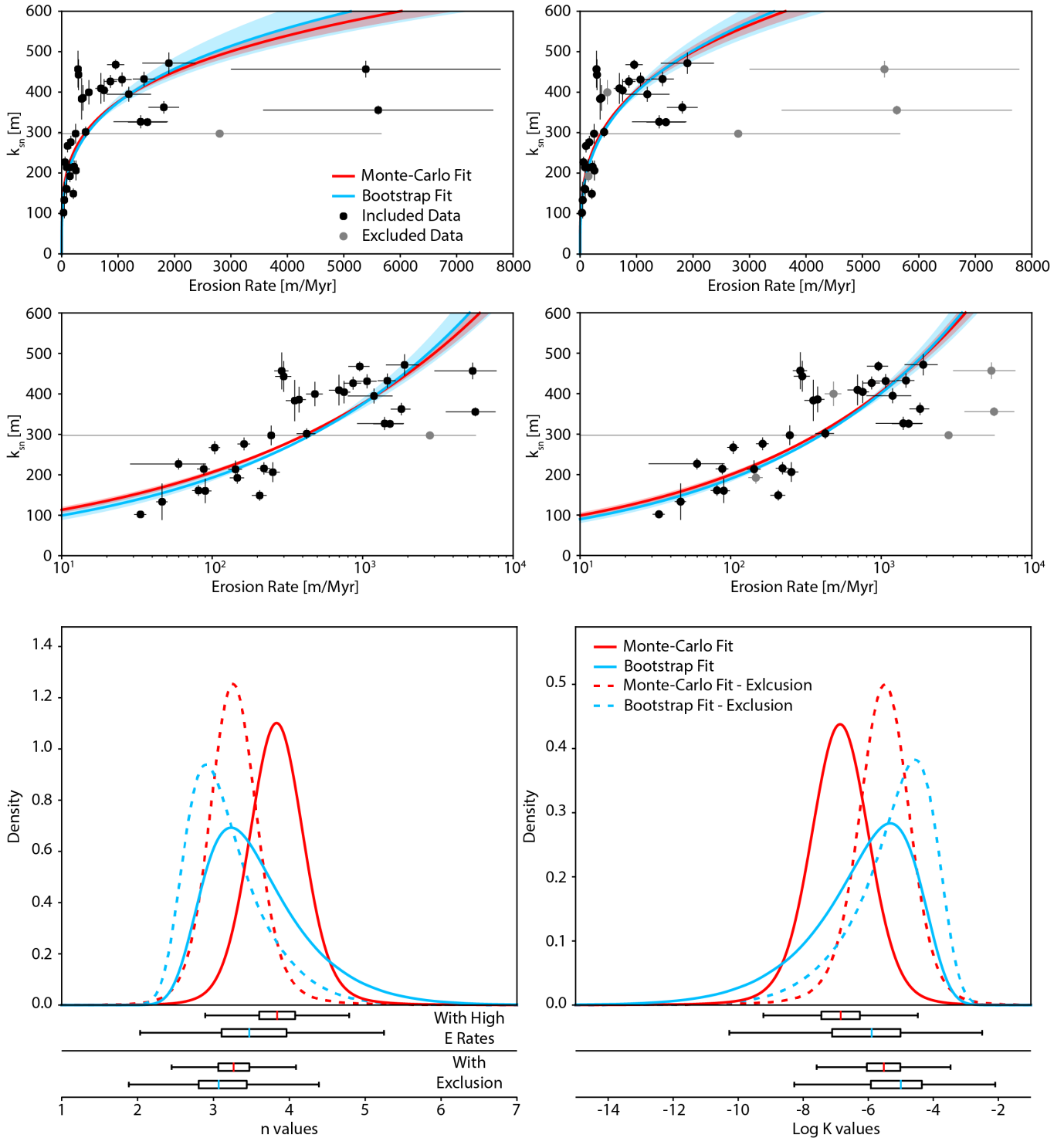


Figure S11: Power law fits to the data using log-transformed for both bootstrap and monte-carlo. Fits excluding the two highest erosion rate basins are also included. Box and whisker plots show median value with the colored line (which is used for the solid line relationship in plots above) and extent boxes represent the 25th and 75th percentiles (which are used to define the shaded regions in plots above).



Figure S12: Example of definition of channel widths using Google Earth imagery, red line in right image represents the mapped extent of the channel.

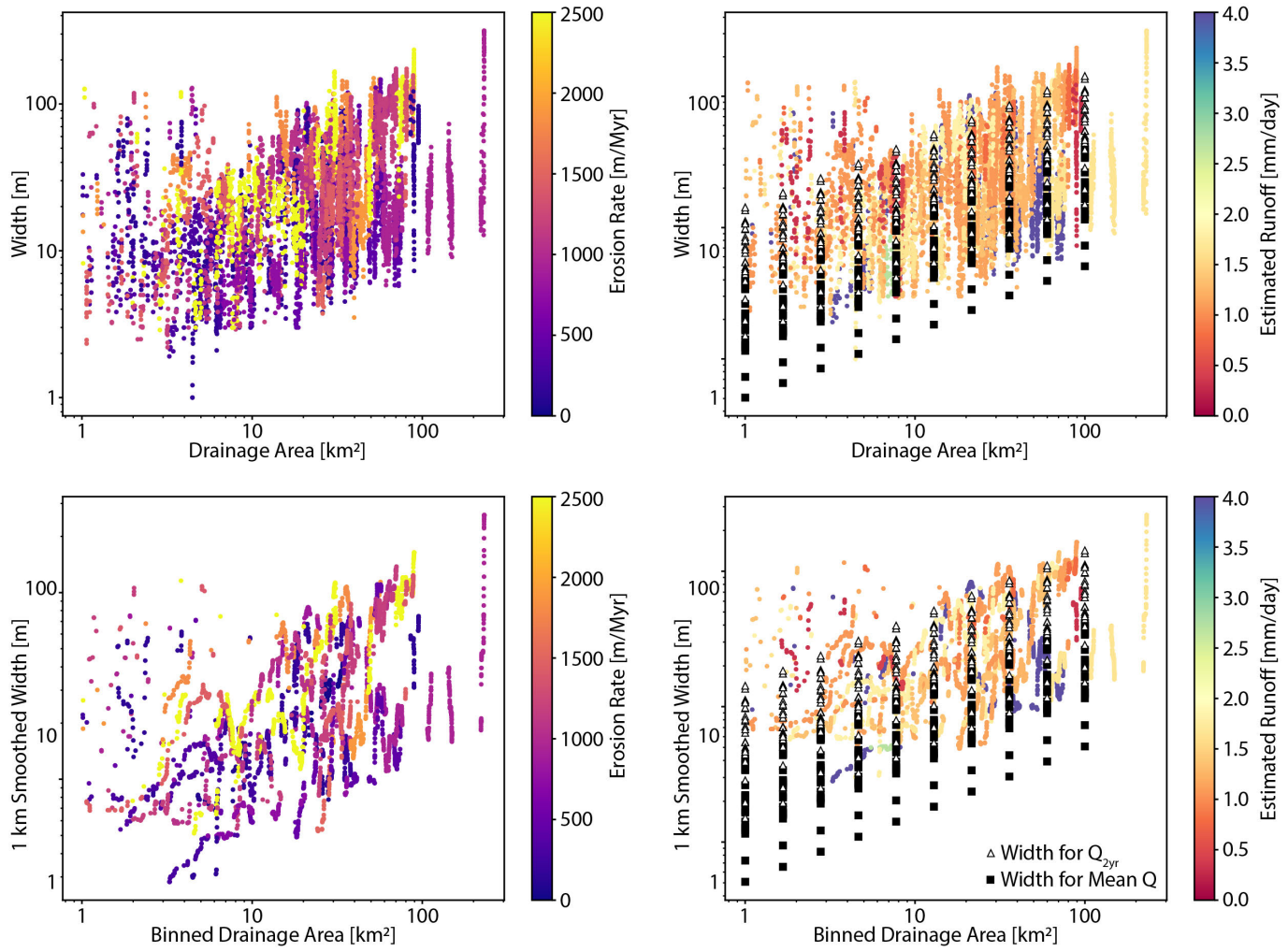


Figure S13: Comparison between widths measured on remotely sensed data and implied widths based on the choice of ω_a and k_w .

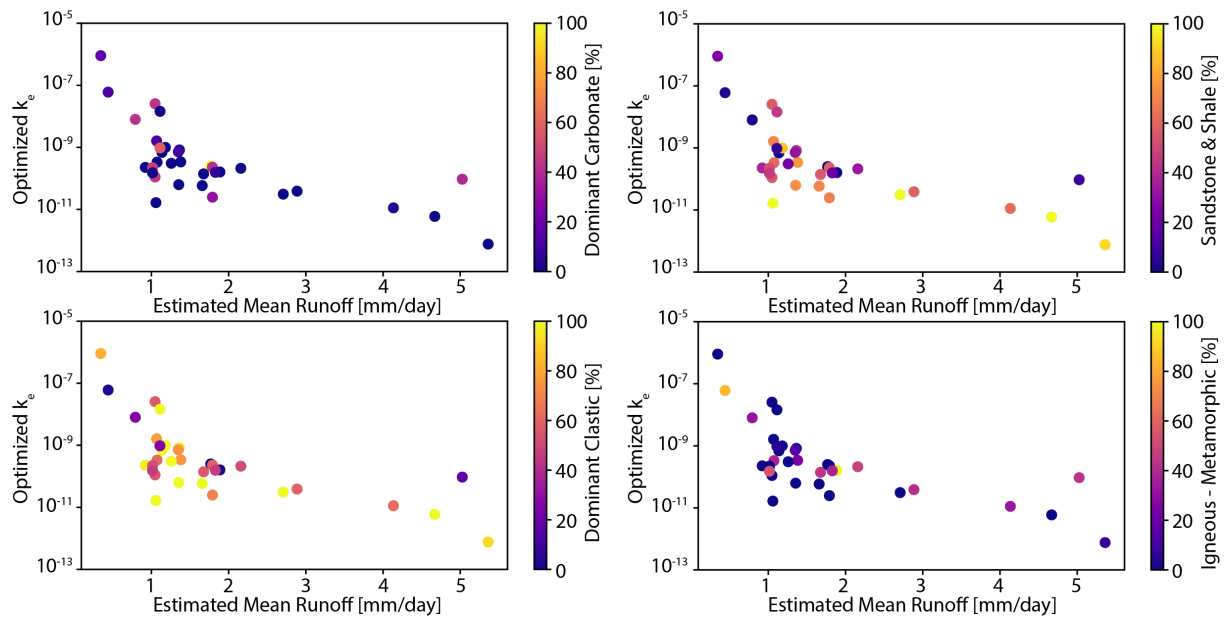


Figure S14: Variation of optimized k_e , R and lithology.

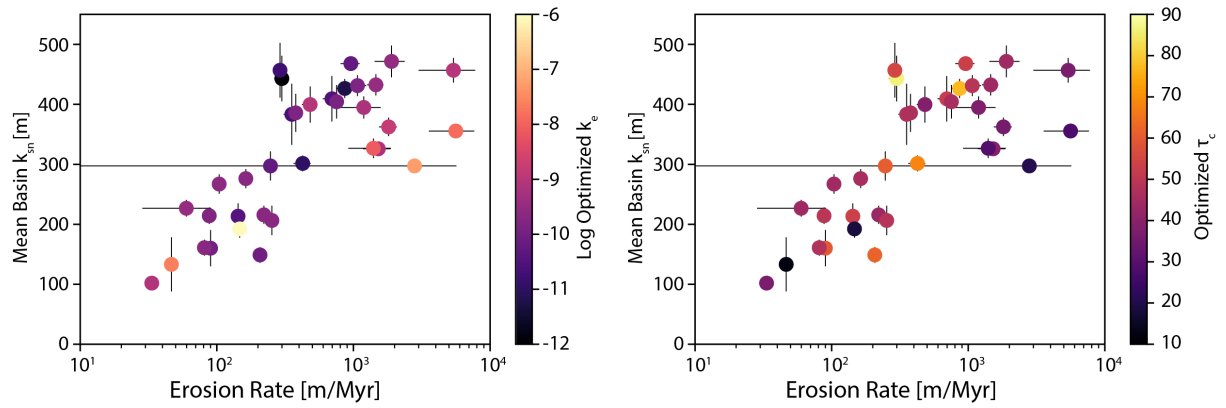


Figure S15: Relationship between k_{sn} , erosion rate, and optimized k_e and τ_c .

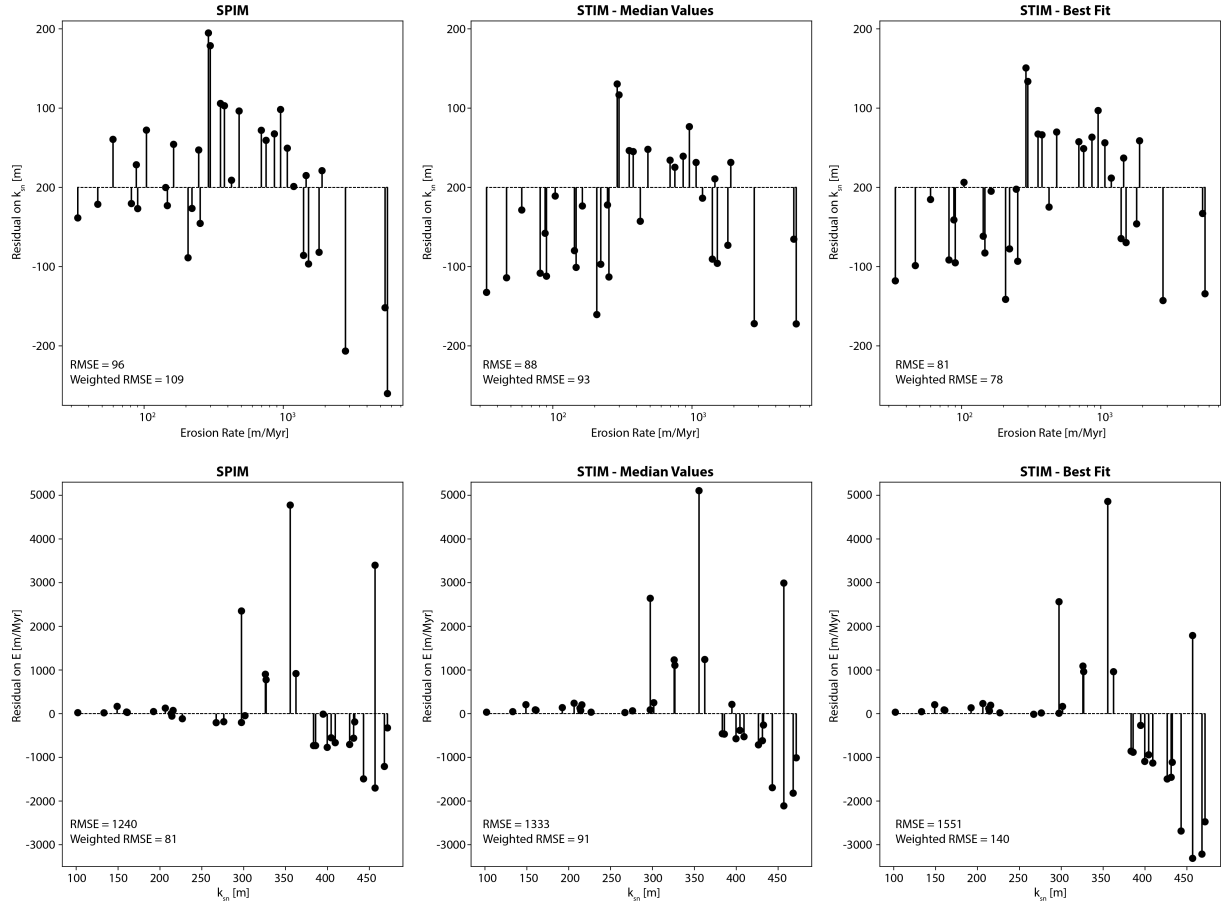


Figure S16: Comparisons of the residuals for the bootstrap SPIM fit (left column), the STIM median values relationship (center column), and the STIM ODR fit (right column). Residuals are calculated for both k_{sn} and erosion rate. Values for root mean square error (RMSE) and weighted RMSE, which considers the uncertainty on individual observations, are also shown.

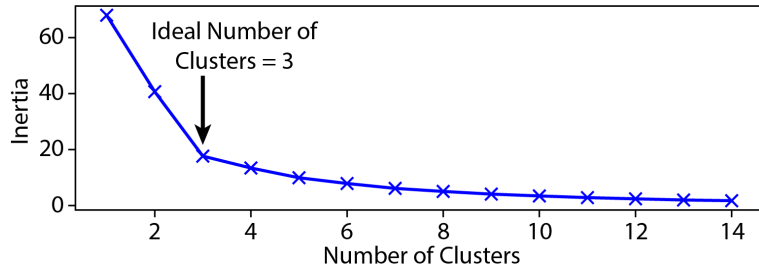


Figure S17: Elbow plot for determining ideal number of clusters in kmeans clustering of variability and runoff data.

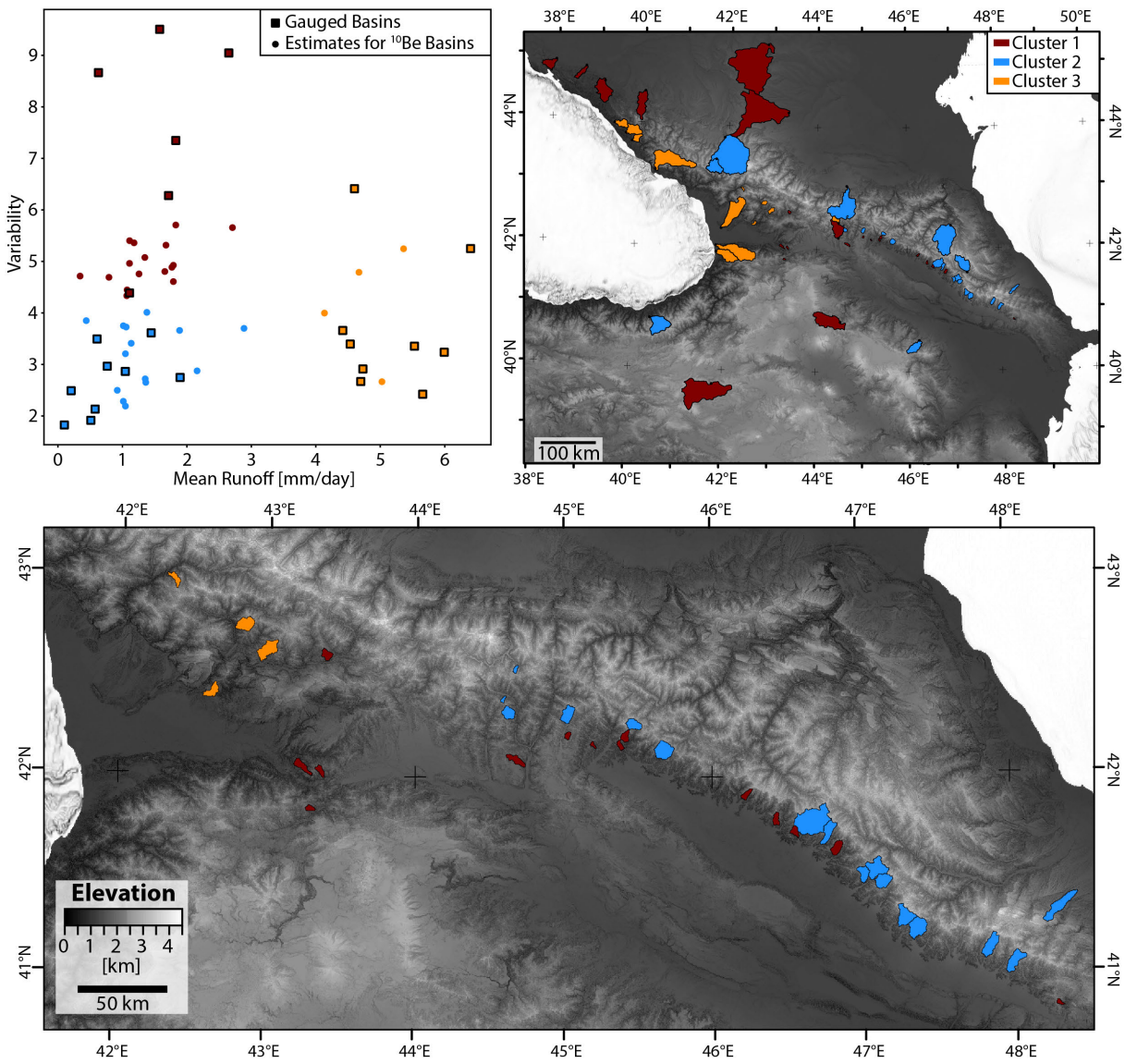


Figure S18: Upper left: Mean runoff versus variability for the GRDC gauged basins (squares) and the estimated parameters for the erosion rate basins, colored by their cluster membership. Upper right: Map of both GRDC basins and erosion rate basins colored by their cluster membership. Lower: Map of erosion rate basins colored by their cluster membership.

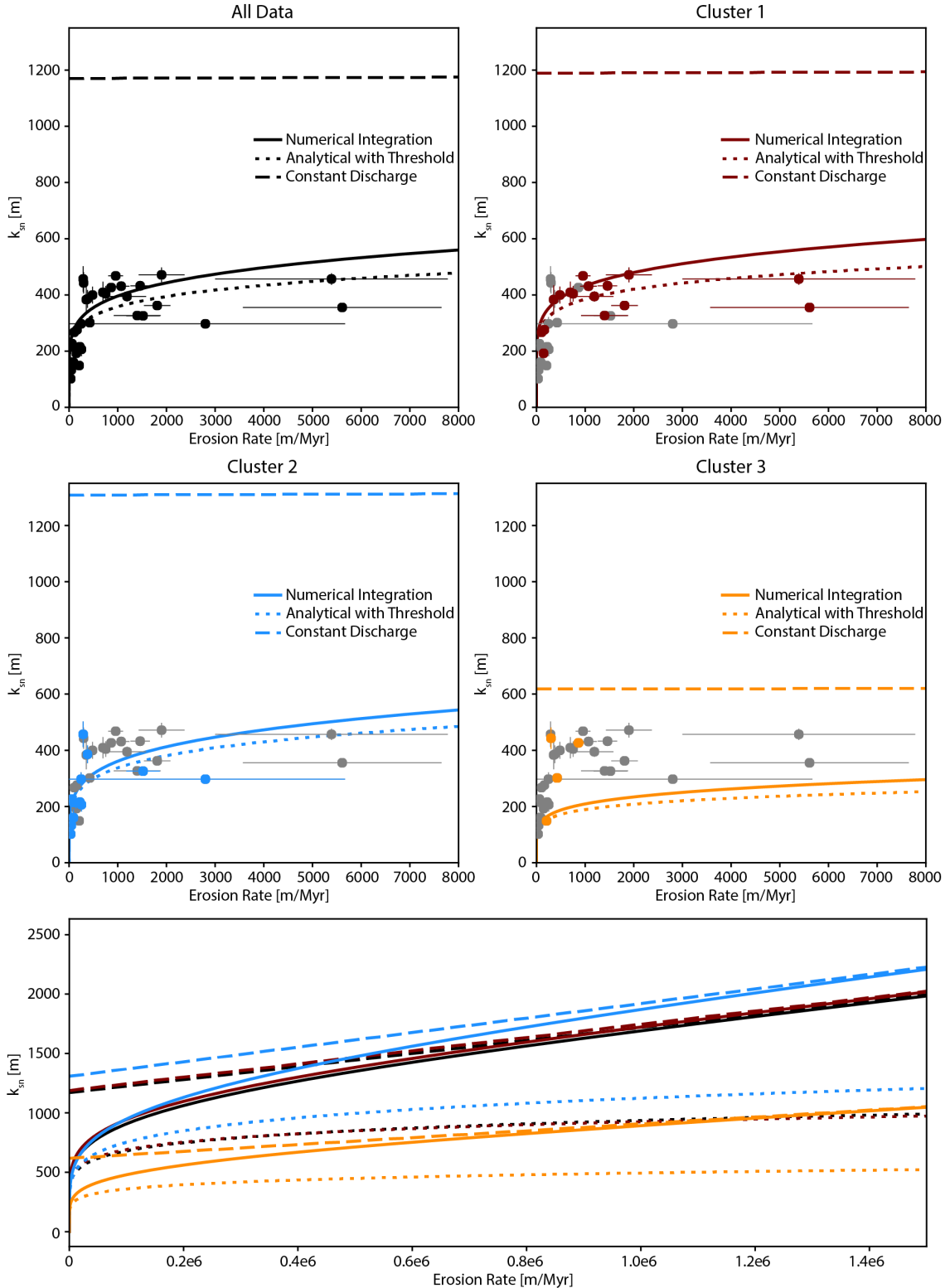


Figure S19: Relationship between k_{sn} and erosion rates and the predicted relationships based on STIM estimation using the entire dataset or specific clusters. Solid lines show the relationships as they appear in the main text, numerically solving equation S13, short dashed lines show solution using same parameters but the analytical approximation when thresholds are very large (i.e. equation S16), long dashed lines show solution using same parameters but assuming constant discharge (i.e. equation S15).

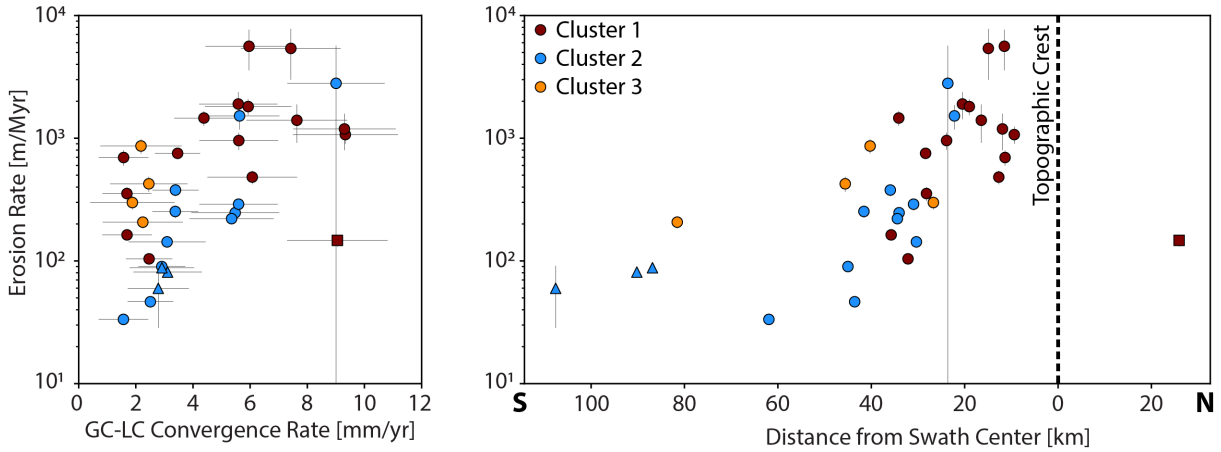


Figure S20: Erosion rate vs convergence (left) and distance from the center of the swath (right). Right panel is identical to Figure 7B in the main text, and the left panel is identical to Figure S5 except here symbols are colored by their cluster membership. This emphasizes that the erosion rates for cluster 3 are non-anomalous.

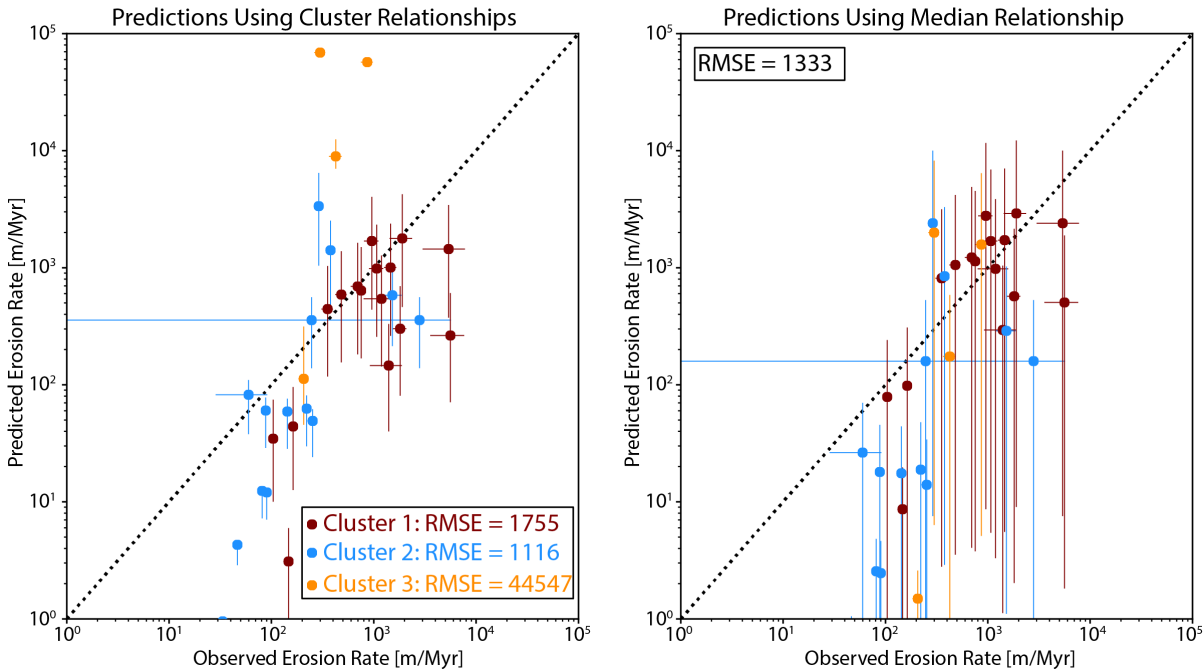


Figure S21: Left is difference between observed erosion rate (i.e. ¹⁰Be erosion rate) and predicted erosion rate for individual basins using the STIM relationship for the respective cluster to which that basin belongs. As in the main text, k_e is held fixed to the same value as the whole population. Right is the same but using the whole population STIM relationship. RMSE are calculated for the residual on erosion rate.

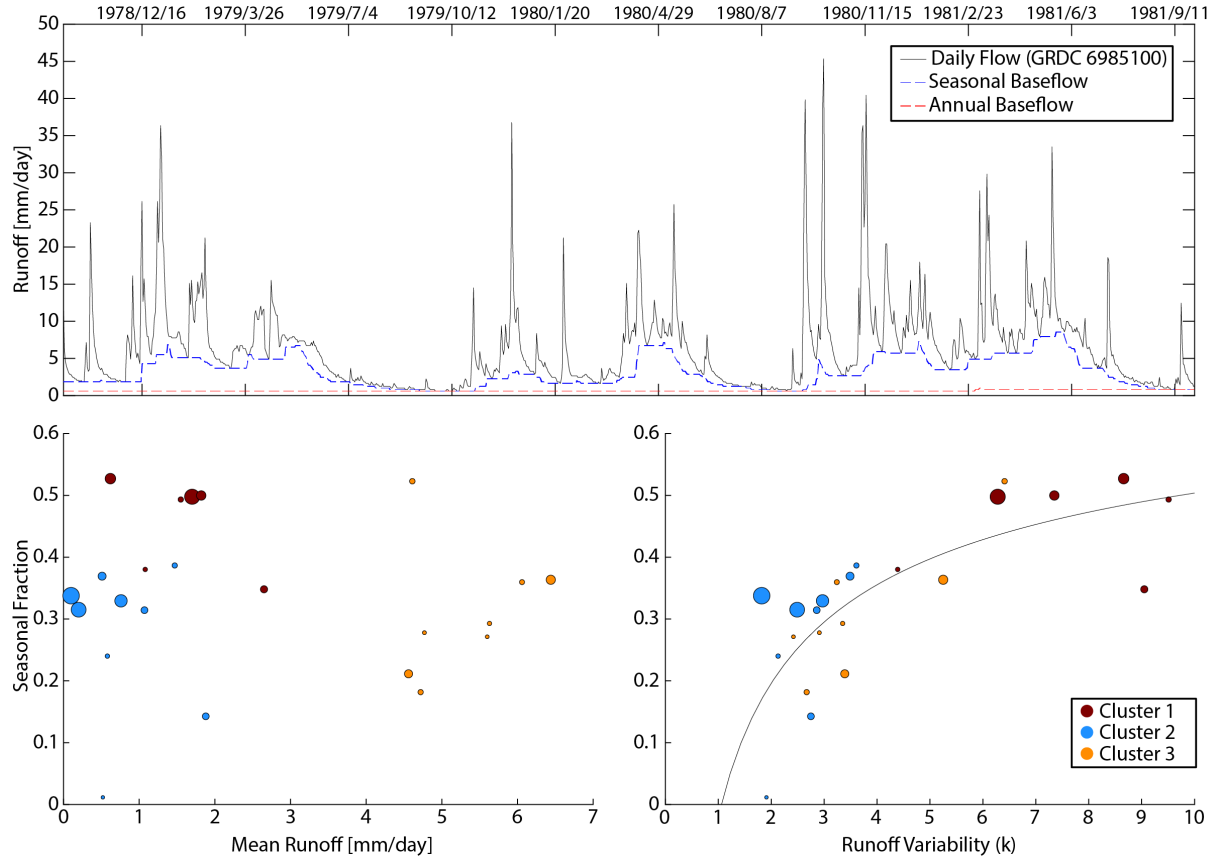


Figure S22: Upper: Example event , seasonal , and annual component separation. Bottom: Relationship between seasonal runoff fraction and (left) mean runoff and (right) runoff variability. Points on bottom plots are scaled by drainage area and color-coded by results from k-means clustering analysis from Figure 9 in main text.

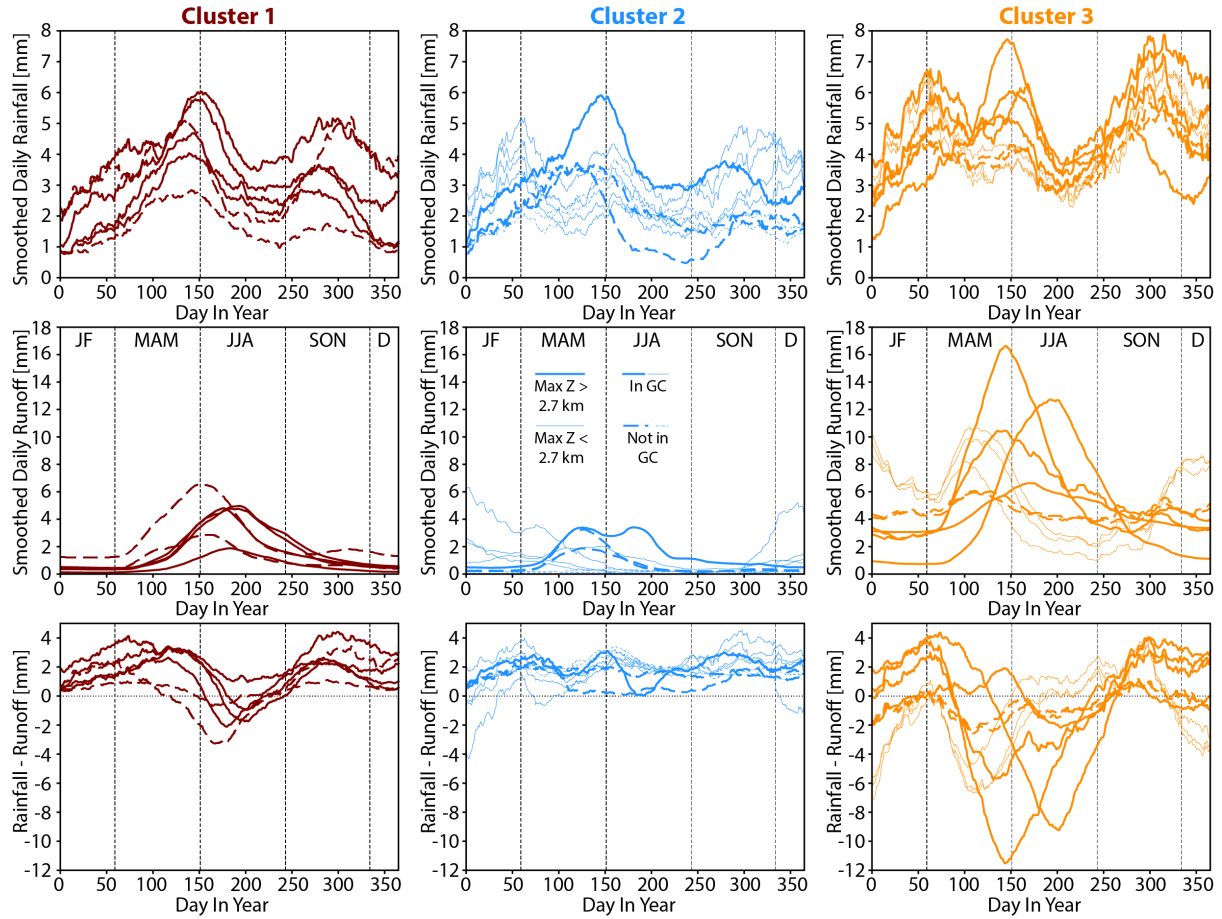


Figure S23: Upper: Averaged and smoothed rainfall time series, Middle: Averaged and smoothed runoff time series, and Bottom: Rainfall-Runoff. Watersheds are broken up by cluster from k-means clustering analysis from Figure 9 in main text. Meaningful differences in patterns were found if the data was filtered between watersheds with a maximum elevation greater or less than 2.7 km

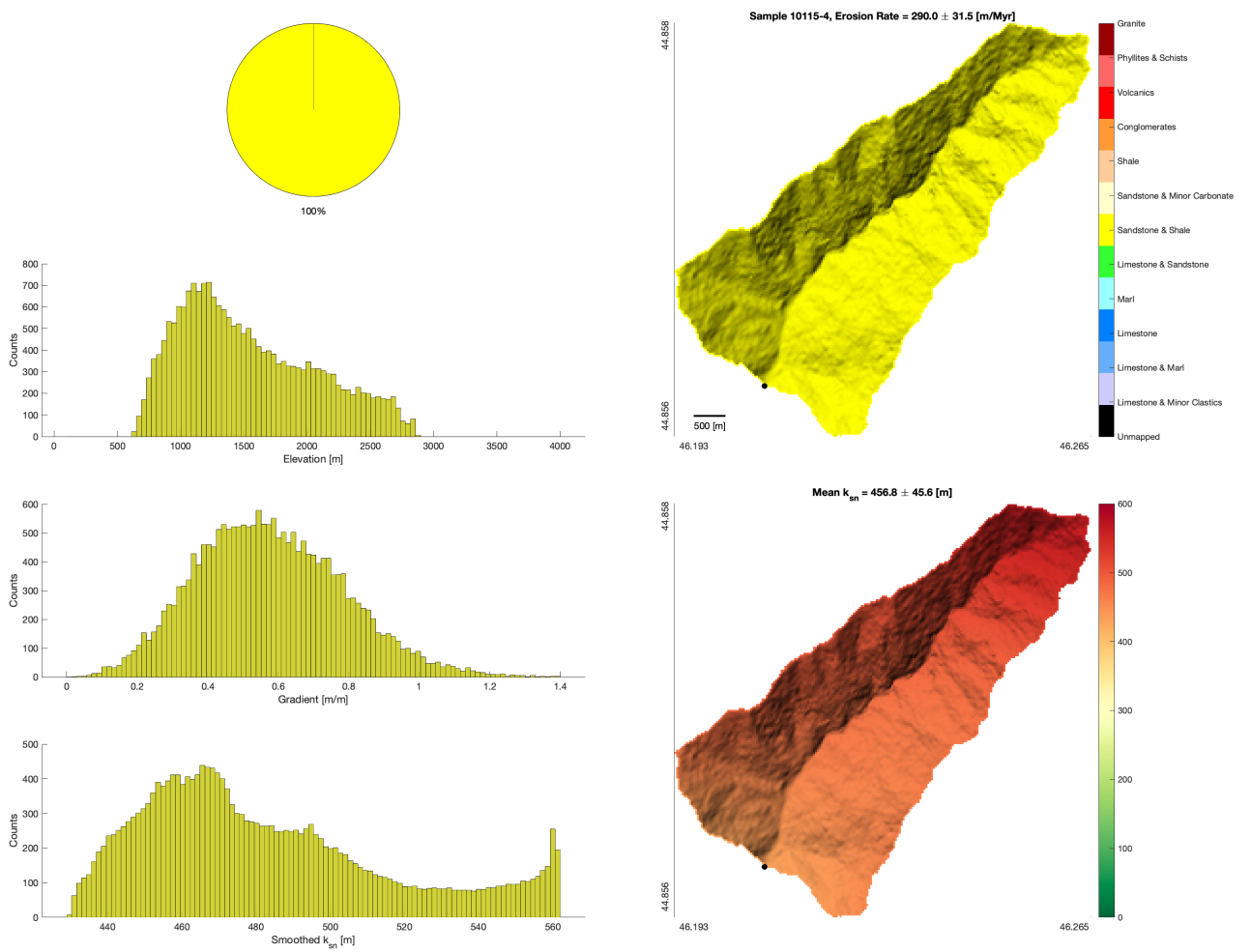


Figure S24: Relation between topography and lithology for sample 10115-4. Left column shows, from top to bottom: percentage of catchment occupied by different lithologies (keyed to color bar in right), histogram of elevation and portion of each elevation bin represented by a given lithology, histogram of hillslope gradient and portion of each gradient bin represented by a given lithology, and histogram of smoothed k_{sn} and portion of each k_{sn} bin represented by a given lithology. Right column shows distribution of lithology within the catchment (top) and smoothed k_{sn} (bottom).

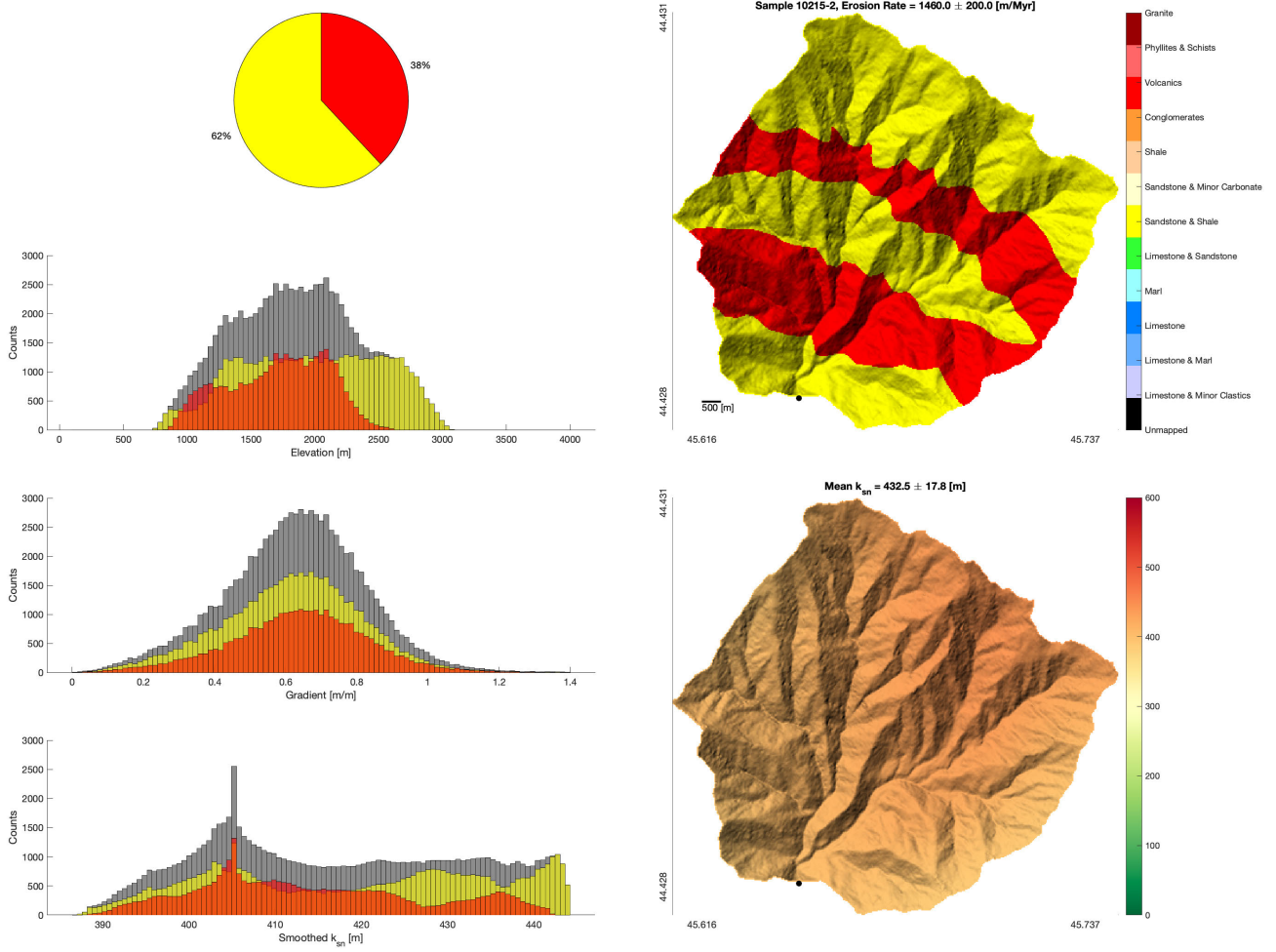


Figure S25: Relation between topography and lithology for sample 10215-2. Left column shows, from top to bottom; percentage of catchment occupied by different lithologies (keyed to color bar in right), histogram of elevation and portion of each elevation bin represented by a given lithology, histogram of hillslope gradient and portion of each gradient bin represented by a given lithology, and histogram of smoothed k_{sn} and portion of each k_{sn} bin represented by a given lithology. Right column shows distribution of lithology within the catchment (top) and smoothed k_{sn} (bottom).

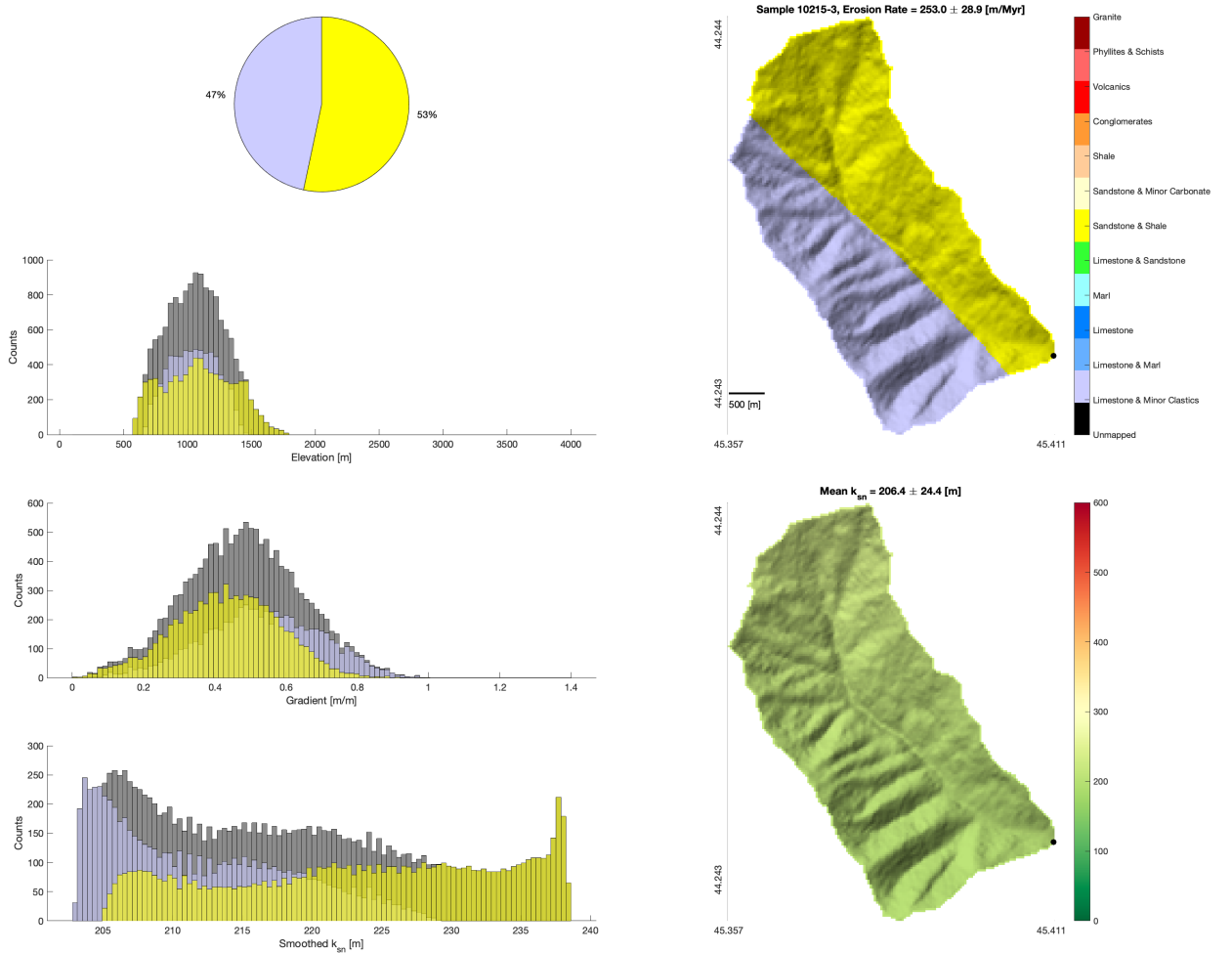


Figure S26: Relation between topography and lithology for sample 10215-3. Left column shows, from top to bottom; percentage of catchment occupied by different lithologies (keyed to color bar in right), histogram of elevation and portion of each elevation bin represented by a given lithology, histogram of hillslope gradient and portion of each gradient bin represented by a given lithology, and histogram of smoothed k_{sn} and portion of each k_{sn} bin represented by a given lithology. Right column shows distribution of lithology within the catchment (top) and smoothed k_{sn} (bottom).

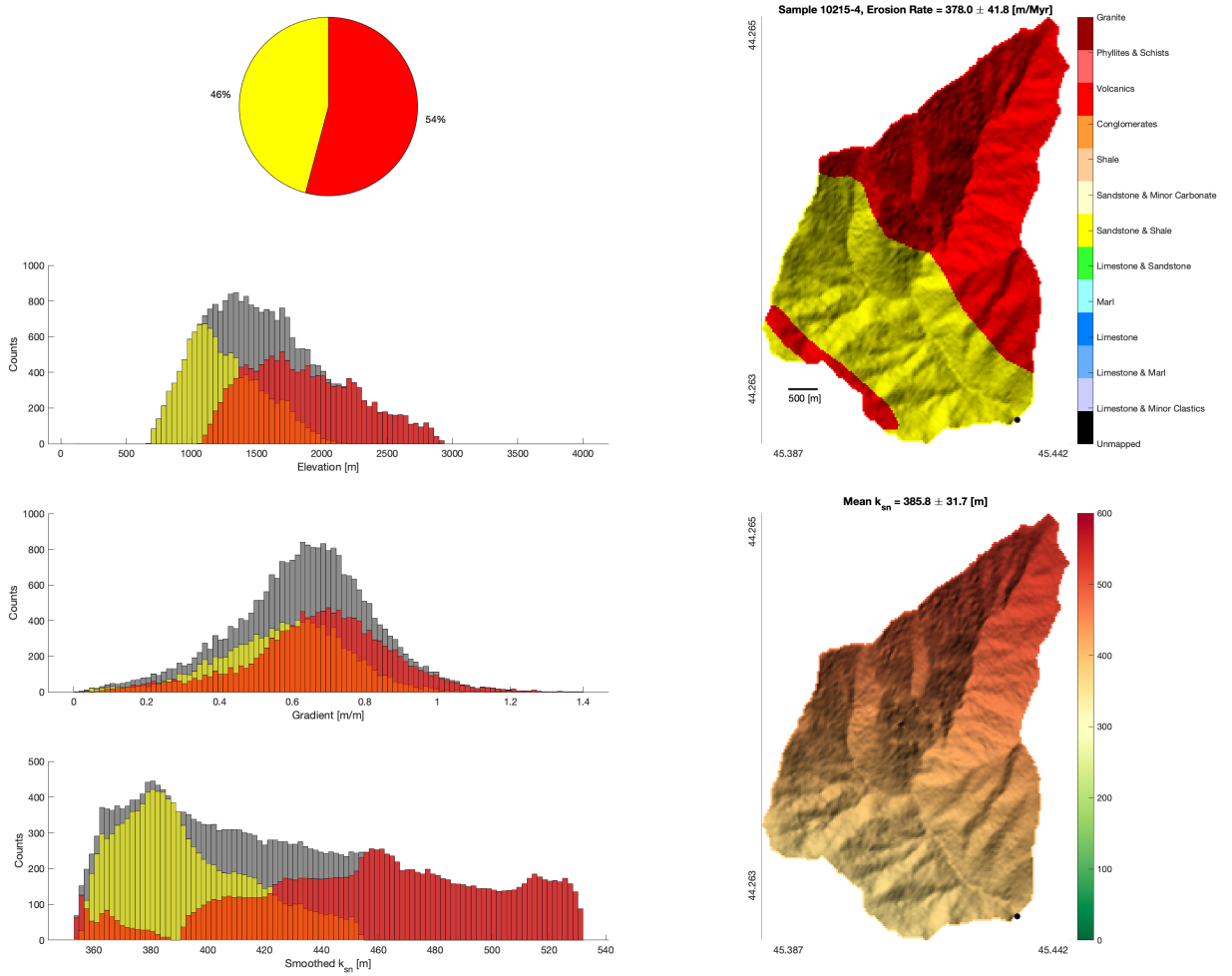


Figure S27: Relation between topography and lithology for sample 10215-4. Left column shows, from top to bottom; percentage of catchment occupied by different lithologies (keyed to color bar in right), histogram of elevation and portion of each elevation bin represented by a given lithology, histogram of hillslope gradient and portion of each gradient bin represented by a given lithology, and histogram of smoothed k_{sn} and portion of each k_{sn} bin represented by a given lithology. Right column shows distribution of lithology within the catchment (top) and smoothed k_{sn} (bottom).

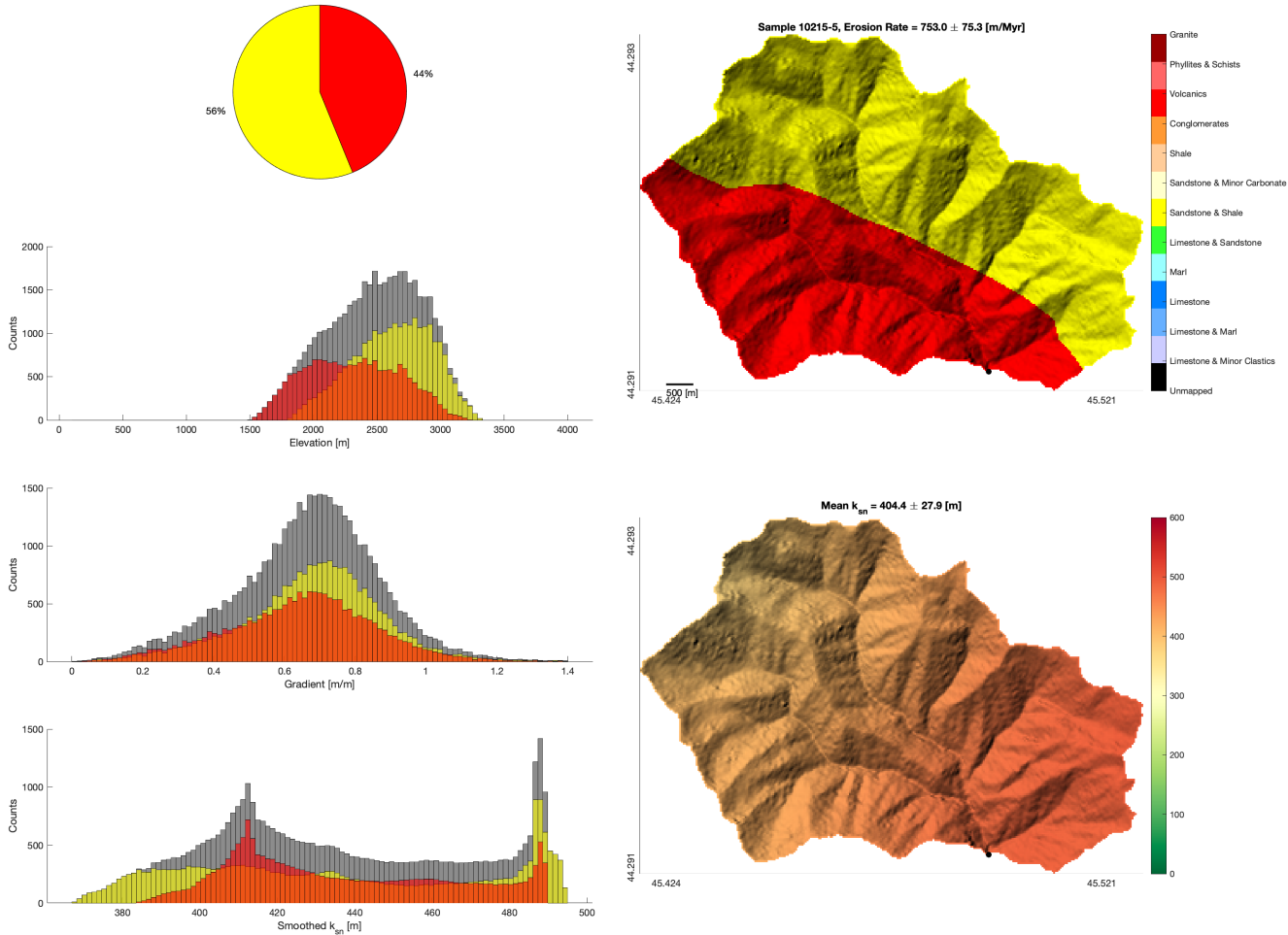


Figure S28: Relation between topography and lithology for sample 10215-5. Left column shows, from top to bottom; percentage of catchment occupied by different lithologies (keyed to color bar in right), histogram of elevation and portion of each elevation bin represented by a given lithology, histogram of hillslope gradient and portion of each gradient bin represented by a given lithology, and histogram of smoothed k_{sn} and portion of each k_{sn} bin represented by a given lithology. Right column shows distribution of lithology within the catchment (top) and smoothed k_{sn} (bottom).

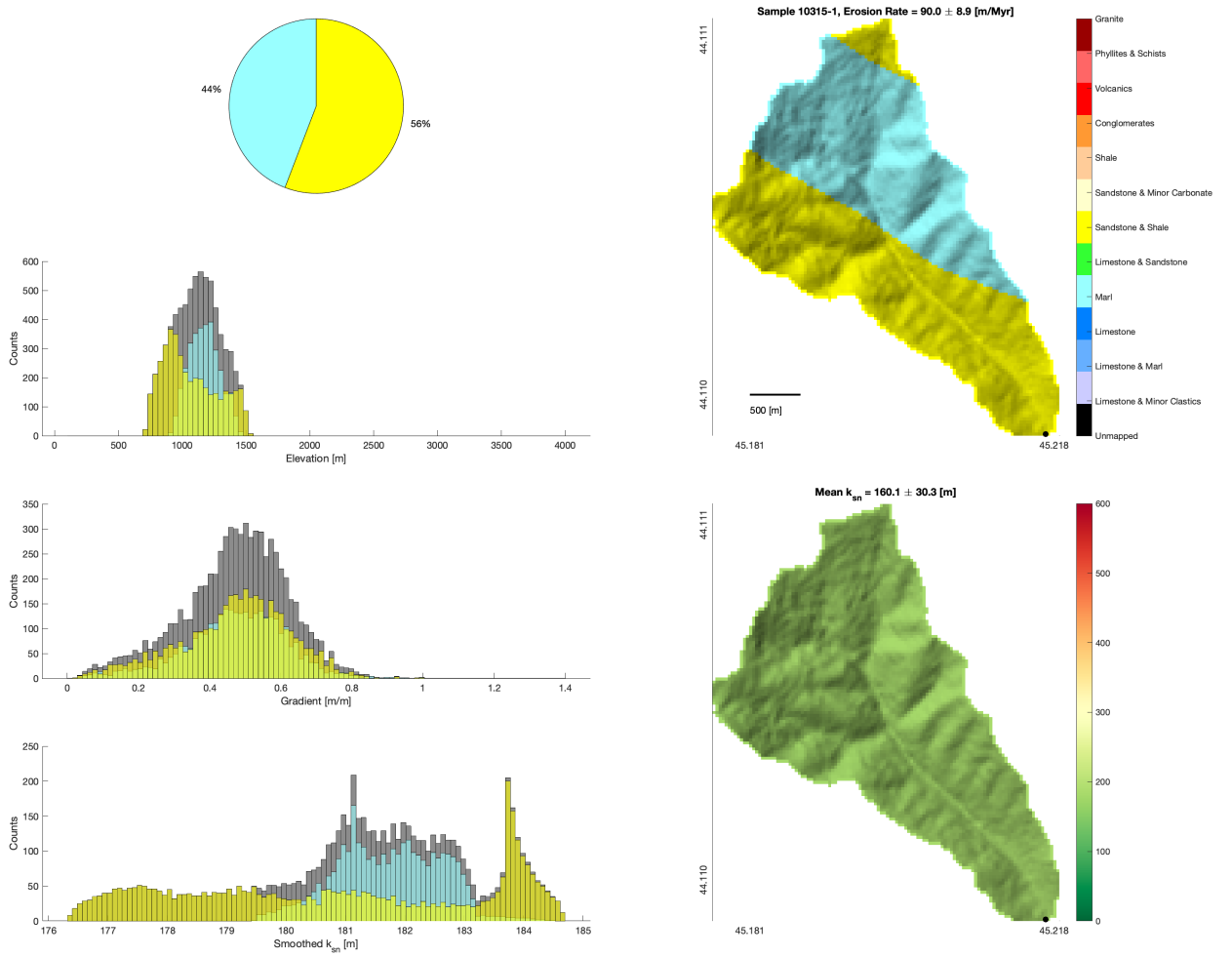


Figure S29: Relation between topography and lithology for sample 10315-1. Left column shows, from top to bottom; percentage of catchment occupied by different lithologies (keyed to color bar in right), histogram of elevation and portion of each elevation bin represented by a given lithology, histogram of hillslope gradient and portion of each gradient bin represented by a given lithology, and histogram of smoothed k_{sn} and portion of each k_{sn} bin represented by a given lithology. Right column shows distribution of lithology within the catchment (top) and smoothed k_{sn} (bottom).

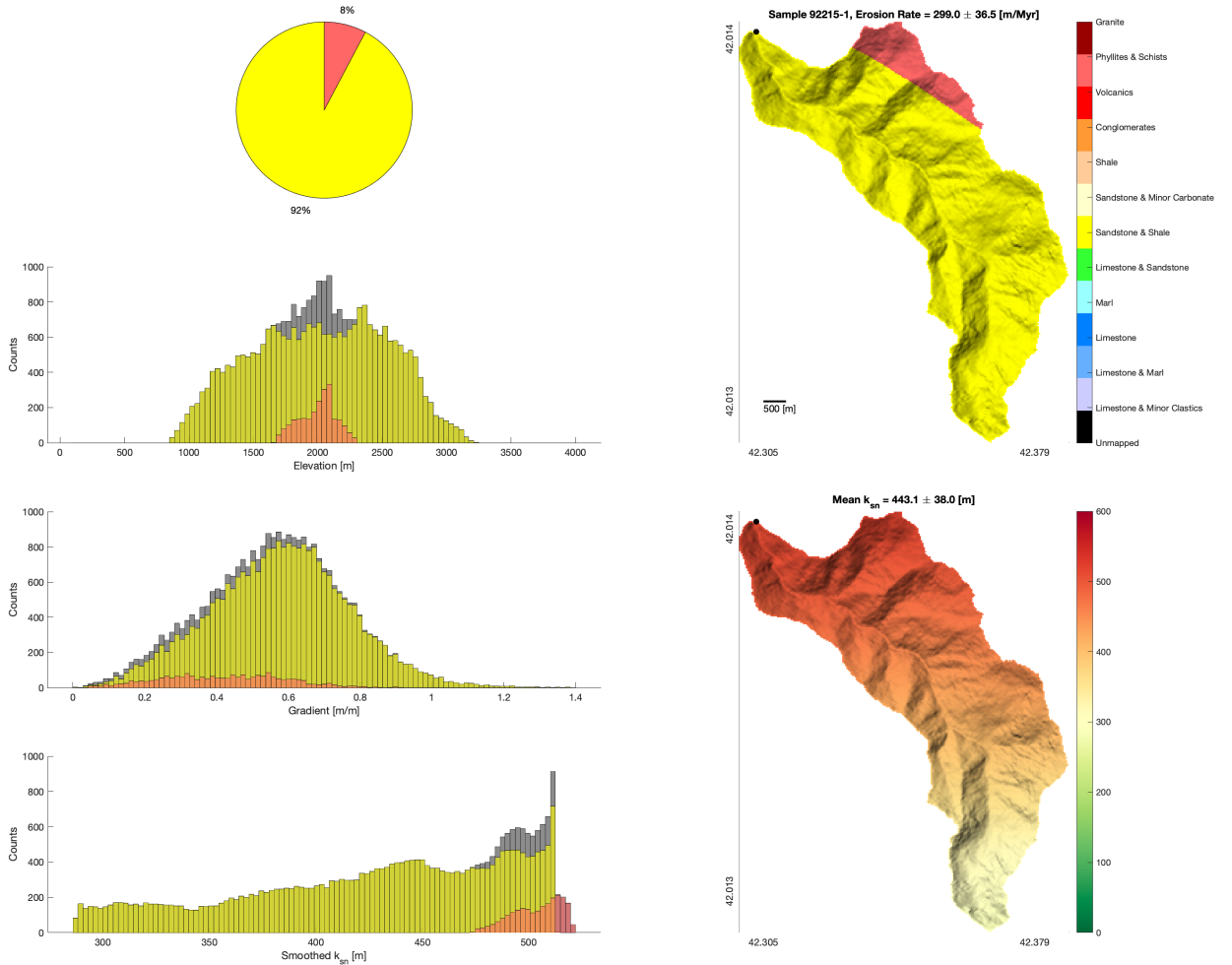


Figure S30: Relation between topography and lithology for sample 92215-1. Left column shows, from top to bottom; percentage of catchment occupied by different lithologies (keyed to color bar in right), histogram of elevation and portion of each elevation bin represented by a given lithology, histogram of hillslope gradient and portion of each gradient bin represented by a given lithology, and histogram of smoothed k_{sn} and portion of each k_{sn} bin represented by a given lithology. Right column shows distribution of lithology within the catchment (top) and smoothed k_{sn} (bottom).

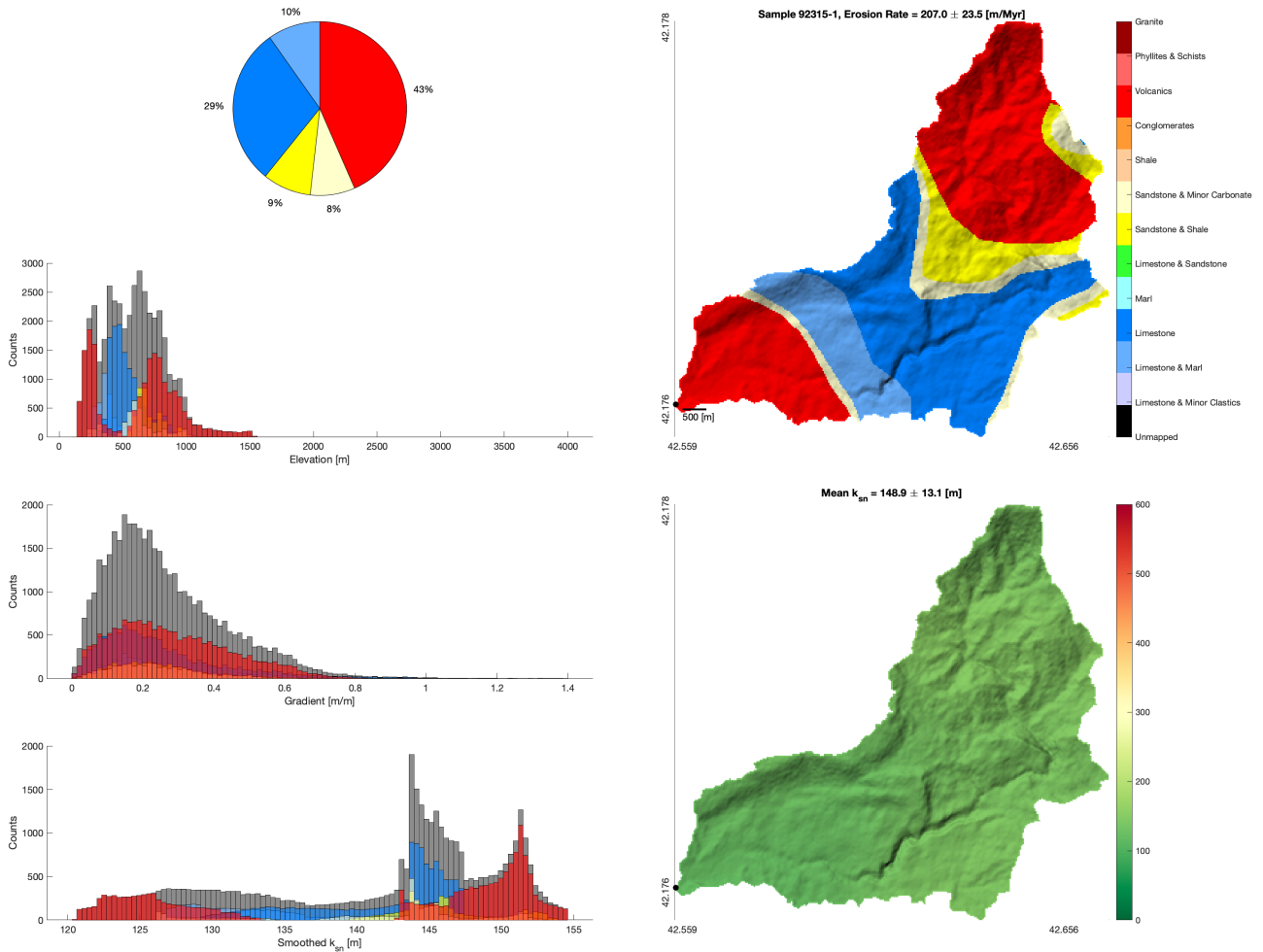


Figure S31: Relation between topography and lithology for sample 92315-1. Left column shows, from top to bottom; percentage of catchment occupied by different lithologies (keyed to color bar in right), histogram of elevation and portion of each elevation bin represented by a given lithology, histogram of hillslope gradient and portion of each gradient bin represented by a given lithology, and histogram of smoothed k_{sn} and portion of each k_{sn} bin represented by a given lithology. Right column shows distribution of lithology within the catchment (top) and smoothed k_{sn} (bottom).

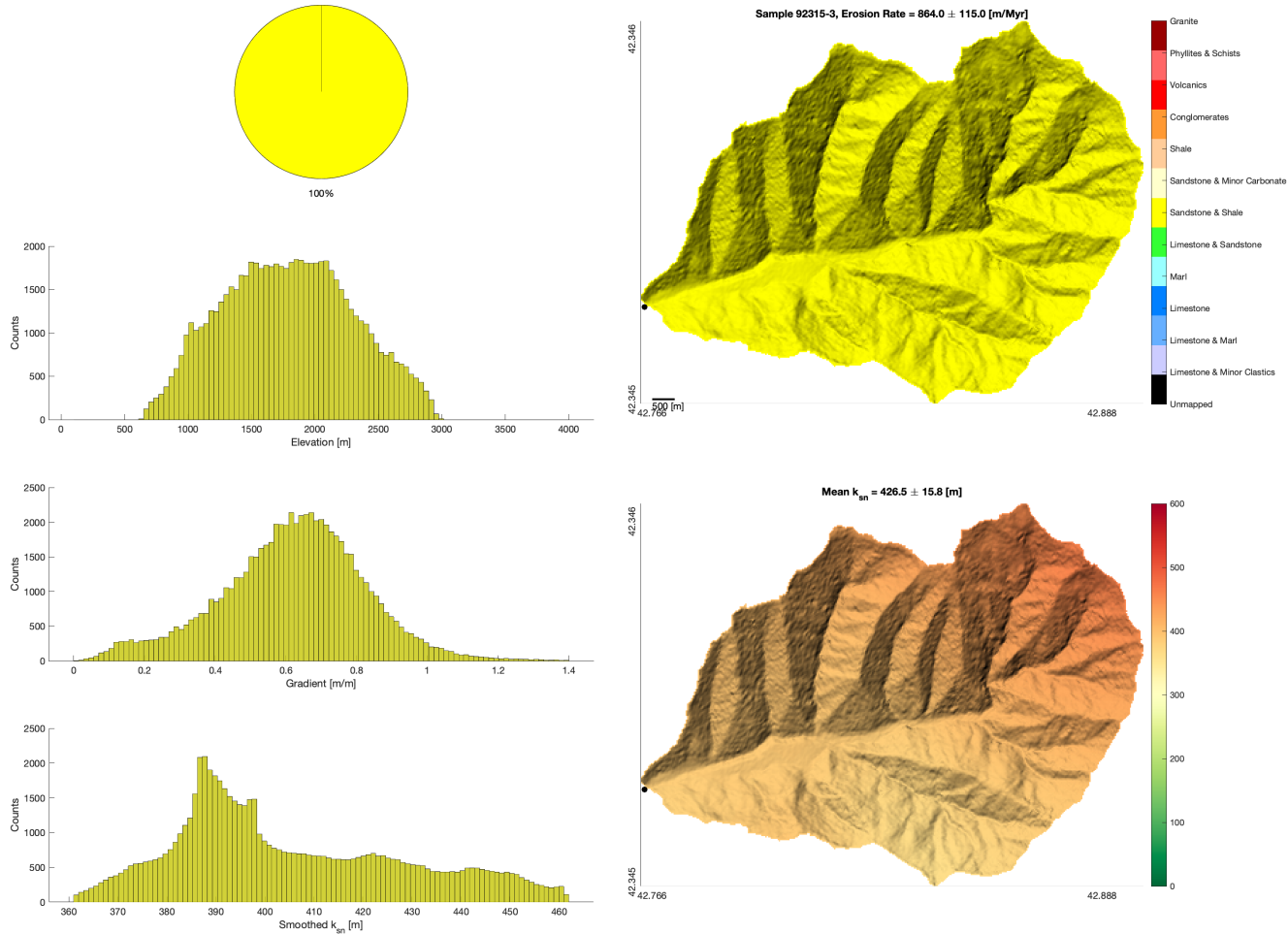


Figure S32: Relation between topography and lithology for sample 92315-3. Left column shows, from top to bottom; percentage of catchment occupied by different lithologies (keyed to color bar in right), histogram of elevation and portion of each elevation bin represented by a given lithology, histogram of hillslope gradient and portion of each gradient bin represented by a given lithology, and histogram of smoothed k_{sn} and portion of each k_{sn} bin represented by a given lithology. Right column shows distribution of lithology within the catchment (top) and smoothed k_{sn} (bottom).

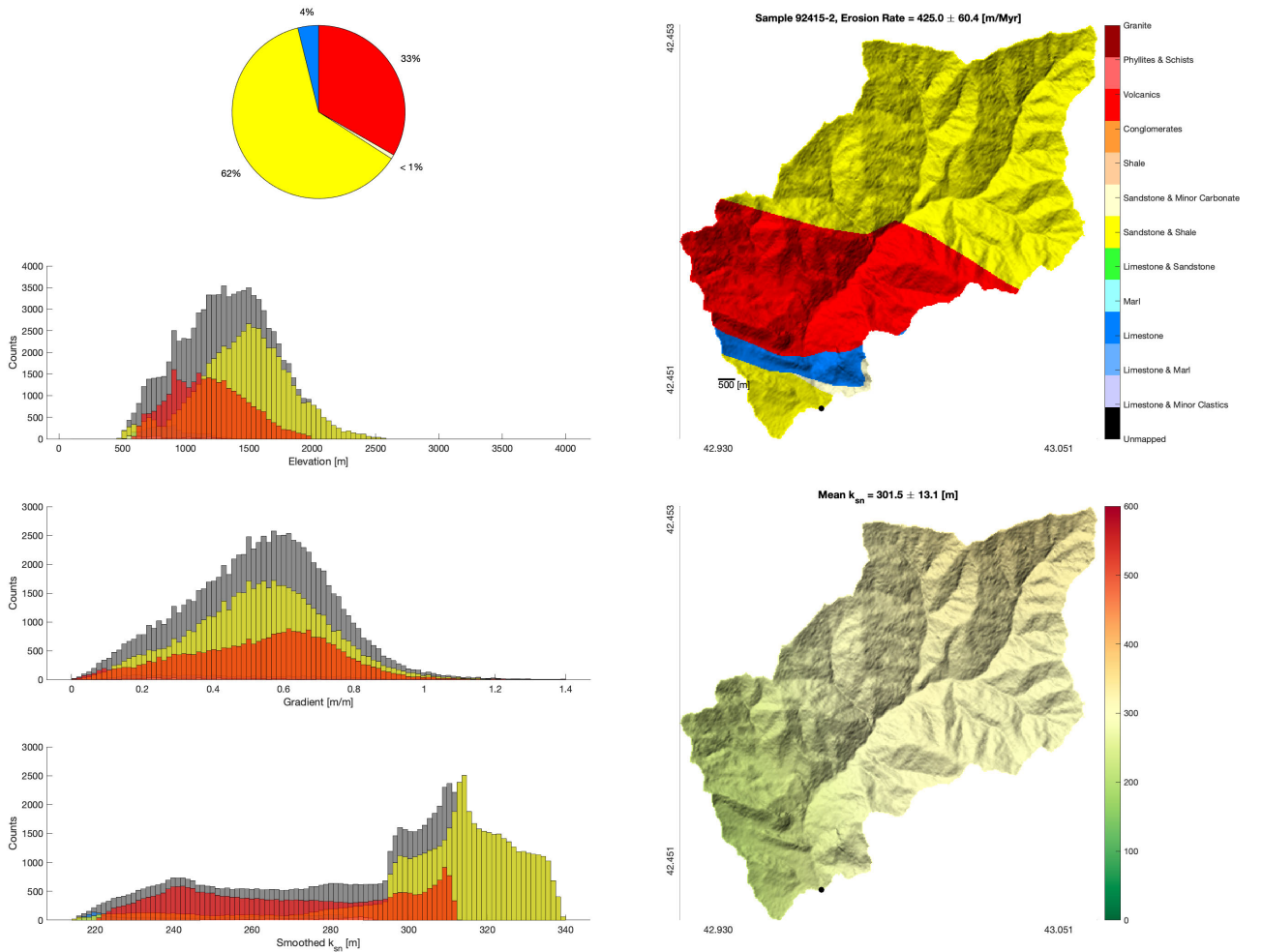


Figure S33: Relation between topography and lithology for sample 92415-2. Left column shows, from top to bottom; percentage of catchment occupied by different lithologies (keyed to color bar in right), histogram of elevation and portion of each elevation bin represented by a given lithology, histogram of hillslope gradient and portion of each gradient bin represented by a given lithology, and histogram of smoothed k_{sn} and portion of each k_{sn} bin represented by a given lithology. Right column shows distribution of lithology within the catchment (top) and smoothed k_{sn} (bottom).

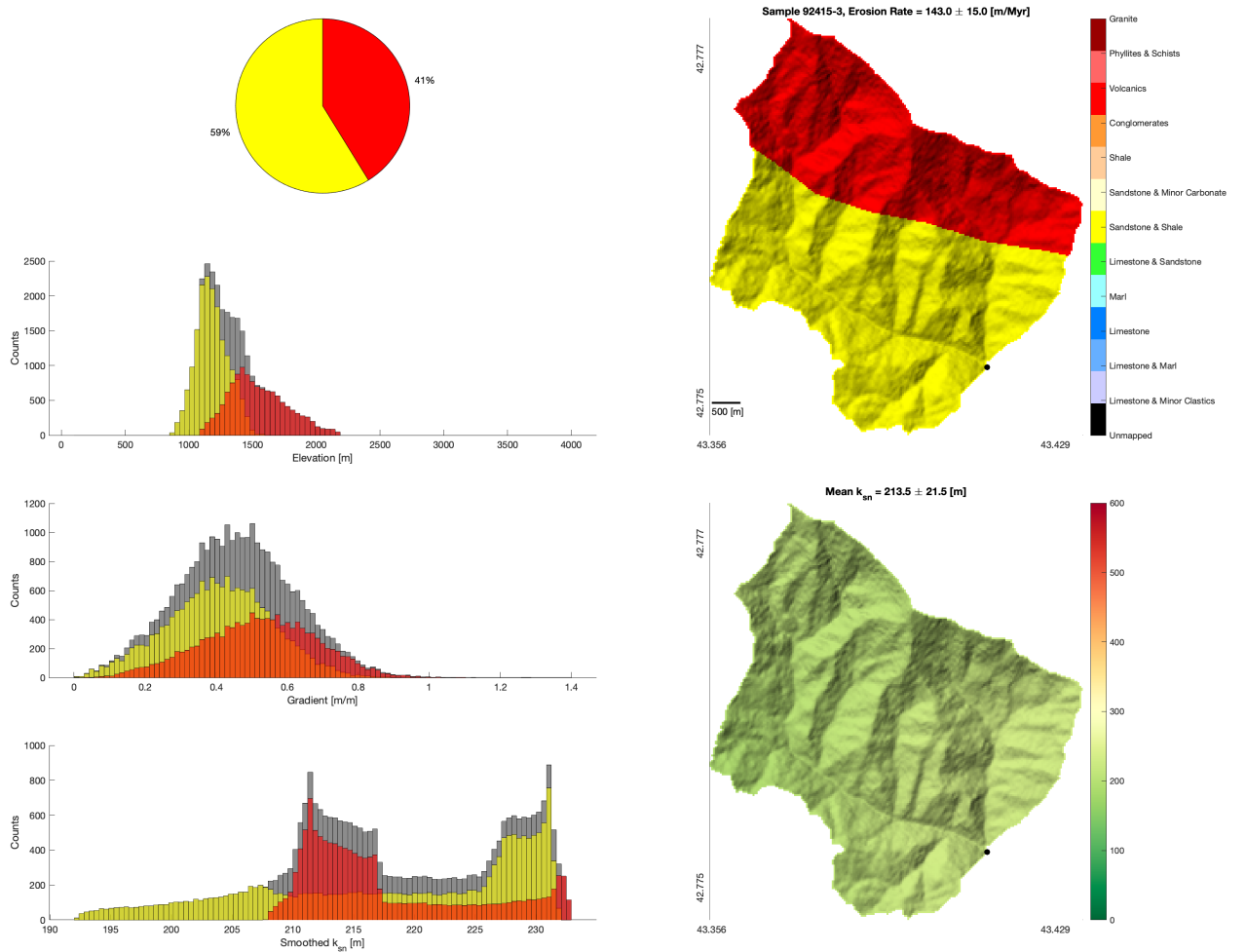


Figure S34: Relation between topography and lithology for sample 92415-3. Left column shows, from top to bottom; percentage of catchment occupied by different lithologies (keyed to color bar in right), histogram of elevation and portion of each elevation bin represented by a given lithology, histogram of hillslope gradient and portion of each gradient bin represented by a given lithology, and histogram of smoothed k_{sn} and portion of each k_{sn} bin represented by a given lithology. Right column shows distribution of lithology within the catchment (top) and smoothed k_{sn} (bottom).

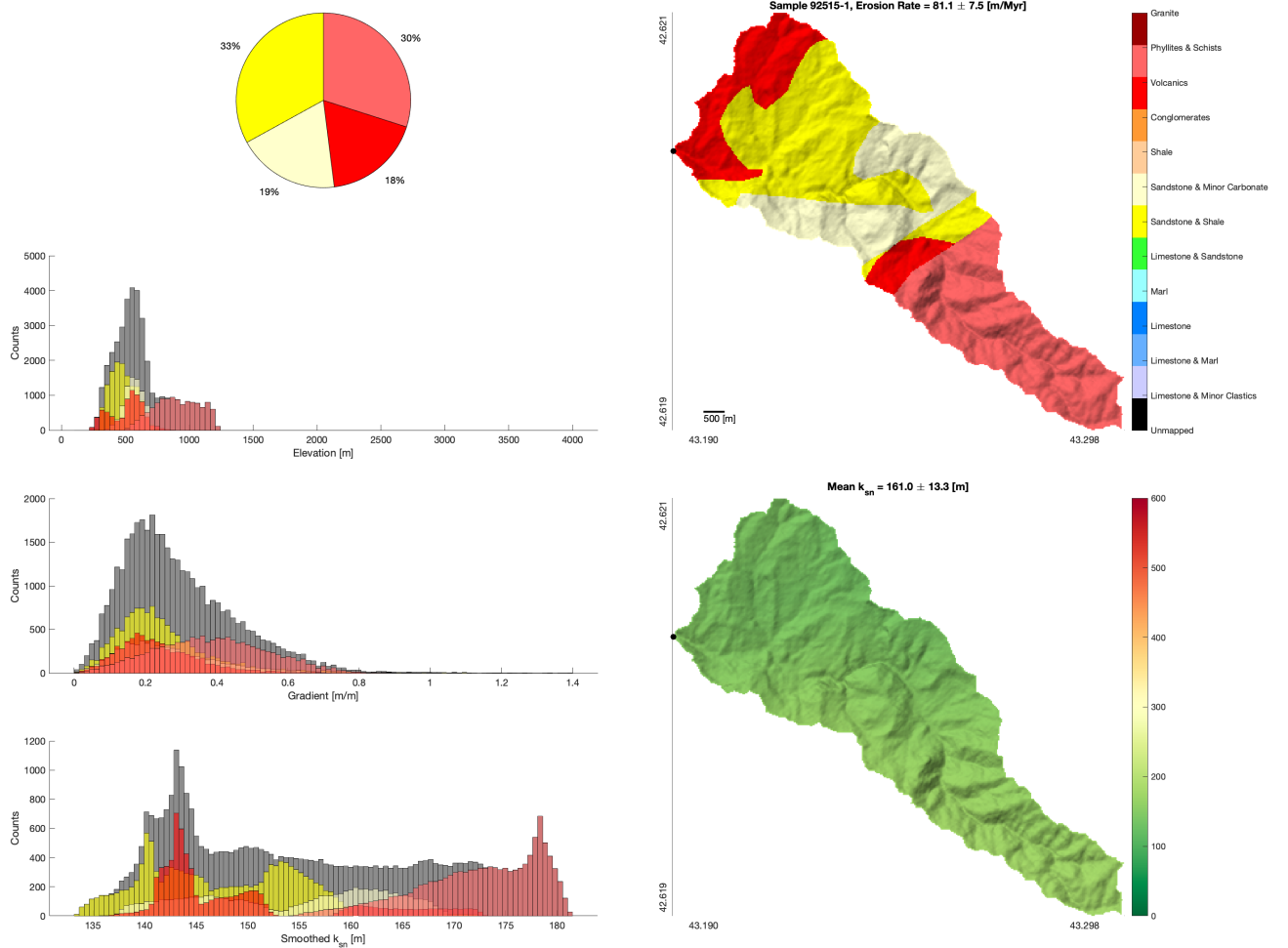


Figure S35: Relation between topography and lithology for sample 92515-1. Left column shows, from top to bottom; percentage of catchment occupied by different lithologies (keyed to color bar in right), histogram of elevation and portion of each elevation bin represented by a given lithology, histogram of hillslope gradient and portion of each gradient bin represented by a given lithology, and histogram of smoothed k_{sn} and portion of each k_{sn} bin represented by a given lithology. Right column shows distribution of lithology within the catchment (top) and smoothed k_{sn} (bottom).

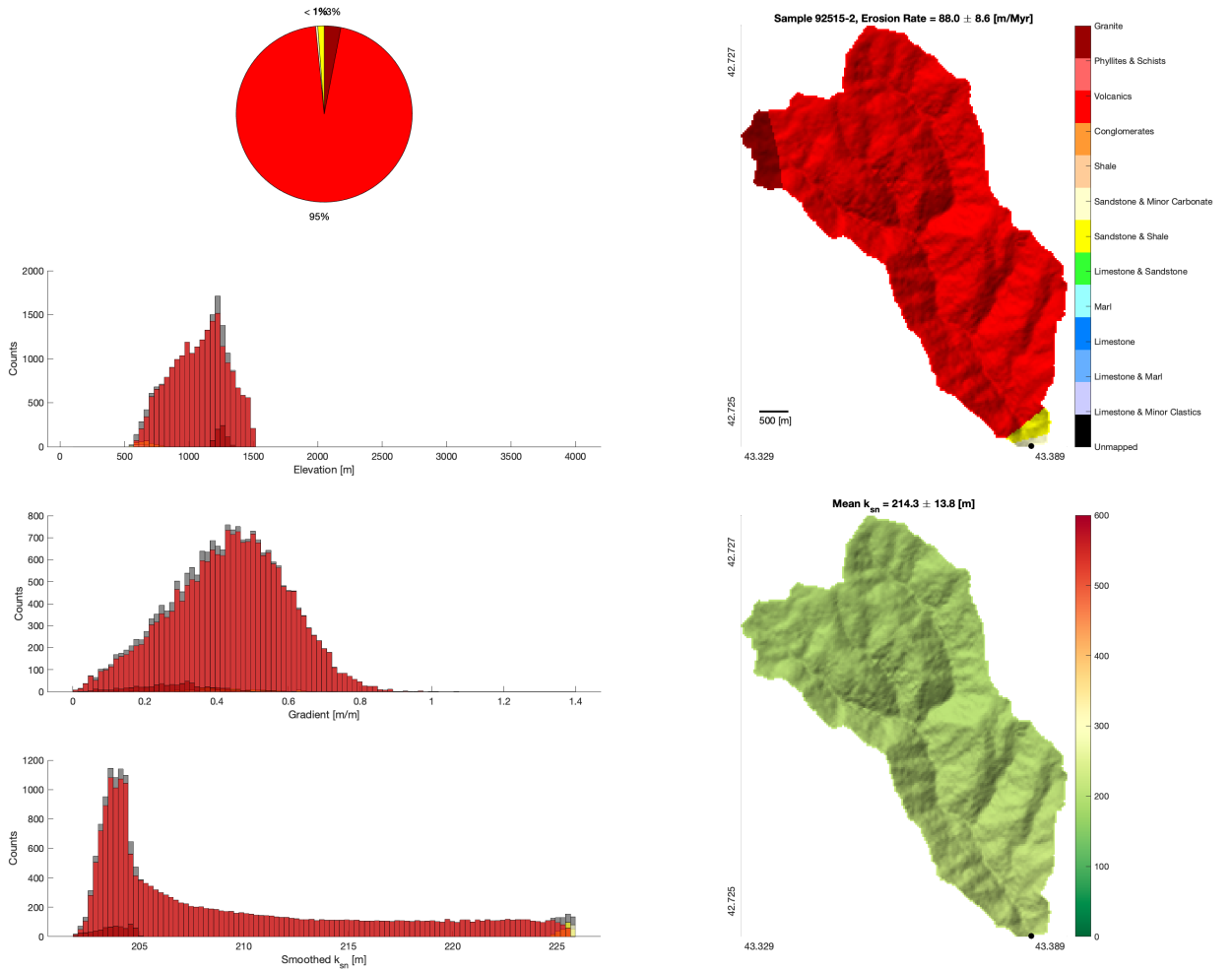


Figure S36: Relation between topography and lithology for sample 92515-2. Left column shows, from top to bottom; percentage of catchment occupied by different lithologies (keyed to color bar in right), histogram of elevation and portion of each elevation bin represented by a given lithology, histogram of hillslope gradient and portion of each gradient bin represented by a given lithology, and histogram of smoothed k_{sn} and portion of each k_{sn} bin represented by a given lithology. Right column shows distribution of lithology within the catchment (top) and smoothed k_{sn} (bottom).

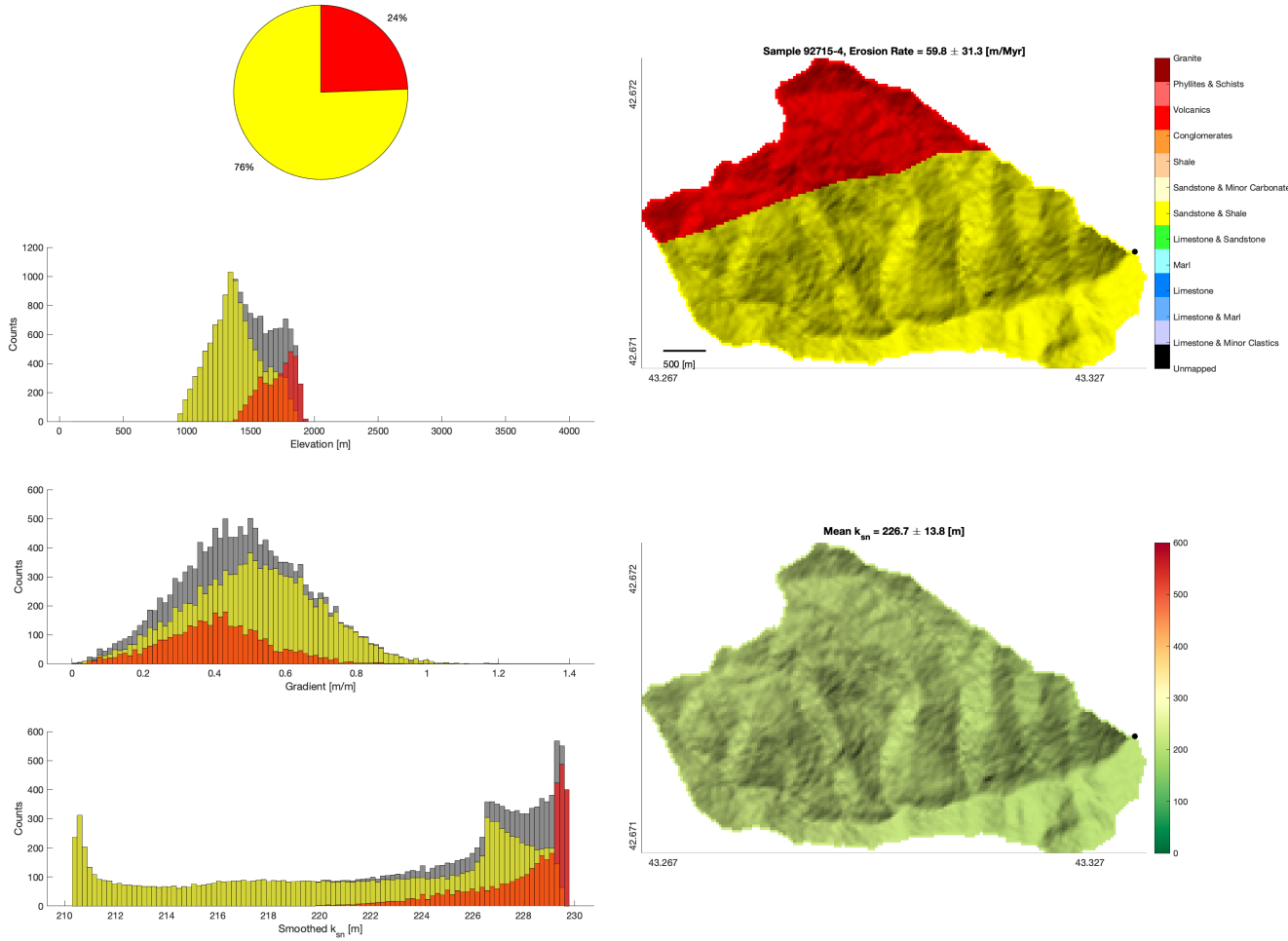


Figure S37: Relation between topography and lithology for sample 92715-4. Left column shows, from top to bottom; percentage of catchment occupied by different lithologies (keyed to color bar in right), histogram of elevation and portion of each elevation bin represented by a given lithology, histogram of hillslope gradient and portion of each gradient bin represented by a given lithology, and histogram of smoothed k_{sn} and portion of each k_{sn} bin represented by a given lithology. Right column shows distribution of lithology within the catchment (top) and smoothed k_{sn} (bottom).

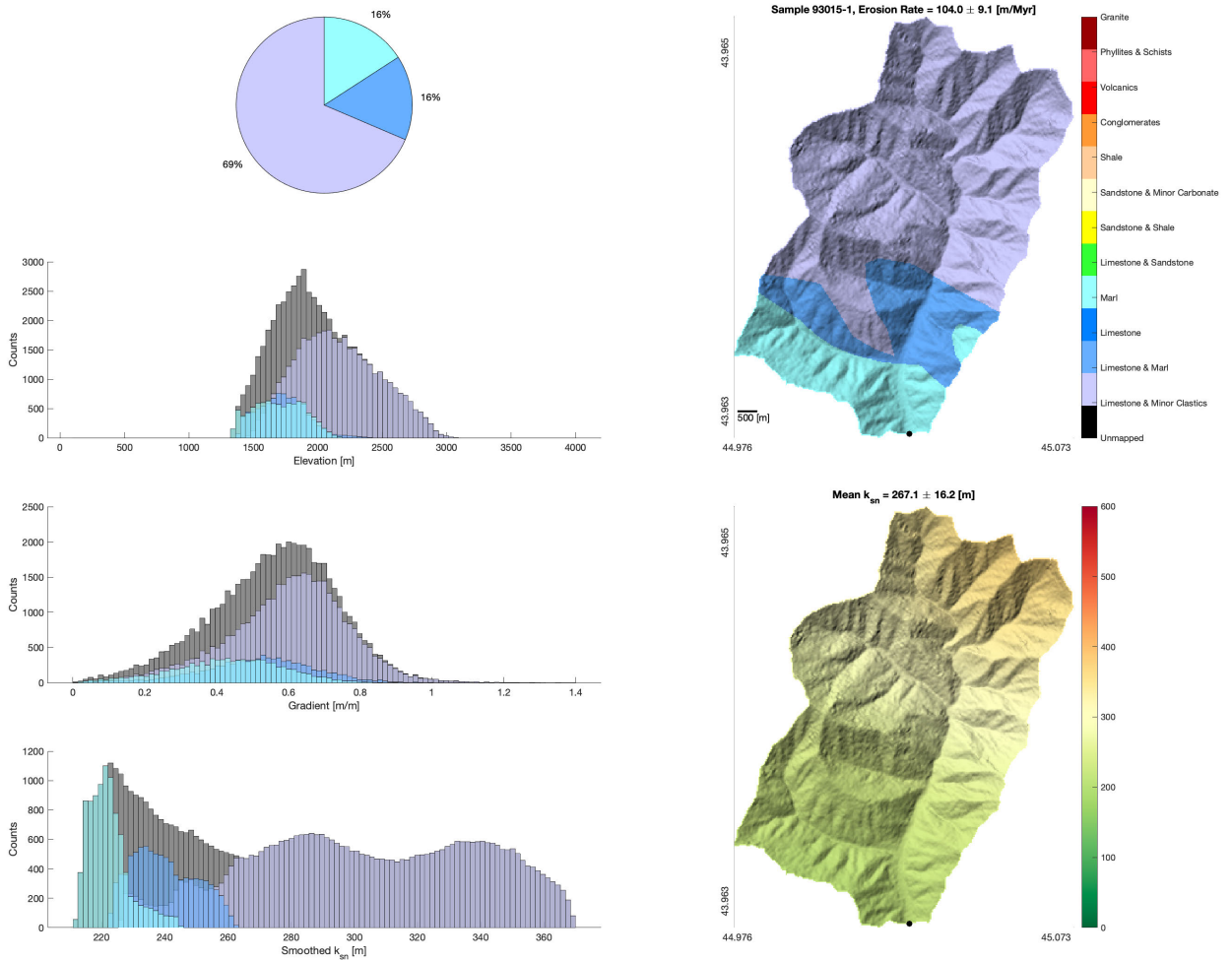


Figure S38: Relation between topography and lithology for sample 93015-1. Left column shows, from top to bottom; percentage of catchment occupied by different lithologies (keyed to color bar in right), histogram of elevation and portion of each elevation bin represented by a given lithology, histogram of hillslope gradient and portion of each gradient bin represented by a given lithology, and histogram of smoothed k_{sn} and portion of each k_{sn} bin represented by a given lithology. Right column shows distribution of lithology within the catchment (top) and smoothed k_{sn} (bottom).

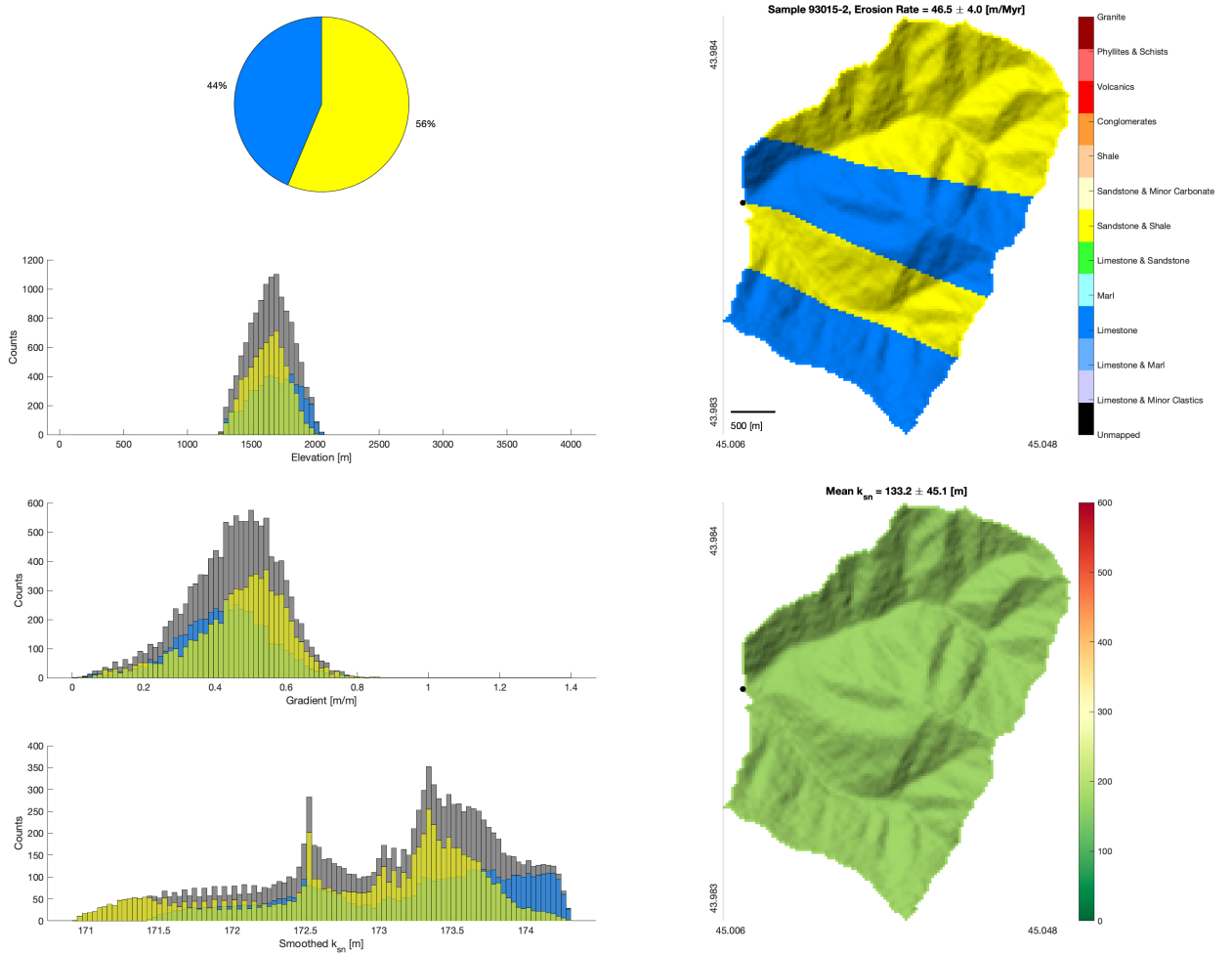


Figure S39: Relation between topography and lithology for sample 93015-2. Left column shows, from top to bottom; percentage of catchment occupied by different lithologies (keyed to color bar in right), histogram of elevation and portion of each elevation bin represented by a given lithology, histogram of hillslope gradient and portion of each gradient bin represented by a given lithology, and histogram of smoothed k_{sn} and portion of each k_{sn} bin represented by a given lithology. Right column shows distribution of lithology within the catchment (top) and smoothed k_{sn} (bottom).

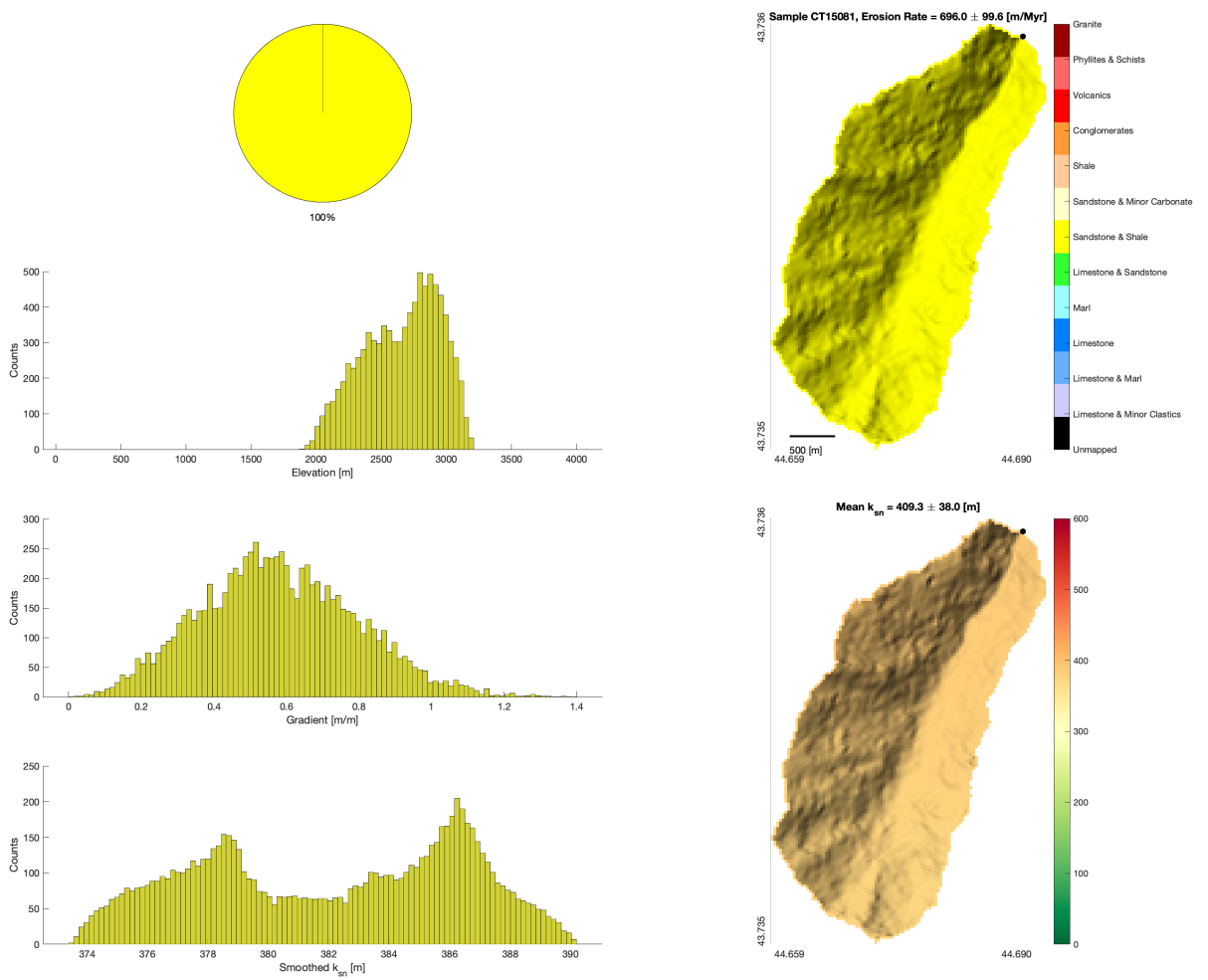


Figure S40: Relation between topography and lithology for sample CT15081. Left column shows, from top to bottom; percentage of catchment occupied by different lithologies (keyed to color bar in right), histogram of elevation and portion of each elevation bin represented by a given lithology, histogram of hillslope gradient and portion of each gradient bin represented by a given lithology, and histogram of smoothed k_{sn} and portion of each k_{sn} bin represented by a given lithology. Right column shows distribution of lithology within the catchment (top) and smoothed k_{sn} (bottom).

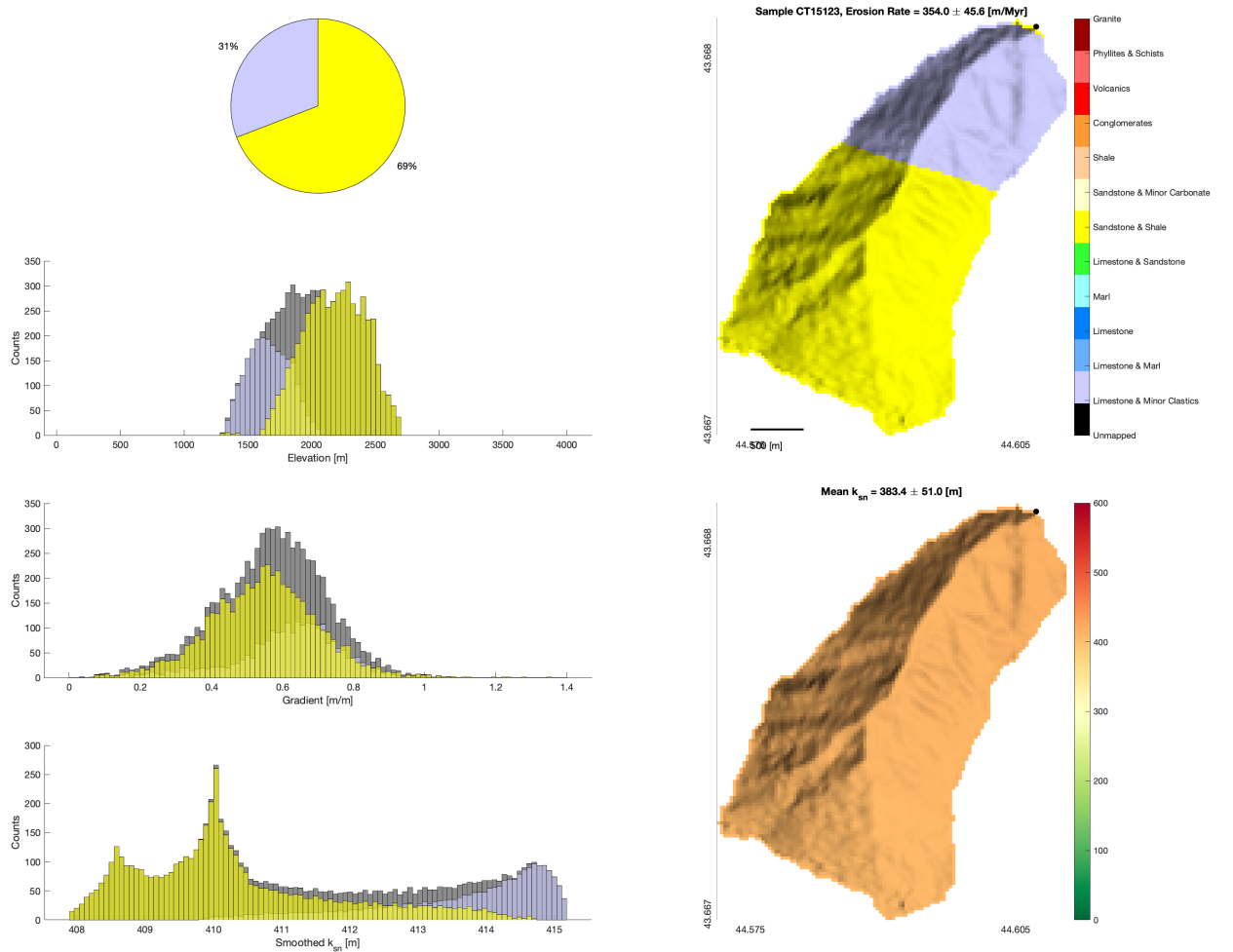


Figure S41: Relation between topography and lithology for sample CT15123. Left column shows, from top to bottom; percentage of catchment occupied by different lithologies (keyed to color bar in right), histogram of elevation and portion of each elevation bin represented by a given lithology, histogram of hillslope gradient and portion of each gradient bin represented by a given lithology, and histogram of smoothed k_{sn} and portion of each k_{sn} bin represented by a given lithology. Right column shows distribution of lithology within the catchment (top) and smoothed k_{sn} (bottom).

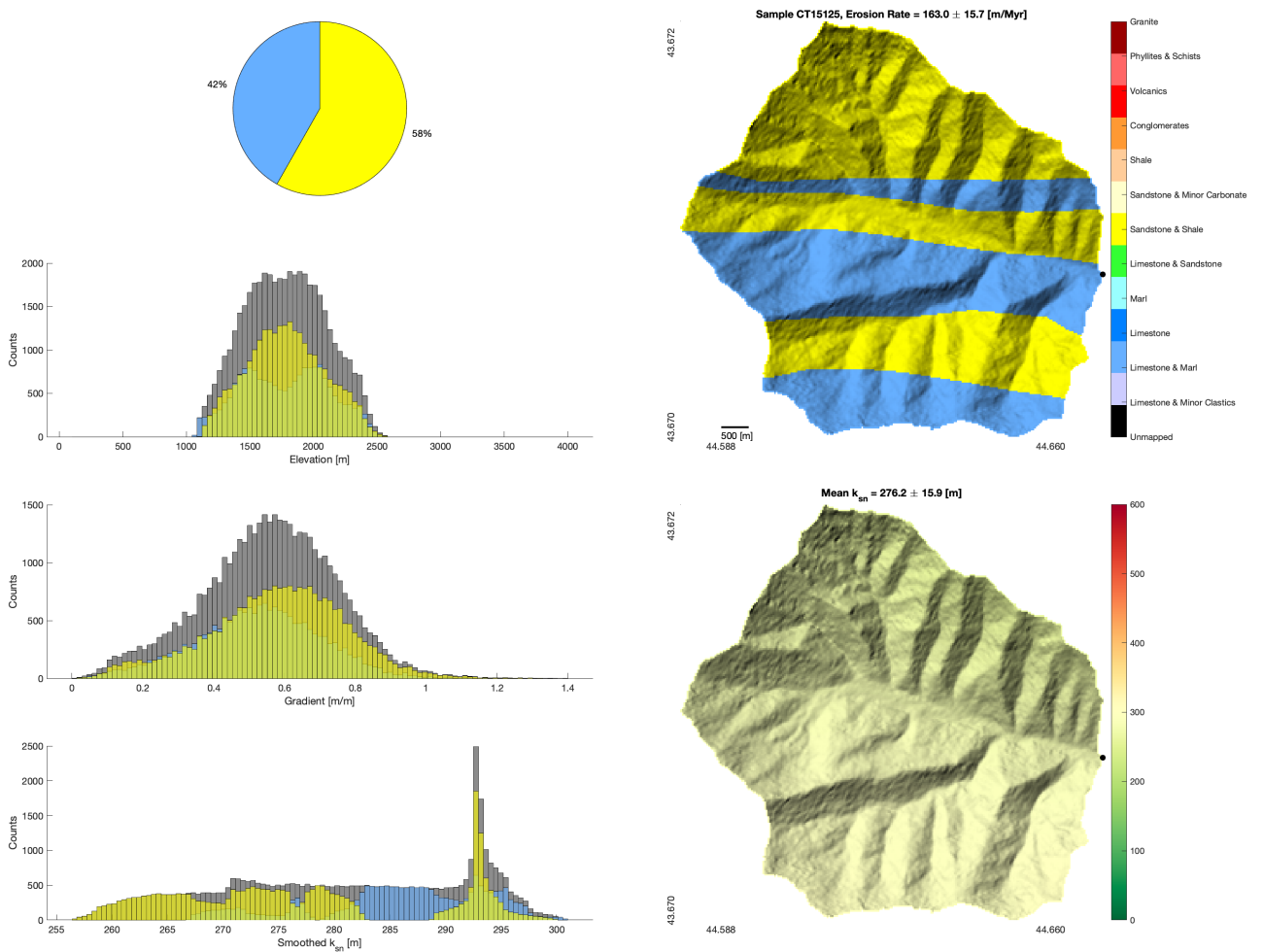


Figure S42: Relation between topography and lithology for sample CT15125. Left column shows, from top to bottom; percentage of catchment occupied by different lithologies (keyed to color bar in right), histogram of elevation and portion of each elevation bin represented by a given lithology, histogram of hillslope gradient and portion of each gradient bin represented by a given lithology, and histogram of smoothed k_{sn} and portion of each k_{sn} bin represented by a given lithology. Right column shows distribution of lithology within the catchment (top) and smoothed k_{sn} (bottom).

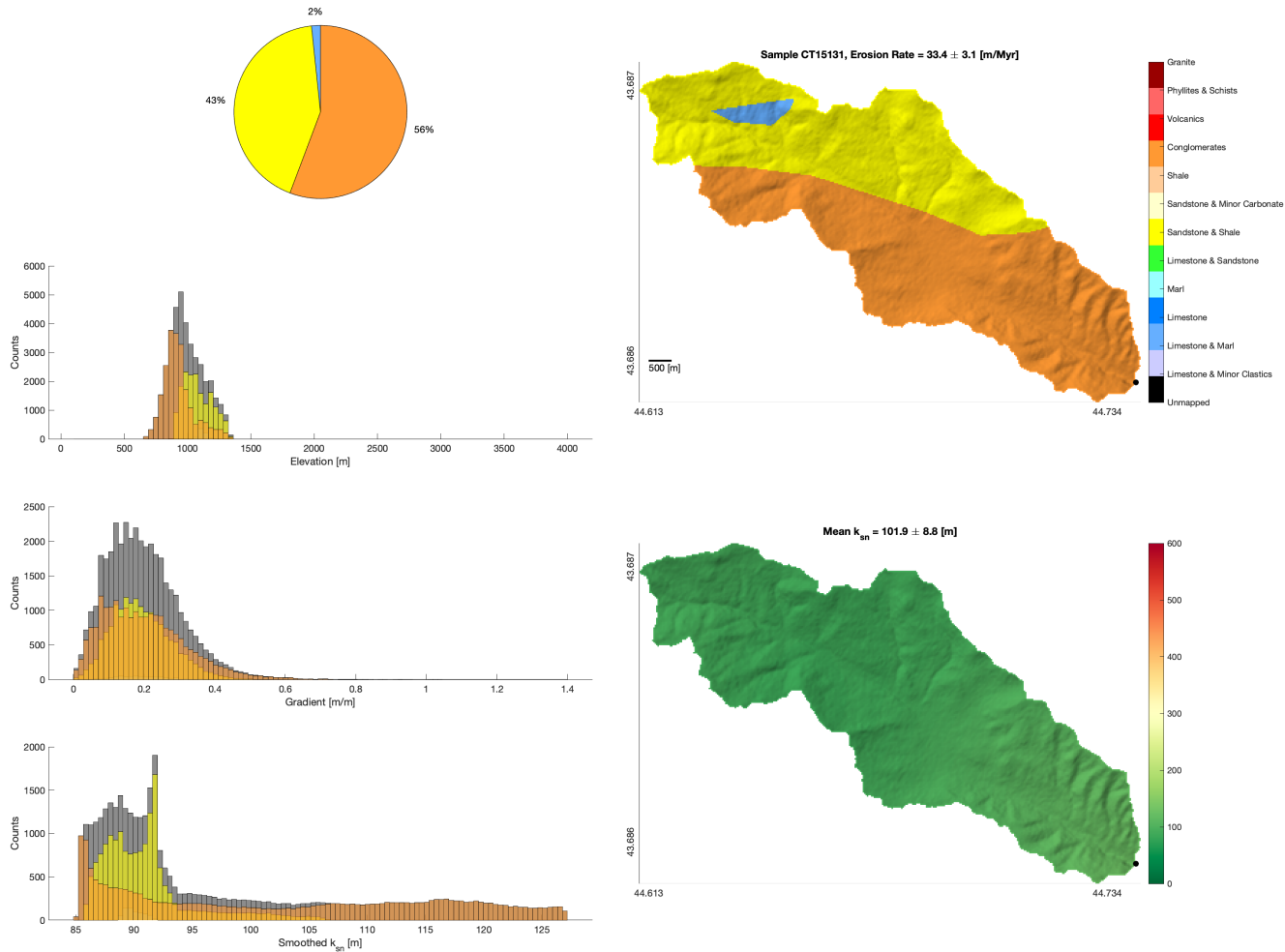


Figure S43: Relation between topography and lithology for sample CT15131. Left column shows, from top to bottom; percentage of catchment occupied by different lithologies (keyed to color bar in right), histogram of elevation and portion of each elevation bin represented by a given lithology, histogram of hillslope gradient and portion of each gradient bin represented by a given lithology, and histogram of smoothed k_{sn} and portion of each k_{sn} bin represented by a given lithology. Right column shows distribution of lithology within the catchment (top) and smoothed k_{sn} (bottom).

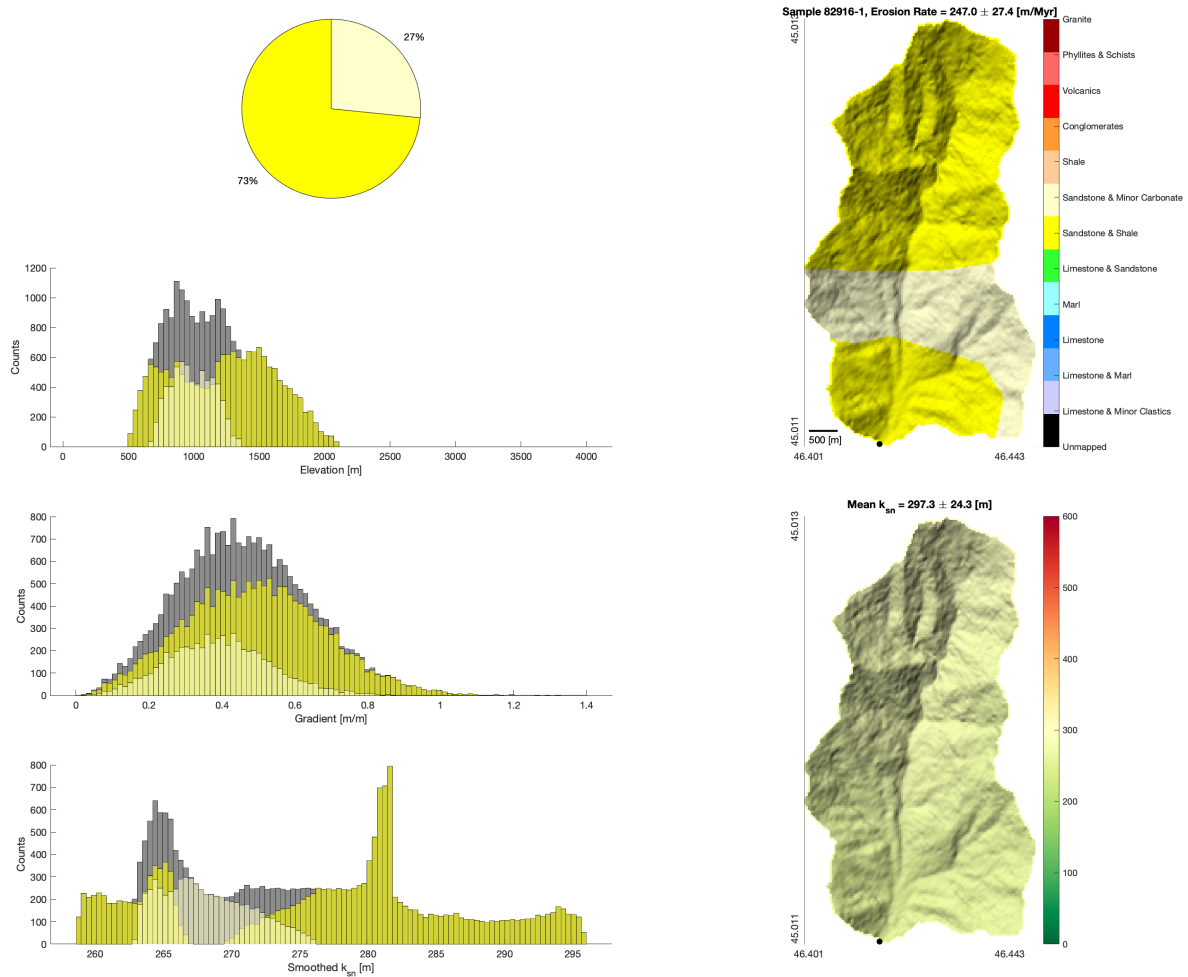


Figure S44: Relation between topography and lithology for sample 82916-1. Left column shows, from top to bottom; percentage of catchment occupied by different lithologies (keyed to color bar in right), histogram of elevation and portion of each elevation bin represented by a given lithology, histogram of hillslope gradient and portion of each gradient bin represented by a given lithology, and histogram of smoothed k_{sn} and portion of each k_{sn} bin represented by a given lithology. Right column shows distribution of lithology within the catchment (top) and smoothed k_{sn} (bottom).

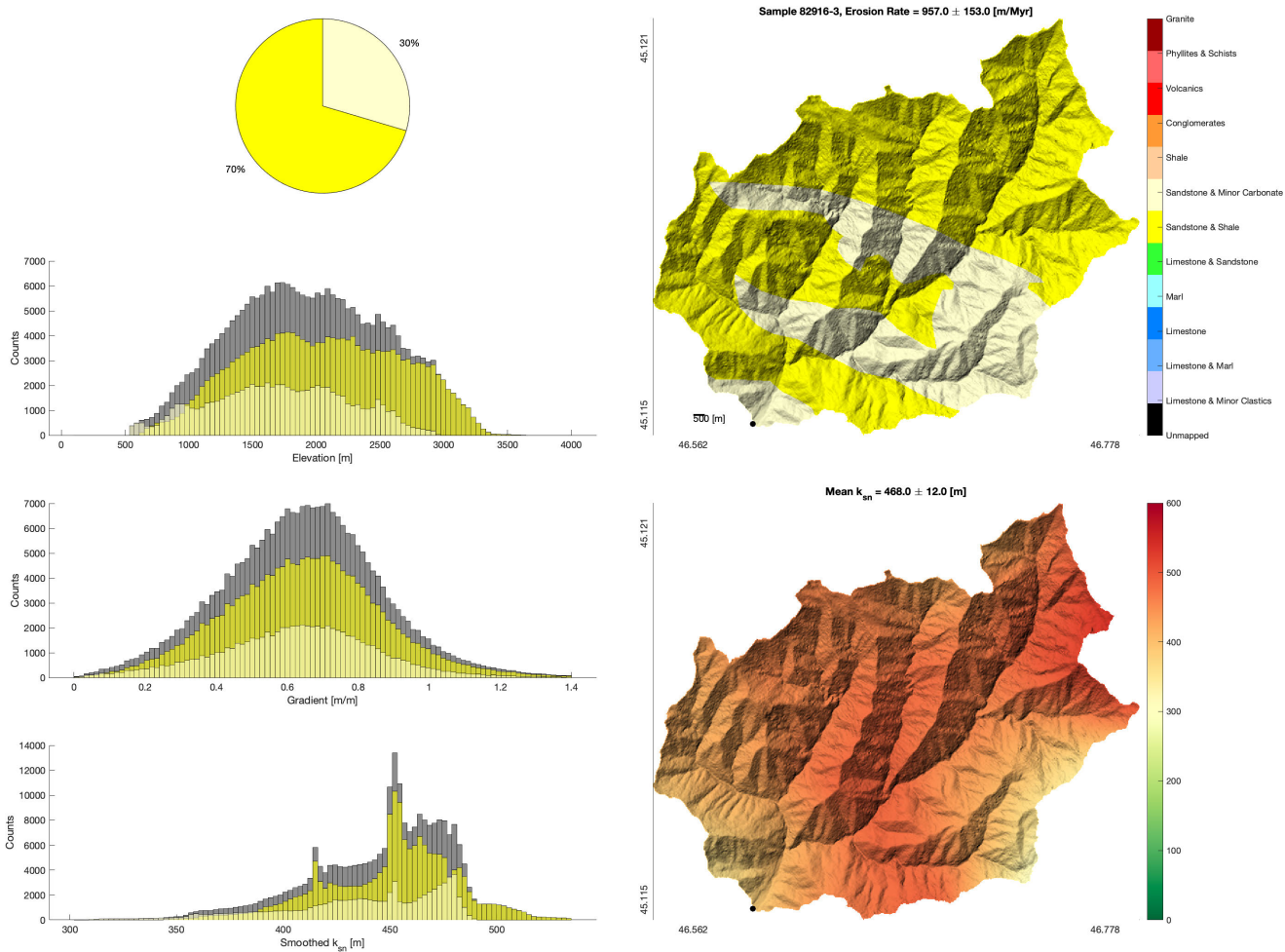


Figure S45: Relation between topography and lithology for sample 82916-3. Left column shows, from top to bottom; percentage of catchment occupied by different lithologies (keyed to color bar in right), histogram of elevation and portion of each elevation bin represented by a given lithology, histogram of hillslope gradient and portion of each gradient bin represented by a given lithology, and histogram of smoothed k_{sn} and portion of each k_{sn} bin represented by a given lithology. Right column shows distribution of lithology within the catchment (top) and smoothed k_{sn} (bottom).

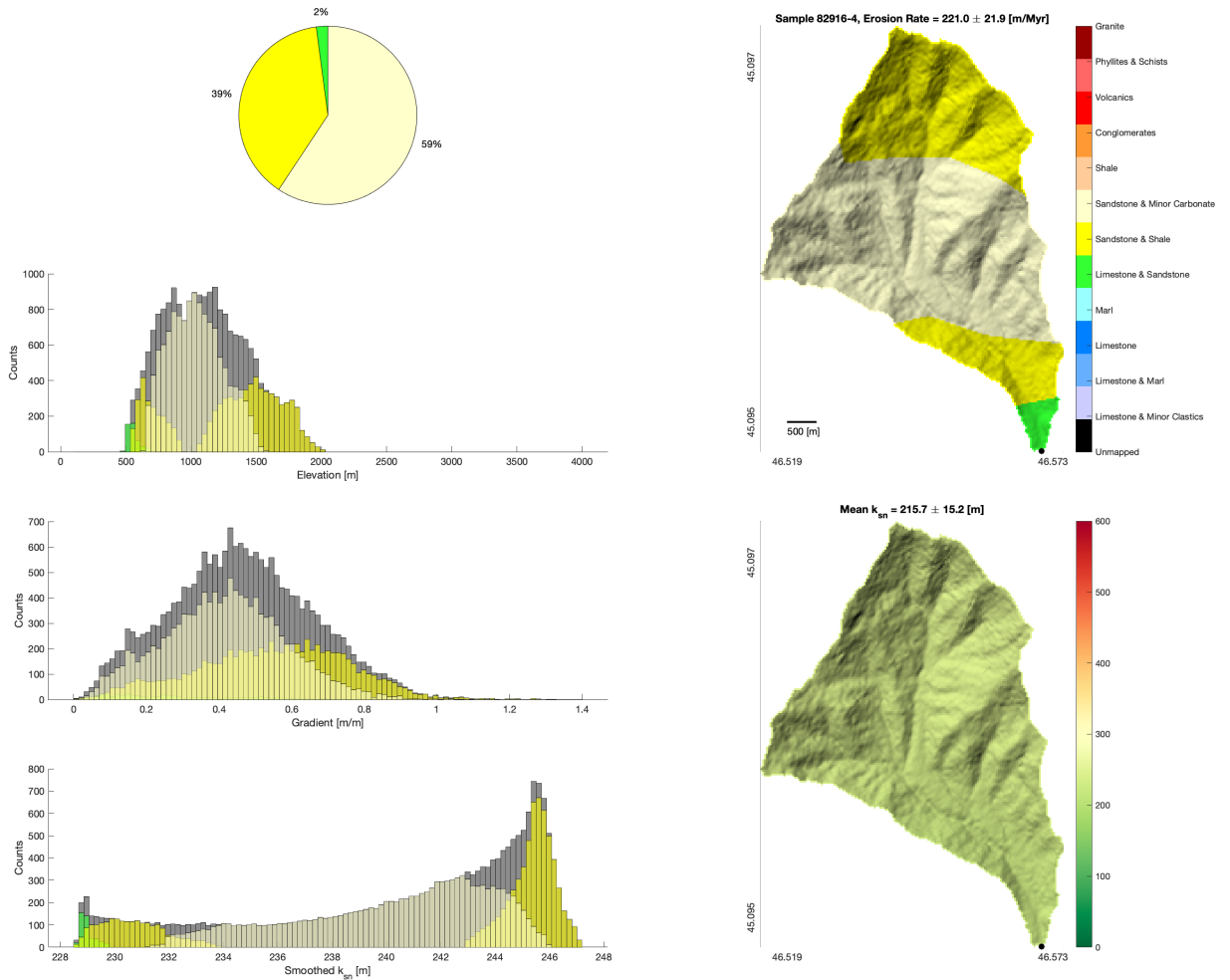


Figure S46: Relation between topography and lithology for sample 82916-4. Left column shows, from top to bottom; percentage of catchment occupied by different lithologies (keyed to color bar in right), histogram of elevation and portion of each elevation bin represented by a given lithology, histogram of hillslope gradient and portion of each gradient bin represented by a given lithology, and histogram of smoothed k_{sn} and portion of each k_{sn} bin represented by a given lithology. Right column shows distribution of lithology within the catchment (top) and smoothed k_{sn} (bottom).

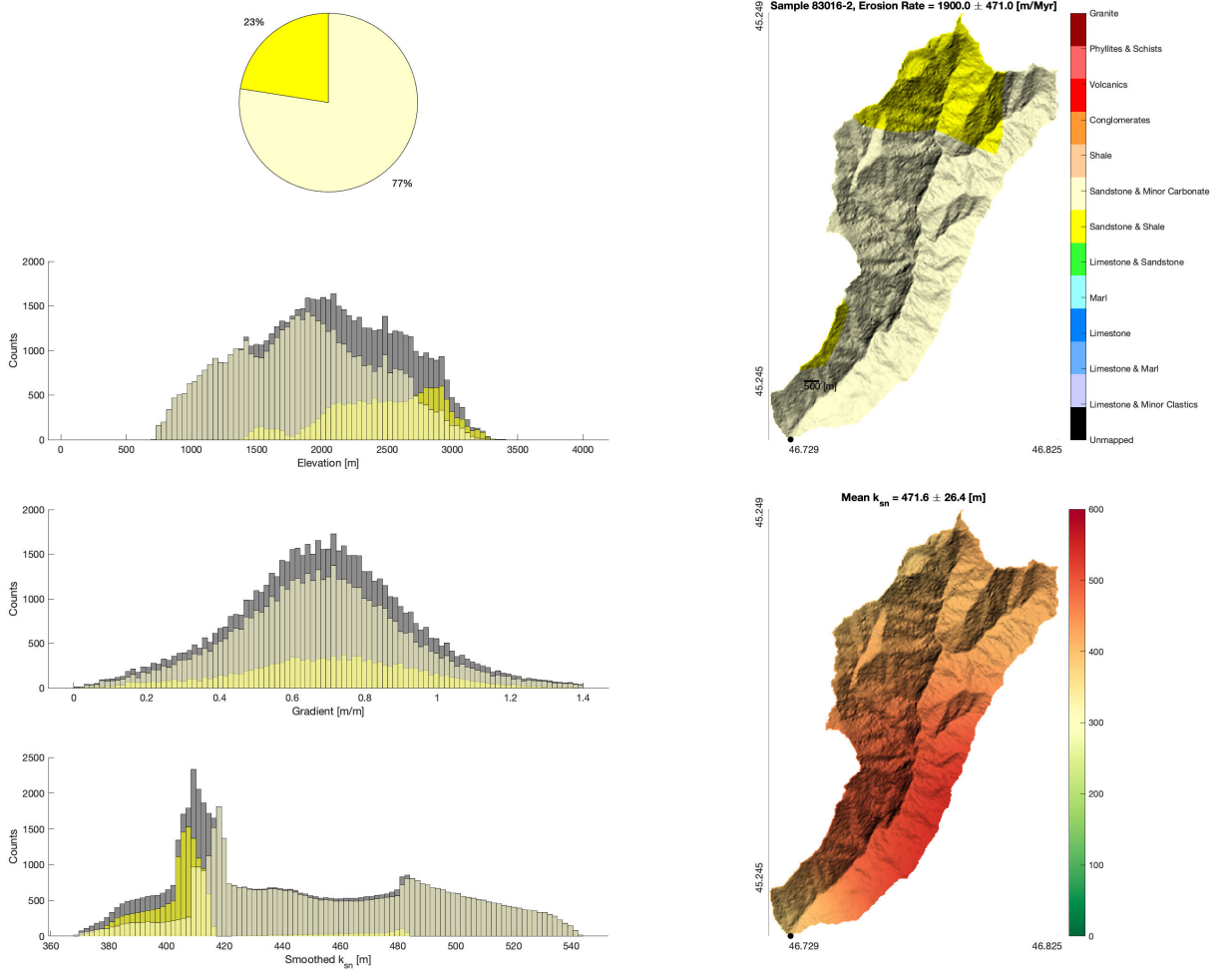


Figure S47: Relation between topography and lithology for sample 83016-2. Left column shows, from top to bottom; percentage of catchment occupied by different lithologies (keyed to color bar in right), histogram of elevation and portion of each elevation bin represented by a given lithology, histogram of hillslope gradient and portion of each gradient bin represented by a given lithology, and histogram of smoothed k_{sn} and portion of each k_{sn} bin represented by a given lithology. Right column shows distribution of lithology within the catchment (top) and smoothed k_{sn} (bottom).

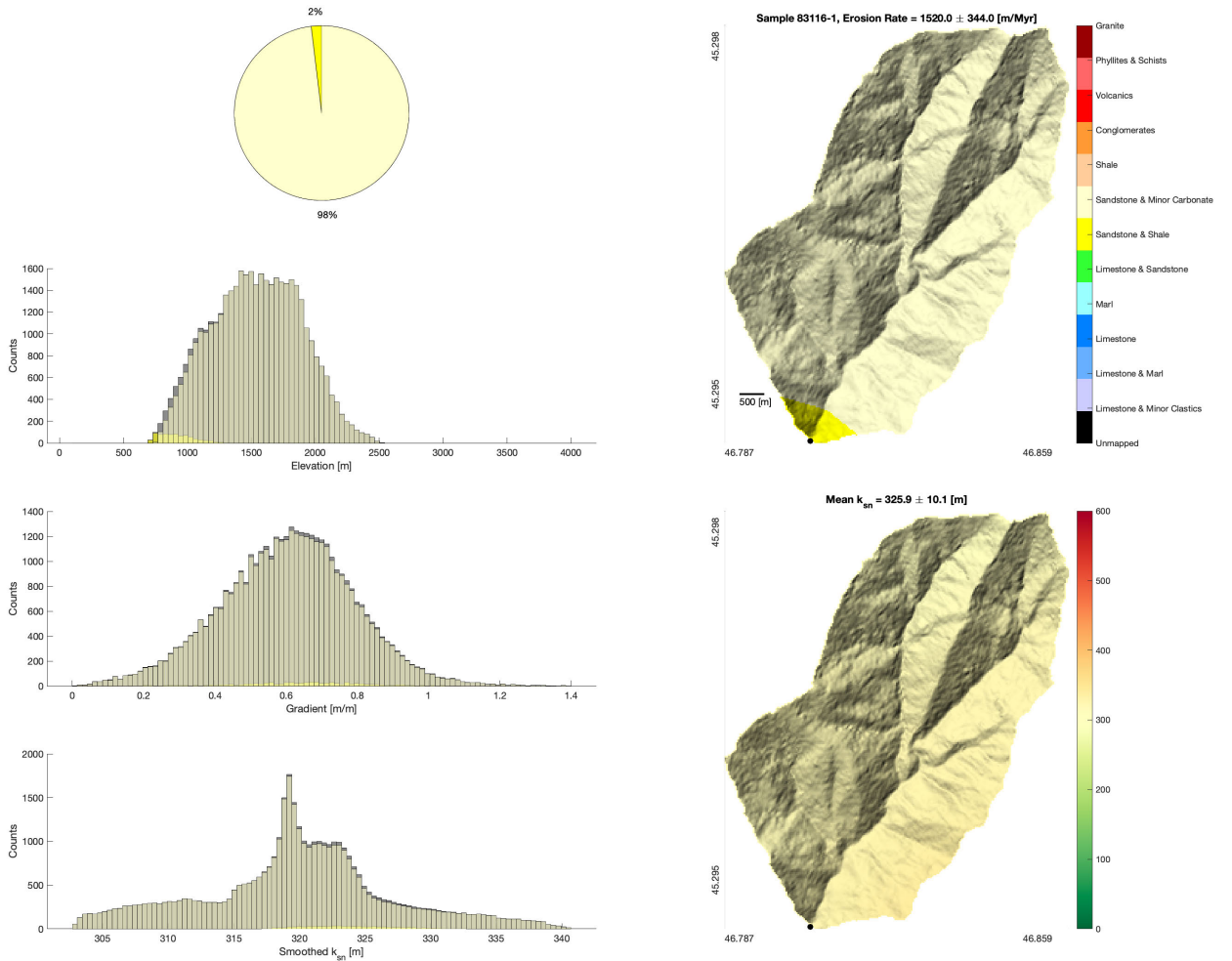


Figure S48: Relation between topography and lithology for sample 83116-1. Left column shows, from top to bottom; percentage of catchment occupied by different lithologies (keyed to color bar in right), histogram of elevation and portion of each elevation bin represented by a given lithology, histogram of hillslope gradient and portion of each gradient bin represented by a given lithology, and histogram of smoothed k_{sn} and portion of each k_{sn} bin represented by a given lithology. Right column shows distribution of lithology within the catchment (top) and smoothed k_{sn} (bottom).

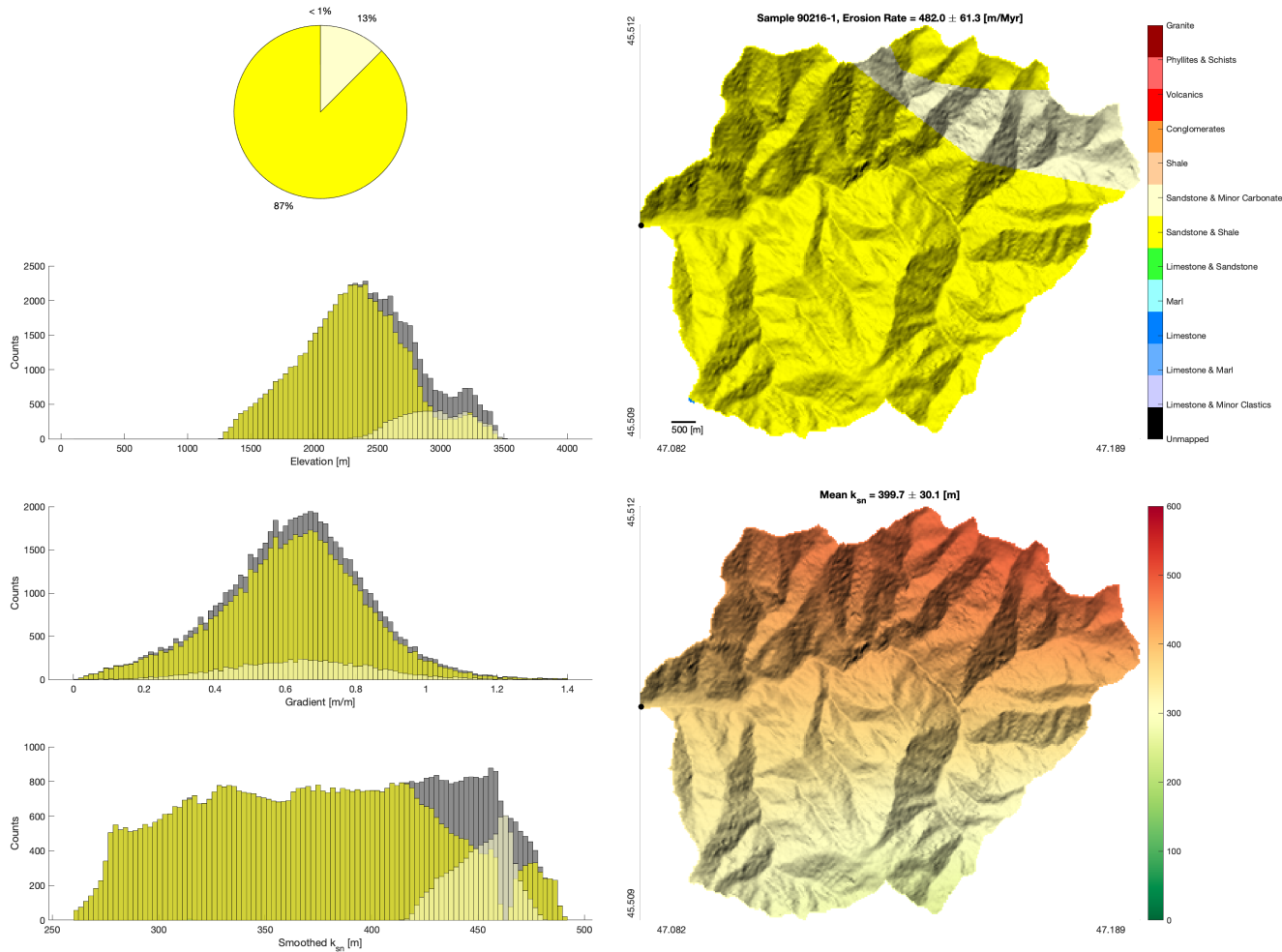


Figure S49: Relation between topography and lithology for sample 90216-1. Left column shows, from top to bottom; percentage of catchment occupied by different lithologies (keyed to color bar in right), histogram of elevation and portion of each elevation bin represented by a given lithology, histogram of hillslope gradient and portion of each gradient bin represented by a given lithology, and histogram of smoothed k_{sn} and portion of each k_{sn} bin represented by a given lithology. Right column shows distribution of lithology within the catchment (top) and smoothed k_{sn} (bottom).

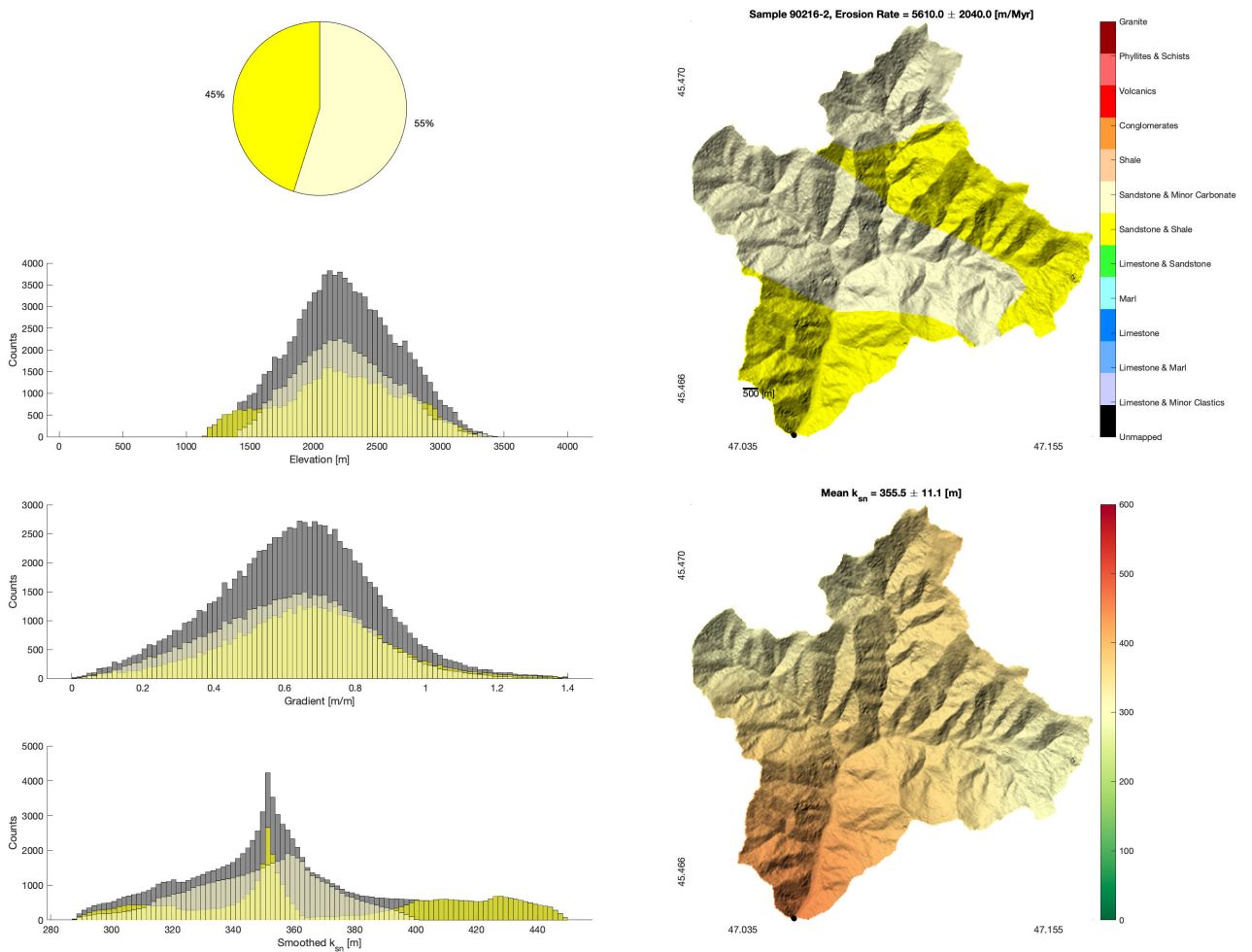


Figure S50: Relation between topography and lithology for sample 90216-2. Left column shows, from top to bottom; percentage of catchment occupied by different lithologies (keyed to color bar in right), histogram of elevation and portion of each elevation bin represented by a given lithology, histogram of hillslope gradient and portion of each gradient bin represented by a given lithology, and histogram of smoothed k_{sn} and portion of each k_{sn} bin represented by a given lithology. Right column shows distribution of lithology within the catchment (top) and smoothed k_{sn} (bottom).

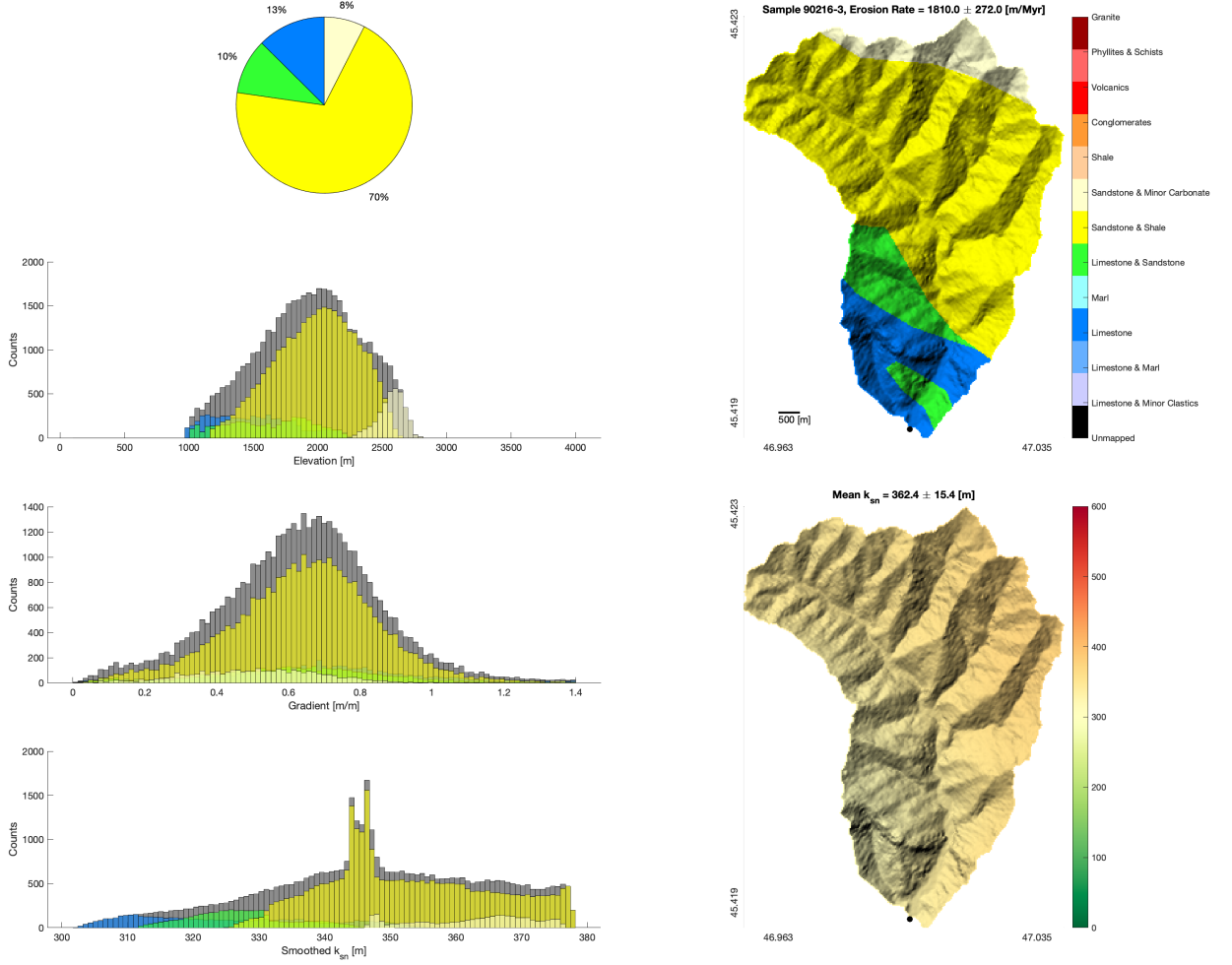


Figure S51: Relation between topography and lithology for sample 90216-3. Left column shows, from top to bottom; percentage of catchment occupied by different lithologies (keyed to color bar in right), histogram of elevation and portion of each elevation bin represented by a given lithology, histogram of hillslope gradient and portion of each gradient bin represented by a given lithology, and histogram of smoothed k_{sn} and portion of each k_{sn} bin represented by a given lithology. Right column shows distribution of lithology within the catchment (top) and smoothed k_{sn} (bottom).

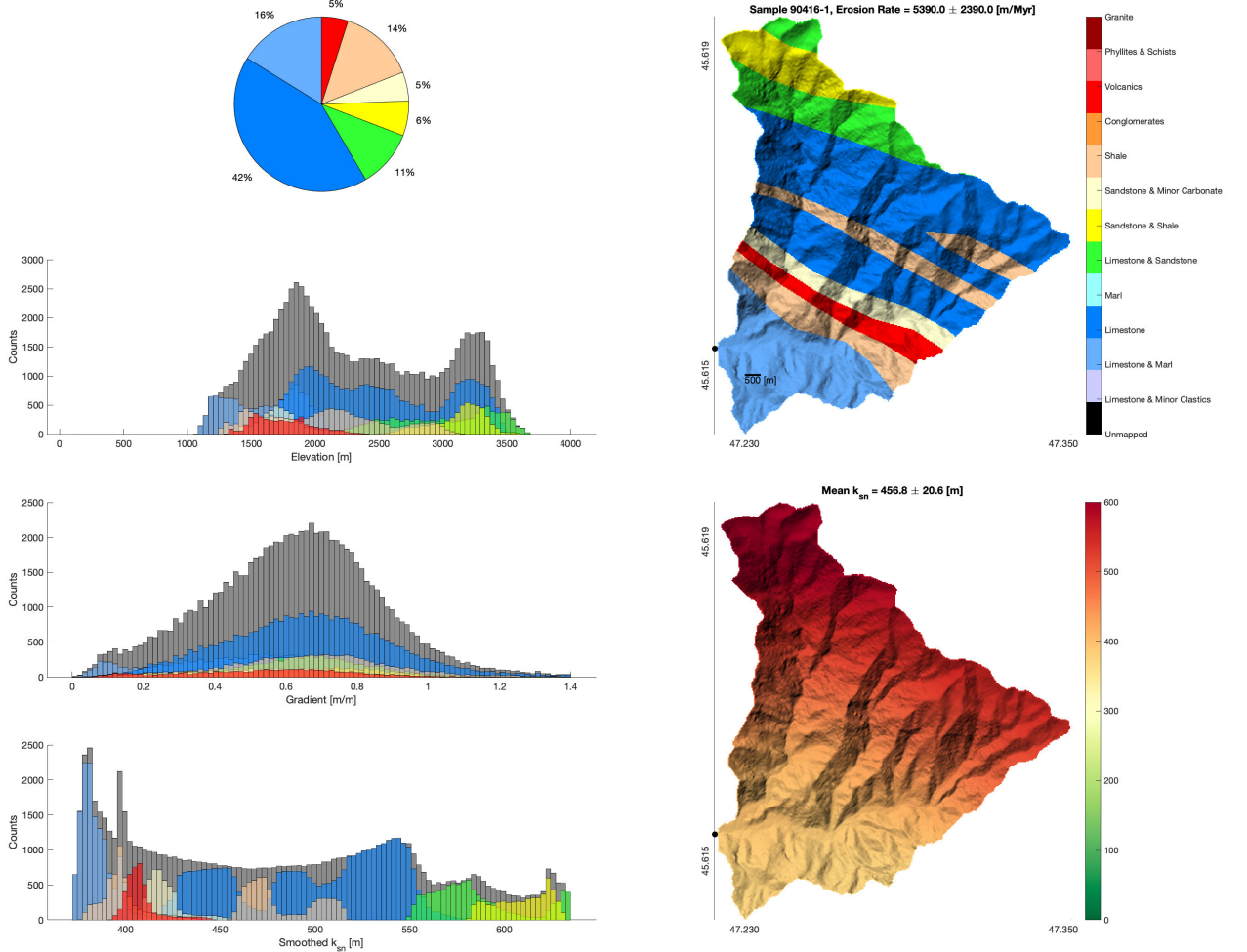


Figure S52: Relation between topography and lithology for sample 90416-1. Left column shows, from top to bottom; percentage of catchment occupied by different lithologies (keyed to color bar in right), histogram of elevation and portion of each elevation bin represented by a given lithology, histogram of hillslope gradient and portion of each gradient bin represented by a given lithology, and histogram of smoothed k_{sn} and portion of each k_{sn} bin represented by a given lithology. Right column shows distribution of lithology within the catchment (top) and smoothed k_{sn} (bottom).

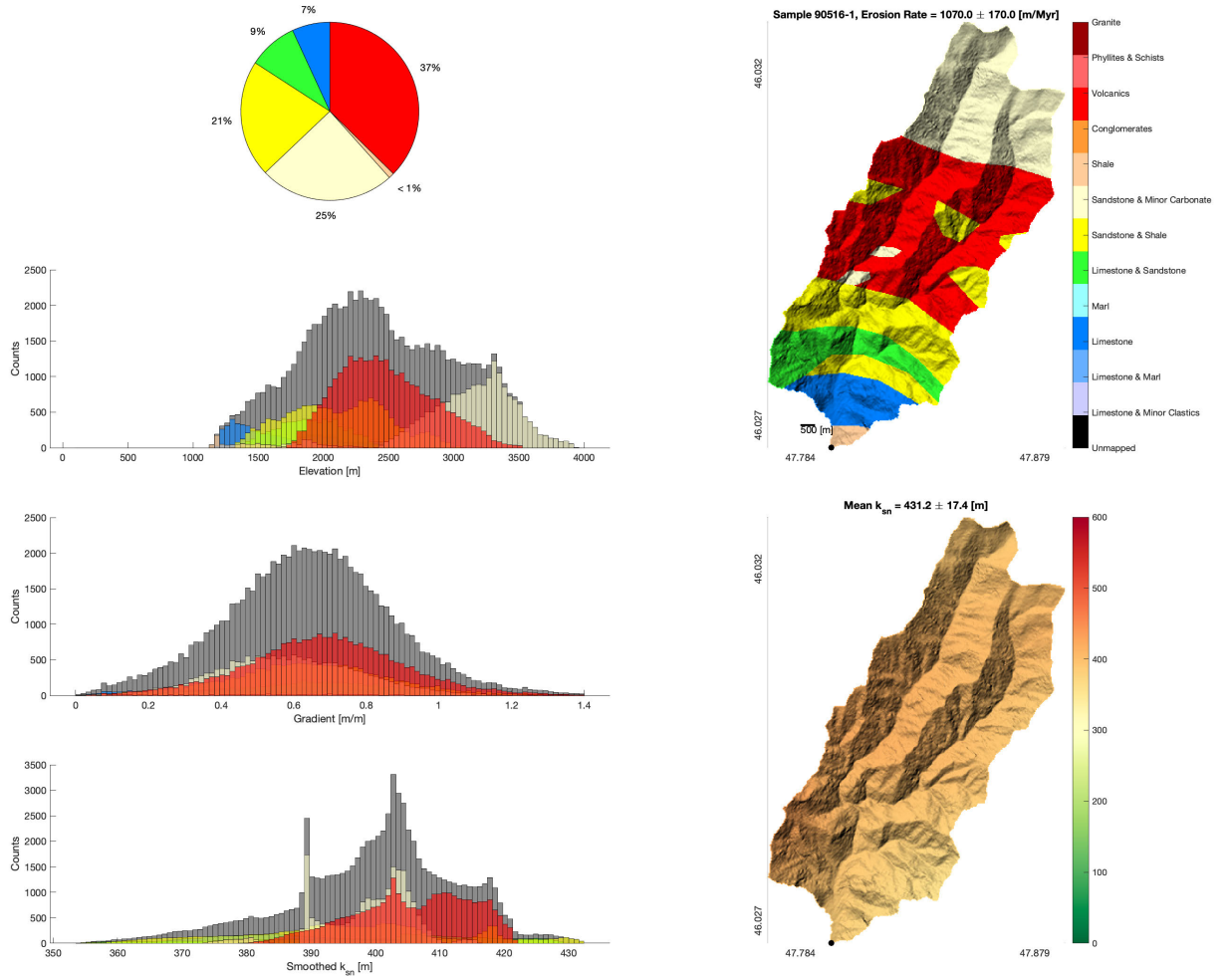


Figure S53: Relation between topography and lithology for sample 90516-1. Left column shows, from top to bottom; percentage of catchment occupied by different lithologies (keyed to color bar in right), histogram of elevation and portion of each elevation bin represented by a given lithology, histogram of hillslope gradient and portion of each gradient bin represented by a given lithology, and histogram of smoothed k_{sn} and portion of each k_{sn} bin represented by a given lithology. Right column shows distribution of lithology within the catchment (top) and smoothed k_{sn} (bottom).

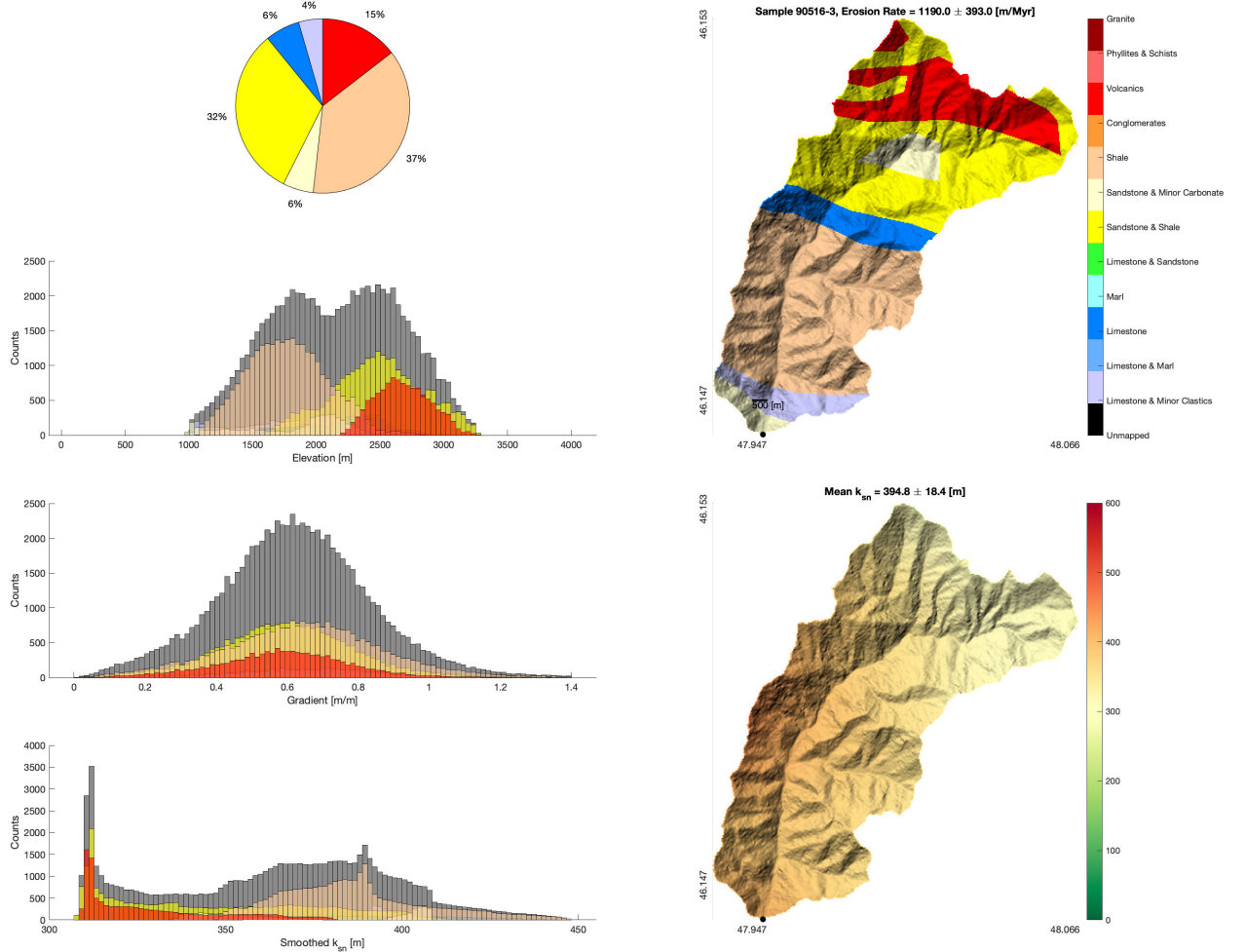


Figure S54: Relation between topography and lithology for sample 90516-3. Left column shows, from top to bottom; percentage of catchment occupied by different lithologies (keyed to color bar in right), histogram of elevation and portion of each elevation bin represented by a given lithology, histogram of hillslope gradient and portion of each gradient bin represented by a given lithology, and histogram of smoothed k_{sn} and portion of each k_{sn} bin represented by a given lithology. Right column shows distribution of lithology within the catchment (top) and smoothed k_{sn} (bottom).

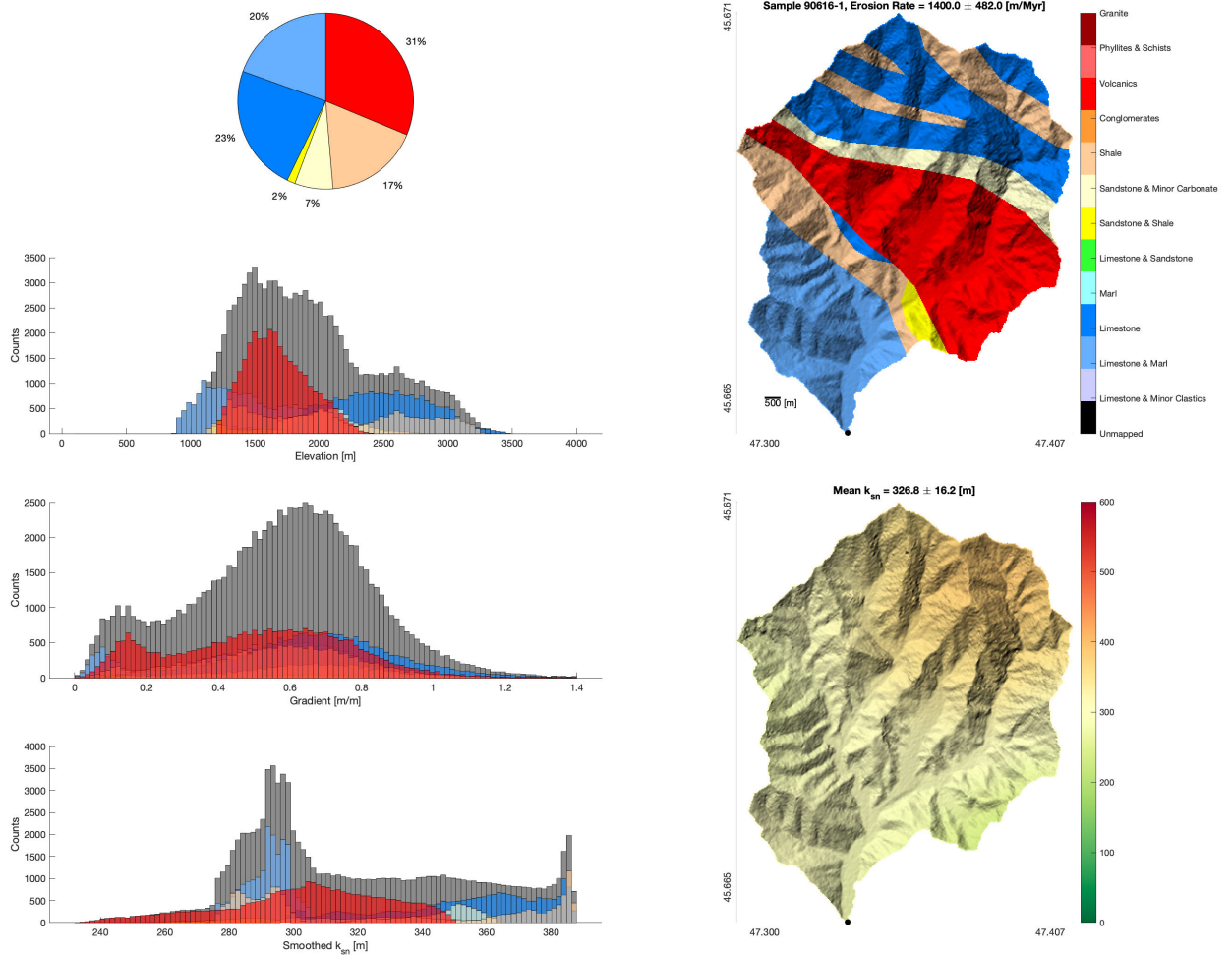


Figure S55: Relation between topography and lithology for sample 90616-1. Left column shows, from top to bottom; percentage of catchment occupied by different lithologies (keyed to color bar in right), histogram of elevation and portion of each elevation bin represented by a given lithology, histogram of hillslope gradient and portion of each gradient bin represented by a given lithology, and histogram of smoothed k_{sn} and portion of each k_{sn} bin represented by a given lithology. Right column shows distribution of lithology within the catchment (top) and smoothed k_{sn} (bottom).

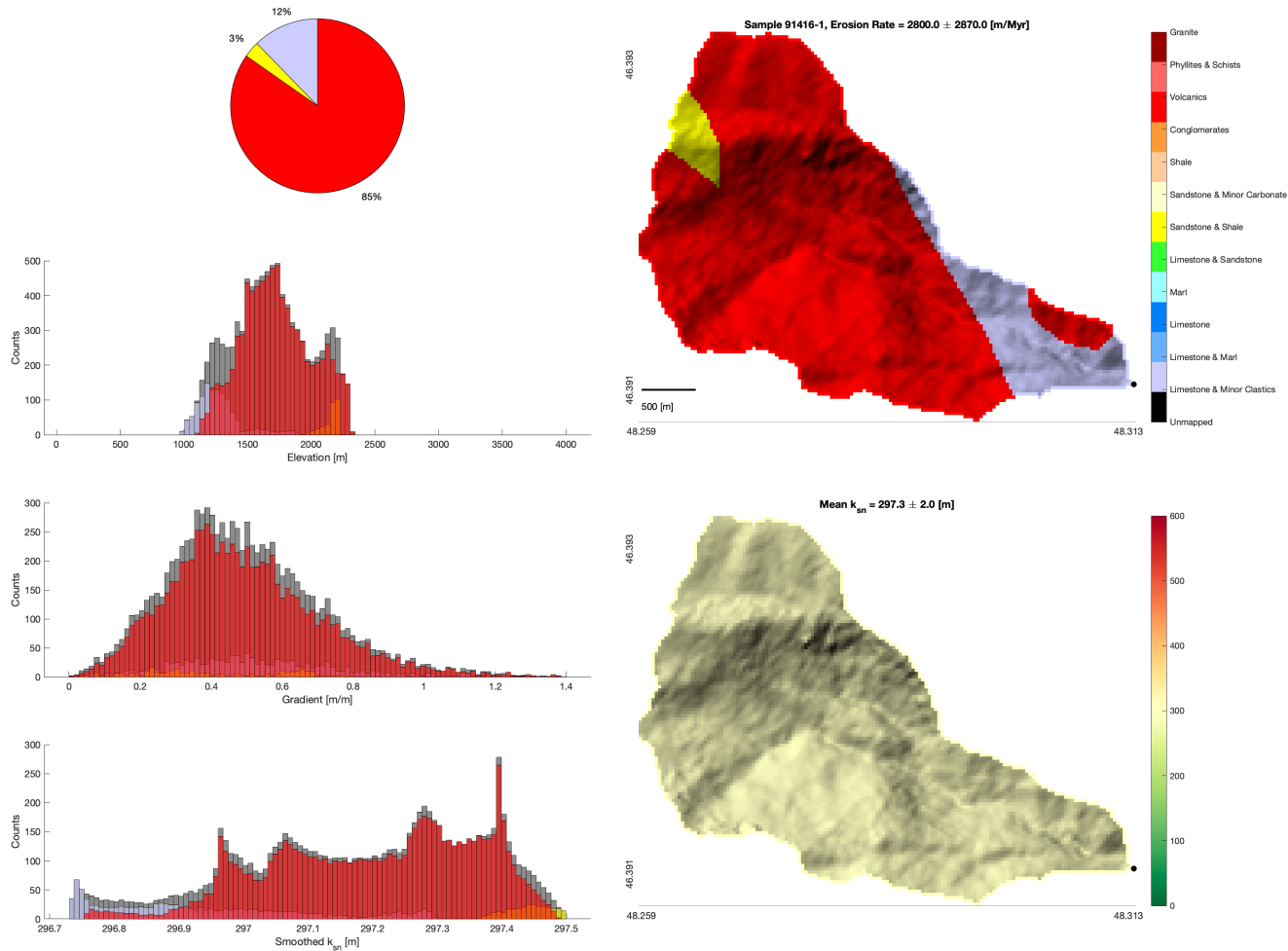


Figure S56: Relation between topography and lithology for sample 91416-1. Left column shows, from top to bottom; percentage of catchment occupied by different lithologies (keyed to color bar in right), histogram of elevation and portion of each elevation bin represented by a given lithology, histogram of hillslope gradient and portion of each gradient bin represented by a given lithology, and histogram of smoothed k_{sn} and portion of each k_{sn} bin represented by a given lithology. Right column shows distribution of lithology within the catchment (top) and smoothed k_{sn} (bottom).

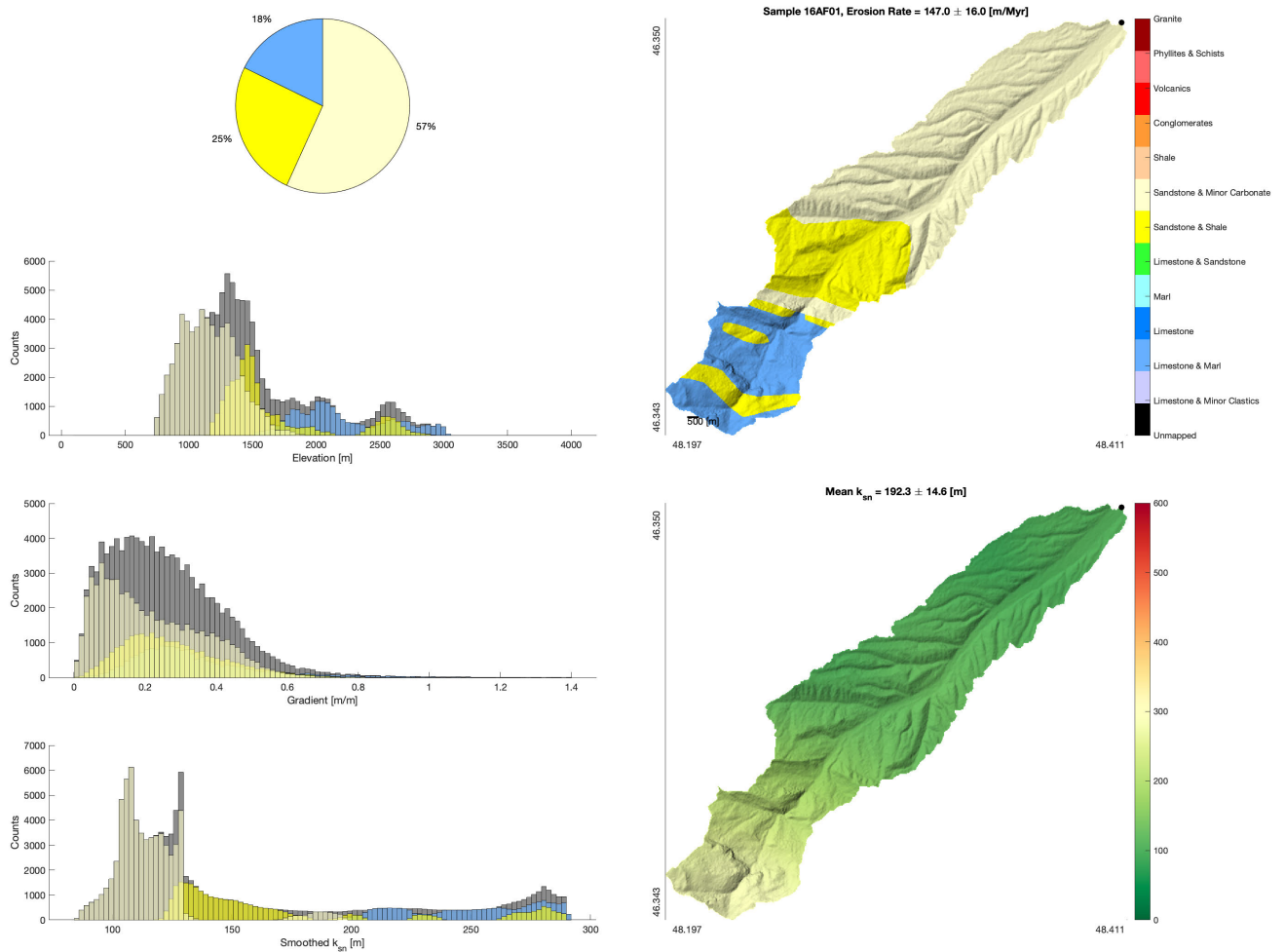


Figure S57: Relation between topography and lithology for sample 16AF01. Left column shows, from top to bottom; percentage of catchment occupied by different lithologies (keyed to color bar in right), histogram of elevation and portion of each elevation bin represented by a given lithology, histogram of hillslope gradient and portion of each gradient bin represented by a given lithology, and histogram of smoothed k_{sn} and portion of each k_{sn} bin represented by a given lithology. Right column shows distribution of lithology within the catchment (top) and smoothed k_{sn} (bottom).

References

- Byron A. Adams, Kelin X. Whipple, Adam M. Forte, Arjun M. Heimsath, and Kip V. Hodges. Climate controls on erosion in tectonically active landscapes. *Science Advances*, 6(42), 2020. doi: 10.1126/sciadv.aaz3166.
- A A Ali-Zade. Geological Map of Azerbaijan Republic, 2005.
- Akif A. Alizadeh, Ibrahim S. Guliyev, Fakhraddin A. Kadirov, and Lev V. Eppelbaum. *Geosciences of Azerbaijan: Volume I: Geology*. Regional Geology Reviews. Springer International Publishing, Cham, 2016. ISBN 978-3-319-27393-8 978-3-319-27395-2. doi: 10.1007/978-3-319-27395-2.
- Boris Avdeev and Nathan A Niemi. Rapid Pliocene exhumation of the central Greater Caucasus constrained by low-temperature thermochronometry. *Tectonics*, 30, 2011. doi: 10.1029/2010TC002808.
- Greg Balco, J Stone, N A Lifton, and Tibor Dunai. A complete and easily accessible means of calculating surface exposure ages or erosion rates from ^{10}Be and ^{26}Al measurements. *Quaternary Geochronology*, 3:174–195, 2008. doi: 10.1016/j.quageo.2007.12.001.
- Roman A. DiBiase. Short Communication: Increasing vertical attenuation length of cosmogenic nuclide production on steep slopes negates topographic shielding corrections for catchment erosion rates. Preprint, Cross-cutting themes: Geochronology applied to establish timing and rates of Earth surface processes, July 2018.
- Roman A DiBiase and Kelin X Whipple. The influence of erosion thresholds and runoff variability on the relationships among topography, climate, and erosion rate. *Journal of Geophysical Research*, 116(F04036), 2011. doi: 10.1029/2011JF002095.
- R.G. Ditchburn and N.E. Whitehead. The separation of ^{10}Be from silicates. In *3rd Workshop of the South Pacific Environmental Radioactivity Association*, pages 4–7, 1994.
- A I Dzhanelidze and N A Kandelaki. K-38-XIII, 1957.
- G. Burch Fisher, Bodo Bookhagen, and Colin B. Amos. Channel planform geometry and slopes from freely available high-spatial resolution imagery and DEM fusion: Implications for channel width scalings, erosion proxies, and fluvial signatures in tectonically active landscapes. *Geomorphology*, 194:46–56, 2013. ISSN 0169-555X. doi: 10.1016/j.geomorph.2013.04.011.
- Adam M Forte and Kelin X Whipple. Short communication : The Topographic Analysis Kit (TAK) for TopoToolbox. *Earth Surface Dynamics*, 7:87–95, 2019. doi: 10.5194/esurf-7-87-2019.
- Adam M Forte, Eric Cowgill, and Kelin X Whipple. Transition from a singly vergent to doubly vergent wedge in a young orogen: The Greater Caucasus. *Tectonics*, 33(11):2077–2101, 2014. doi: 10.1002/2014TC003651.
- Adam M Forte, Kelin X Whipple, B Bookhagen, and Matthew W Rossi. Decoupling of modern shortening rates, climate, and topography in the Caucasus. *Earth and Planetary Science Letters*, 449:282–294, 2016. doi: 10.1016/j.epsl.2016.06.013.
- P D Gamkrelidze. K-38-XX, 1958.
- P D Gamkrelidze and I R Kakhadze. K-38-VII, 1959.
- Ramin Gobejishvili, Nino Lomidze, Levan Tielidze, and Jaap J M van der Meer. Late Pleistocene (Würmian) Glaciations of the Caucasus. In J Ehlers, P L Gibbard, and P D Hughes, editors, *Quaternary Glaciations - Extent and Chronology*, pages 141–147. Elsevier, Amsterdam, 2011.
- Fakhraddin Kadirov, Michael Floyd, Akif Alizadeh, Ibrahim Guliev, R Reilinger, Sadi Kuleli, R King, and M N Toksoz. Kinematics of the eastern Caucasus near Baku, Azerbaijan. *Natural Hazards*, 63:997–1006, 2012.
- D N Kandelaki and I R Kakhadze. K-38-XV, 1957.
- N A Kandelaki and I R Kakhadze. K-38-XIV, 1957.
- V E Khain and A N Shardanov. K-39-XXV, 1960.

A. M. G. Klein Tank, J. B. Wijngaard, G. P. Können, R. Böhm, G. Demarée, A. Gocheva, M. Mileta, S. Pashiardis, L. Hejkrlik, C. Kern-Hansen, R. Heino, P. Bessemoulin, G. Müller-Westermeier, M. Tzanakou, S. Szalai, T. Pálisdóttir, D. Fitzgerald, S. Rubin, M. Capaldo, M. Maugeri, A. Leitass, A. Bukanis, R. Aberfeld, A. F. V. van Engelen, E. Forland, M. Mietus, F. Coelho, C. Mares, V. Razuvayev, E. Nieplova, T. Cegnar, J. Antonio López, B. Dahlström, A. Moberg, W. Kirchhofer, A. Ceylan, O. Pachaliuk, L. V. Alexander, and P. Petrovic. Daily dataset of 20th-century surface air temperature and precipitation series for the European Climate Assessment: EUROPEAN TEMPERATURE AND PRECIPITATION SERIES. *International Journal of Climatology*, 22(12):1441–1453, October 2002. ISSN 08998418. doi: 10.1002/joc.773.

C. Kohl and K. Nishizumi. Chemical isolation of quartz for measurement of in situ-produced cosmogenic nuclides. *Geochimica et Cosmochimica Acta*, 56(9):3583–3587, 1992.

V N Krestnikov. K-38-XVI, 1957.

Dimitri Lague, N Hovius, and P Davy. Discharge, discharge variability, and the bedrock channel profile. *Journal of Geophysical Research*, 110:F04006–F04006, 2005. doi: 10.1029/2004JF000259.

V A Melnikov and E I Popova. K-38-VIII, 1975.

Charles Mifsud, Toshiyuki Fujioka, and David Fink. Extraction and purification of quartz in rock using hot phosphoric acid for in situ cosmogenic exposure dating. *Nuclear Instruments and Methods in Physics Research B*, 294:203–207, 2013. ISSN 0168-583X. doi: 10.1016/j.nimb.2012.08.037.

Nathan A Niemi, Michael Osokin, Douglas Burbank, Arjun M Heimsath, and Emmanuel J Gabet. Effects of bedrock landslides on cosmogenically determined erosion rates. *Earth and Planetary Science Letters*, 237:480–498, 2005.

M. C. Palucis and M. P. Lamb. What controls channel form in steep mountain streams?: Controls on Steep Channel Form. *Geophysical Research Letters*, 44(14):7245–7255, July 2017. ISSN 00948276. doi: 10.1002/2017GL074198.

Eric W Portenga and Paul R Bierman. Understanding Earth's eroding surface with ^{10}Be . *GSA Today*, 21(8):4–10, 2011. doi: 10.1130/G111A.1.

R Reilinger, S McClusky, Philippe Vernant, S Lawrence, S Ergintav, Rahsan Cakmak, Haluk Ozener, Fakhreddin Kadirov, Ibrahim Guliev, Ruben Stepanyan, M Nadariya, Galaktion Hahubia, S Mahmoud, K Sakr, Abdullah ArRajehi, D Paradissis, A Al-Aydrus, M Prilepin, Tamara Guseva, Emre Evren, Andriy Dmitrotsa, S V Filikov, Francisco Gomez, Riad Al-Ghazzi, and Gebran Karam. GPS constraints on continental deformation in the Africa-Arabia-Eurasia continental collision zone and implications for the dynamics of plate interactions. *Journal of Geophysical Research*, 111:doi:10.1029/2005JB004051–doi:10.1029/2005JB004051, 2006.

Joshua J Roering, J Taylor Perron, and James W Kirchner. Functional relationships between denudation and hillslope form and relief. *Earth and Planetary Science Letters*, 264:245–258, 2007.

Matthew W Rossi, Kelin X Whipple, and Enrique R Vivoni. Precipitation and evapotranspiration controls on event-scale runoff variability in the contiguous United States and Puerto Rico. *Journal of Geophysical Research*, 121, 2016. doi: 10.1002/2015JF003446.

W Schwanghart and D Scherler. Short Communication: TopoToolbox 2 - MATLAB based software for topographic analysis and modeling in Earth surface sciences. *Earth Surface Dynamics*, 2:1–7, 2014. doi: 10.5194/esurf-2-1-2014.

G. Sokhadze, M. Floyd, T. Godoladze, R. King, E. S. Cowgill, Z. Javakhishvili, G. Hahubia, and R. Reilinger. Active convergence between the Lesser and Greater Caucasus in Georgia: Constraints on the tectonic evolution of the Lesser–Greater Caucasus continental collision. *Earth and Planetary Science Letters*, 481:154–161, 2018. doi: 10.1016/j.epsl.2017.10.007.

John O. Stone. Air pressure and cosmogenic isotope production. *Journal of Geophysical Research: Solid Earth*, 105(B10): 23753–23759, October 2000. ISSN 01480227. doi: 10.1029/2000JB900181.

J. V. Sutcliffe, F. A. K. Farquharson, E. L. Tate, and S. S. Folwell. Flood regimes in the Southern Caucasus: The influence of precipitation on mean annual floods and frequency curves. *Hydrology Research*, 39(5-6):385–401, October 2008. ISSN 0029-1277, 2224-7955. doi: 10.2166/nh.2008.025.

Gregory E Tucker. Drainage basin sensitivity to tectonic and climatic forcing: Implications of a stochastic model for the role of entrainment and erosion thresholds. *Earth Surface Processes and Landforms*, 29:185–204, 2004. doi: 10.1002/esp.1020.

Gregory E Tucker and Rafael L Bras. A stochastic approach to modeling the role of rainfall variability in drainage basin evolution. *Water Resources Research*, 36(7):1953–1964, 2000.

H Wulf, B Bookhagen, and D Scherler. Differentiating between rain, snow, and glacier contributions to river discharge in the western Himalaya using remote-sensing data and distributed hydrologic modeling. *Advances in Water Resources*, 88: 152–169, 2016. doi: 10.1016/j.advwatres.2015.12.004.

B J Yanites, Gregory E Tucker, and Robert S Anderson. Numerical and analytical models of cosmogenic radionuclide dynamics in landslide-dominated drainage basins. *Journal of Geophysical Research*, 114:F01007–F01007, 2009. doi: 10.1029/2008JF001088.

Brian J. Yanites, Nate A. Mitchell, Joshua C. Bregy, Grace A. Carlson, Kirstyn Cataldo, Margaret Holahan, Graham H. Johnston, Amelia Nelson, Jeffery Valenza, and Matthew Wanker. Landslides control the spatial and temporal variation of channel width in southern Taiwan: Implications for landscape evolution and cascading hazards in steep, tectonically active landscapes: Variation in channel morphology controlled by landslides in s. Taiwan. *Earth Surface Processes and Landforms*, 43 (9):1782–1797, July 2018. ISSN 01979337. doi: 10.1002/esp.4353.